MULTIPOLAR ORDER AND FLUCTUATIONS IN TmAg2 AND YbRu2Ge2

A DISSERTATION
SUBMITTED TO THE DEPARTMENT OF APPLIED PHYSICS
AND THE COMMITTEE ON GRADUATE STUDIES
OF STANFORD UNIVERSITY
IN PARTIAL FULFILLMENT OF THE REQUIREMENTS
FOR THE DEGREE OF
DOCTOR OF PHILOSOPHY

Elliott Rosenberg
August 2020

© 2020 by Elliott William Rosenberg. All Rights Reserved.
Re-distributed by Stanford University under license with the author.

This work is licensed under a Creative Commons Attribution-3.0 United States License.
http://creativecommons.org/licenses/by/3.0/us/

This dissertation is online at: http://purl.stanford.edu/dj722qw1039

I certify that I have read this dissertation and that, in my opinion, it is fully adequate in scope and quality as a dissertation for the degree of Doctor of Philosophy.

Ian Fisher, Primary Adviser

I certify that I have read this dissertation and that, in my opinion, it is fully adequate in scope and quality as a dissertation for the degree of Doctor of Philosophy.

Aharon Kapitulnik

I certify that I have read this dissertation and that, in my opinion, it is fully adequate in scope and quality as a dissertation for the degree of Doctor of Philosophy.

Steven Kivelson

Approved for the Stanford University Committee on Graduate Studies.

Stacey F. Bent, Vice Provost for Graduate Education

This signature page was generated electronically upon submission of this dissertation in electronic format. An original signed hard copy of the signature page is on file in University Archives.

Preface

The cooperative alignment of complex local electron density distributions can be defined through the spontaneous development of a term in the multipole expansion of the charge/current distribution on each site, which is fixed to break certain symmetries by the definition of that multipole. For instance the simplest example of multipole order is local moment ferromagnetism, in which local magnetic dipoles align collectively to break time-reversal symmetry. The multipolar order observed in the $4f$ intermetallics $TmAg_2$ and $YbRu_2Ge_2$, the materials studied in this thesis, is characterized by the alignment of higher order local multipolar degrees of freedom, namely electric quadrupoles, which break the rotational symmetry of the host tetragonal crystal lattice. These low temperature ferroquadrupolar phase transitions can be suppressed towards 0K, offering avenues towards studying materials in regimes where quantum fluctuations may dominate the properties of the system, also known as the quantum critical regime. Quantum criticality in general is a topic of considerable current interest from both a theoretical and experimental perspective, yet relatively little has been studied of the potential consequences of the suppression of ferroquadrupolar phase transitions. Futhermore, from a symmetry perspective, these transitions are specific realizations of electronic Ising-nematic phase transitions (exhibited, for example, by several Fe-pnictide superconductor families), as they spontaneously lower the in-plane C_4 rotational symmetry to C_2. Therefore this work is motivated not only in its contributions to understanding multipolar phase transitions and associated quantum criticality, but also from its connection to aspects of the phase diagrams of certain high Tc superconductors.

In this thesis we will show thermodynamic and transport properties of two $4f$ intermetallic materials, $YbRu_2Ge_2$ and $TmAg_2$. Both of these materials have been proposed to undergo ferroquadrupolar phase transitions in the B_{1g} symmetry channel, at 10.2K and 5K respectively. The B_{1g} elastoresistivity and low-temperature X-ray measurements of $YbRu_2Ge_2$, and the strain-tuning of the phase transition for $TmAg_2$ as inferred from the elastocaloric technique, that are presented here establish that this is indeed the case for both of these materials. We investigate in detail how both of these ferroquadrupolar phase transitions can be/are suppressed towards a quantum phase transition at 0K, through the application of a magnetic field applied along the c-axis at $\sim 21.3T$ and $\sim 3.1T$ for $YbRu_2Ge_2$ and $TmAg_2$ respectively. The quadrupole-strain susceptibilities of these materials

are investigated throughout their respective H-T phase diagrams (using two different complimentary probes), revealing higher-order octupolar couplings in $YbRu_2Ge_2$, and a transverse-field mean field Ising susceptibility for the quadrupole-strain susceptibility of $TmAg_2$. Resistivity measurements indicate potential signatures of quantum criticality in the proximity of the field-suppressed ferroquadrupolar phase transition for $YbRu_2Ge_2$.

Acknowledgments

This work was supported by the Gordon and Betty Moore Foundation Emergent Phenomena in Quantum Systems Initiative through Grant GBMF4414. A portion of this work was performed at the National High Magnetic Field Laboratory, which is supported by the National Science Foundation Cooperative Agreement No. DMR-1644779. A portion of this work was also performed at the Cornell High Energy Synchrotron Source, which is supported by the NSF and NIH/National Institute of General Medical Sciences via NSF Award DMR-133208.

I would like to thank my thesis committee and my reading committee, especially for scheduling the defense and reading this work on such short notice.

I would like to thank my coauthors, specifically Akash Maharaj and Jacob Ruff, as well as the Maglab staff at Tallahassee, SNSF staff at Stanford, and CHESS staff at Cornell, for enabling the experimental and theoretical work in this thesis to be completed. Thankfully, science is collaborative, as otherwise I would not be at this stage now.

I would also like to thank the GLAM administrators and staff. Without them dealing with my late RA forms I would have never gotten my salary, which would have made it rough to continue working, as well as paying rent and eating.

Foremost in my mind, I would like to deeply thank my advisor, Ian Fisher. He tolerated my tardiness to group meetings for years (I should have set my clock 7 minutes ahead), and dealt with my very abnormal sleeping/lab schedule (they were switched compared to everyone else). Without his guidance and compassion I sincerely don't think I would have made it to this point. I looked forward to our weekly talks not only to guide my scientific progress but also to catch up with a friend, and I hope he may have thought similarly. His passion for science is contagious, and he inspired me to continue to pursue studying condensed matter physics in the next stage of my career.

The other people that helped inspire me to complete this journey are the postdocs I interacted with during my nearly 7 years in the Fisher lab (I believe I hold the Fisher lab record for taking the longest time to graduate). They are: Jiun-Haw Chu, Phillip K. Walmsley, Harlyn Silverstein, Matthias Ikeda, Pierre Massat, and Maja Bachmann. Harlyn was incredibly impresssive in his encyclopedic knoweldge of chemistry, and he has inspired me to become the best crystal grower I can be. I learned international and French culture from Pierre, and I'm still very impressed he's

going to be a pilot. Although my shared time with Maja has been brief she is a great addition to the Fisher Lab, and I hope when I start my postdoc I can come in and immediately start designing and constructing experiments as she has. I want to specifically thank the postdocs that served as mentors to me during the different stages of my graduate student journey: Jiun-Haw, Phil, and Matthias.

Jiun-Haw was the first postdoc that I interacted with when started working, and he showed me what a experimentalist can be. Persistent, bold, skilled, with an incredible depth and breadth of knowledge, Jiun-Haw set the mark that I constantly aimed for, and that I will continue to aim for, and most likely never achieve. This is the reason I'm excited to work with him as a postdoc in his new lab, not only to pick his brain for more of his expertise, but to attempt to repay the influence his guidance had on my career by pursuing the projects that he will lead now.

Phil took the reins of overseeing me after Jiun-Haw left, and although our projects were not as related, I still constantly picked his brain as to how to conduct myself as a scientist. Observing his expertise in performing high-precision low-temperature measurements made me realize that if you want to do a precise measurement correctly, there are no shortcuts. What I value more from my shared time with Phil was our friendship though, and the memories of our adventures both in Palo Alto and abroad (domestically) at conferences from Baltimore to San Fransisco.

I probably owe the largest debt of gratitude to Matthias. His presence transformed the Fisher Lab, as now more than half the projects that we are pursuing are due to his experimental innovations. This includes the last chapter of my thesis, for which we have worked side by side (my part being me mostly following his instructions), and from this experience I've learned so many fundamental aspects of how to develop and conduct a proper experiment. But just as with Phil, I value my friendship with Matthias even more. I sit here writing these acknowledgements from his apartment, as he has generously let me stay here the past two weeks as I finish my work up at Stanford. (Hopefully we can find his garage opener I accidentally misplaced, it has to be at Safeway.) But it is this generosity and compassion that make Matthias an incredible friend, and for that I am very grateful. I hope we continue to compete and laugh and collaborate as my career moves on.

In my nearly 7 years in the Fisher Lab, I worked with many grad students which helped me to get here: Paula Giraldo-Gallo, Max Shapiro, Alex Hristov, Johanna Palmstrom, Joshua Straquadine, Patrick Worasaran, Matthew Sorensen, Kaan Alp Yay, and Anisha Singh.

Although my shared time was short with Paula, I still remember when she first taught me how to do glasswork, and I hope I've been able to carry on her glasswork technique and knowledge to the next generation of the Fisher Lab.

Max is one of the nicest, yet emotionally strongest friends I have. He's been there for me from when I started, giving me advice whenever I asked, helping me from my qual exam to my thesis presentation. I've enjoyed our conversations ranging from group theory to politics to basketball, and I hope we continue them as I move on from the lab. Working with Alex was challenging and

inspiring, as he is one of the sharpest people I've ever met, with a knack for picking up theoretical physics topics (like group theory) immediately.

Both Johanna and Josh transferred in from other labs, and were very welcome additions to the lab. I really enjoyed the late night conversations with Johanna and going to the Axe and Palm for ice cream sundaes. Both of them are very impressive scientists, Johanna with her attention to detail and contacting prowess, and Josh with his ability to design, develop, and implement an experiment from scratch. I have no doubt you guys will be very successful in your future scientific endeavors.

Patrick started a year after me, and our friendship grew as we bonded over dealing with ups and downs of working in an experimental lab, as well as the inevitable ebbs and flows of motivation during a Ph.D program. Patrick is a multi-talented man, from piano to ping-pong to cooking, and he has inspired me to develop some of those skills (although it seems hopeless that I will ever be as a good of a ping-pong player as him). I can remember our conversation from 5 years ago wondering if we could make it through this, but look at us now.

I want to thank Matt for his help during the Maglab trip we went on. I've also enjoyed our intellectual sparring on politics and octupoles (although I didn't enjoy getting beat down in chess). I'd like to think we both shifted our viewpoints slightly in response to the other's persuasive arguments, but I have a feeling only I really did.

To the young guns Kaan and Anisha, I know the lab is in good hands. I've really enjoyed my conversations with Kaan, from physics to politics to discussing his homeland of Turkey. Anisha, keep pushing through with fixing the MPMS, it will work eventually (I hope).

I want to thank my core group of friends at Stanford: Tyler Whittle, Ben Whittle, Gabriel Maher, Sam Corbett-Davies, Sean Mclaughlin, and my long-term roommate Ben Nosarzewski. I know they are surprised I made it this far, but I did. I want to thank them for tolerating my antics, and it is because of our numerous adventures and misadventures that I stayed sane. To my high school friends: Michael Shen, Han Shi, and Yohanna Hanna, long live the platoon.

Finally and most importantly, I want to thank my family. To my siblings, my twin brother Kyle and my younger sister Shelby, I hope this makes you as proud as I am of the progress and accomplishments you've made in your respective fields. My brother was a constant source of understanding, commiserating, laughter, and motivation. Let's keep on our grind Kyle.

Of course I am incredibly grateful for the support of my parents. Without their constant motivation and help and love I never would made it even to Stanford, let alone to finishing my Ph.D. I hope this makes you proud, and I love you so much. I dedicate this thesis to you.

R.I.P Kobe. I will continue to embrace the mamba mentality in my future career.

Contents

Preface **iv**

Acknowledgments **vi**

1 Introduction **1**

1.1 Overview: Motivation and Context 1

1.2 Multipoles 4

1.3 Group theory 5

1.3.1 Applications of group theory to $TmAg_2$ and $YbRu_2Ge_2$ 11

1.4 Hamiltonians of local $4f$ orbitals 13

1.4.1 H_{CEF} 13

1.4.2 H_{ZEE} 15

1.4.3 H_{MM} 16

1.4.4 E_{el} 16

1.5 Cooperative Jahn-Teller ferroquadrupolar transitions from H_{QQ} and H_{ME} 16

1.6 The Ising Model and its application to ferroquadrupole order 19

1.6.1 The Ising Model 19

1.6.2 Transverse field Ising model 20

1.6.3 Mapping of the low energy effective Hamiltonian of $TmAg_2$ to the Transverse field Ising model 24

1.6.4 Applying the Transverse Field Ising model: Strain derivatives of T_Q 25

1.6.5 Ising model applied to $YbRu_2Ge_2$ 28

2 Experimental Methods **32**

2.1 Crystal Growths of $TmAg_2$ and $YbRu_2Ge_2$ 32

2.1.1 $TmAg_2$ 32

2.1.2 $YbRu_2Ge_2$ 33

2.2 Elastoresistivity with microstructuring 33

2.2.1 Transverse Elastoresistivity 33

2.2.2 Elastoresistivity measurements in magnetic fields using the Montgomery technique . . . 35
2.3 Elastocaloric Effect . . . 37
2.3.1 Physical Origin of the Elastocaloric Effect . . . 37
2.3.2 Elastocaloric Experimental setup . . . 40

3 Divergence of the quadrupole-strain susceptibility of the electronic nematic system $YbRu_2Ge_2$ 45
3.1 Abstract . . . 45
3.2 Introduction . . . 46
3.3 Materials and Methods . . . 51
3.4 Results . . . 52
3.5 Summary and Discussion . . . 58
3.6 Supporting Information (SI) . . . 58
3.6.1 CEF splitting of the J=7/2 Hund's rule multiplet of $YbRu_2Ge_2$ . . . 58
3.6.2 X-ray diffraction data for $YbRu_2Ge_2$ . . . 59
3.6.3 Quadrupole operators . . . 60
3.6.4 Quadrupole-strain Susceptibility . . . 63
3.6.5 Relation of Elastoresistivity to Quadrupole-strain Susceptibility . . . 65
3.6.6 Linearity of the B_{1g} elastoresistivity . . . 67
3.6.7 Non-linearity of the A_{1g} elastoresistivity . . . 67
3.6.8 Focused Ion Beam parameters . . . 69
3.6.9 Crystal Growth . . . 70

4 Effect of magnetic field on Ferroquadrupolar Order in $YbRu_2Ge_2$ 71
4.1 Abstract . . . 71
4.2 Introduction . . . 72
4.3 Experimental Methods . . . 73
4.4 Results . . . 73
4.4.1 Phase diagram . . . 73
4.4.2 Resistivity proximate to the critical field . . . 76
4.4.3 Elastoresistivity as a function of field and temperature . . . 77
4.5 Discussion . . . 80
4.5.1 Magneto-elastoresistivity . . . 80
4.5.2 Relating to quadrupole-strain susceptibility . . . 83
4.5.3 Field-dependence of g . . . 84
4.5.4 Resistivity . . . 85
4.6 Conclusion . . . 85

5 Elastocaloric and transport properties of $TmAg_2$ **87**
5.1 Introduction . . . 88
5.1.1 Background on $TmAg_2$ . . . 88
5.1.2 Strain in $TmAg_2$ . . . 89
5.1.3 Model Hamiltonian for $4f$ degrees of freedom . . . 90
5.2 Experimental Methods . . . 91
5.3 Results and Discussion . . . 92
5.3.1 Heat Capacity . . . 92
5.3.2 Elastocaloric Effect . . . 96
5.3.3 Resistivity . . . 103
5.4 Conclusion . . . 106

6 Conclusion **109**

Bibliography **111**

List of Tables

1.1 **The multipoles up to the 3rd order, with their corresponding Steven's operators.** The Stevens operator notation will be used for the remainder of this thesis, as it connects the multipoles to their angular momentum operator representations. The linear combinations of the spherical harmonics that produce these Stevens operators also classify neatly into separate irreducible representations for D_{4h}, which will be discussed in Section 1.3. $F(J_z, J) = 5J_z^2 - J(J+1) - \frac{1}{2}$. 6

1.2 **Character table for the point group symmetry $\mathbf{D_{4h}}$.** The rows are all of the irreducible representations, which match the number of classes in the group. The columns are the classes of elements in D_{4h}. A class/column may have multiple elements in it (the second column $2C_4$ refers to the rotations by 90 degrees and -90 degrees,) and because they belong to the same class by definition they have the same character for all representations. The character rows are orthogonal when all 16 elements are considered. Note that the irreducible representations with a subscript u act with a negative sign under inversion, whereas those with g have a positive sign. 9

1.3 **The irreducible representations of strain for $\mathbf{D_{4h}}$ and the conjugate quadrupoles.** For D_{4h} two distinct strains span the A_{1g} representation, we have chosen a convenient basis which differentiates in-plane from out-of-plane strain. 17

List of Figures

1.1 **The tetragonal crystal structures and unit cells of $TmAg_2$ on the left and $YbRu_2Ge_2$ on the right.** For $TmAg_2$ the lattice constants are: a=b=3.652Å, c=9.164Å and for $YbRu_2Ge_2$: a=b=4.8Å, c=9.2Å. The space group for these materials is I4/mmm. Both materials will be introduced in greater detail in Chapters 3 and 4. 8

1.2 **A visual depiction of the relevant energy scales for the $4f$ electrons in the $TmAg_2$.** The CEF state energies, which are proposed from previous neutron diffraction experiments [3], are not to scale and have been expanded for clarity. This work will only focus on energy scales at and below H_{CEF}. $YbRu_2Ge_2$ would have a similar diagram but with different multiplicities (different Js) and a different CEF spectrum. 14

1.3 **The phase boundary for the mean-field transverse field S=1/2 Ising model.** Notice in the proximity of H_c that the phase boundary is very steep, making this a difficult phase diagram to be experimentally investigated. 22

1.4 **The order parameter susceptibility vs. temperature for different values of tranvserse field H_x.** Here $nJ = 1$, so $T_Q(H_x = 0) = 0.25$, and $H_c = 0.5$. 23

1.5 **Calculated B_{2g} strain derivative of T_Q plotted as a function of the reduced magnetic field (blue dots).** A power law fit in the proximity of A_c is shown as a yellow line. The scale of the y-axis is arbitrary, although the sign is fixed to be negative by the nature of a transverse field. 27

1.6 **Calculated A_{1g} strain derivative of T_Q plotted as a function of the reduced magnetic field (blue dots).** A power law fit in the proximity of A_c is shown as a red circles. The scale of the y-axis is arbitrary, and the sign has been arbitrarily chosen to match empirical data. 27

1.7 **Calculated mean-field phase diagram for the quasi-quartet described in the main text.** This model is appropriate to describe the low temperature properties of the ferroquadrupolar phase transition of $YbRu_2Ge_2$ with applied magnetic field. The scale of the magnetic field is set such that without a gap $H_c = 10T$, although the quasi-quartet gap estimated in Chapter 4 to be $\Delta_o = 3.6K$ pushes the critical field out further. 31

2.1 **Scanning electron micrograph of a representative micro-structured sample used for transverse elastoresistance measurements.** The $YbRu_2Ge_2$ sample is glued to a 50 μm thick Si substrate. The crystal axes (indicated by black arrows) were previously determined by x-ray diffraction, and identified here by the horizontal facets. Line cuts were etched using a Focused Ion Beam to control the current path (indicated by yellow arrow) and precisely define the voltage contact positions (labelled V_1 through V_4) 36

2.2 **Representative micro-structured sample used for Montgomery-style elastoresistance measurements in magnetic fields.** The $YbRu_2Ge_2$ sample is glued with Angstrom Bond to a 50 μm thick Si substrate. Line cuts were etched using a Focused Ion Beam to control the current path and precisely define the voltage contact positions such that they are at the corners of a 150μm by 150 μm square. The yellow lines are used to guide the eye to the cuts made to separate the contacts, and those contacts were formed with H-20E silver epoxy. 38

2.3 **Schematic of the elastocaloric experimental setup.** The top picture represents a side view of the sample secured between the jaws of the strain cell, and this figure was taken from Ref. [8]. The bottom schematic represents the top view before the final top set of mounting plates are positioned. The black semi-circles represent the Stycast epoxy, which secures the edges of the sample to both the bottom and top sets of mounting plates. The orange lines represent the thermally resistive constantan wires which electrically connect the thermometer's contact pads (represented by yellow rectangles) to the corresponding resistors' contact pads of the Wheatstone Bridge, which is thermally anchored to the strain cell in reality, expanded in the lower left hand corner. V_s is the source voltage for the bridge, and V_B is the output voltage of the bridge which isolates the temperature fluctuations of the thermometer and sample. The parts of the Wheatstone bridge where the resistors' contact pads touch represent electrical contacts. Notice that the stress is aligned along (1 1 0), so this is a B_{2g} measurement. 42

3.1 **Effect of strains of different symmetries on the CEF eigenstates of $YbRu_2Ge_2$, and measurement of the associated elastoresistivity coefficients.** Strains corresponding to distinct irreducible representations, induced by external stresses, are indicated by thick black arrows. These strains admix and split the CEF eigenstates; the effect on the low energy CEF quasi-quartet and the charge density of the ground state orbitals is illustrated. For simplicity, the Γ_6 and Γ_7 eigenstates are illustrated for pure $|\pm 1/2\rangle$ and $|\pm 3/2\rangle$ character respectively (see main text). The far right column shows the required orientation of the normal strain (thick black arrows), crystal axes (insets to grey schematic crystals) and voltage contacts (yellow pads, with measured voltages indicated for longitudinal and transverse pairs) for measurement of the associated elastoresistivity coefficients in each symmetry channel. 48

3.2 **Scanning electron micrograph of a representative micro-structured sample used for elastoresistance measurements.** The $YbRu_2Ge_2$ sample is glued to a 50 μm thick Si substrate. The crystal axes (indicated by black arrows) were previously determined by x-ray diffraction, and identified here by the horizontal facets. Line cuts were etched using a Focused Ion Beam to control the current path (indicated by yellow arrow) and precisely define the voltage contact positions (labelled V_1 through V_4) 53

3.3 **Orthorhombicity of $YbRu_2Ge_2$** The order parameter of the orthorhombic structural phase transition is plotted against temperature. A mean-field Ising order parameter that becomes finite is 10.2K is overlaid as a guide to the eye. Insets illustrate the charge density of the $4f$ CEF quasi-quartet groundstate of $YbRu_2Ge_2$ in the tetragonal phase (green, with 4-fold symmetry), and that of the orthorhombic phase (red, with two-fold symmetry) . Ferroquadrupole order of the $4f$ orbitals is inferred from the observed orthorhombicity. 54

3.4 **Temperature dependence of the resistivity of $YbRu_2Ge_2$.** The resistivity (purple data points) and its derivative with respect to temperature (green data points) show clear features at T_Q (marked by vertical dashed line), as well as T_{N1} and T_{N2}. Slight differences in estimates of the critical temperatures relative to values extracted from x-ray diffraction measurements are attributed to differences in sweep rates of the two measurements. Inset shows the resistivity over a larger temperature range, in which a different $YbRu_2Ge_2$ single crystal is measured. Data are also shown for the non-magnetic analog, YRu_2Ge_2, for which no phase transitions are observed. Yttrium has an empty $4f$ shell but otherwise the electronic structure of the two materials is anticipated to be very similar, and differences in the resistivity between the two compounds are primarily attributed to $4f$ scattering. 56

3.5 **Temperature dependence of the elastoresistivity of $YbRu_2Ge_2$ in the B_{1g} and B_{2g} symmetry channels.** As described in the main text, these quantities (shown by blue and black data points respectively) are proportional to the quadrupole strain susceptibility of the same symmetry channels. Inset shows the inverse of the quadrupole strain susceptibility $(-\chi_{B_{1g}}-\chi_0)^{-1}$ for the B_{1g} channel having subtracted a temperature-independent offset $\chi_0 = 4.48$. Red lines in the main panel and inset show fit to a Curie-Weiss functional form, with fit parameters described in the main text. The Weiss temperature is found to be 0 K within experimental error. Vertical dashed lines indicate T_Q, separating tetragonal (blue) from orthorhombic (red) phases. 57

3.6 **$YbRu_2Ge_2$ CEF spectrum** Spin-orbit coupling determines the ground state electronic mulitplet to have J=7/2, which is split by the surrounding crystalline potential to have 4 doublets, the lowest two in energy forming a quasi-quartet split by roughly 10K. 59

3.7 **Surface plot of log(intensity) at 12.2K** The material is still clearly tetragonal here, although it is displaying some spread in the momentum space direction that orthorhombic domains are expected, possibly indicating critical fluctuations or a static response to unintentional strains from securing the crystal to the sample holder. . . 60

3.8 **Surface plot of log(intensity) at 6.6K** The material is clearly orthorhombic at this temperature, displaying multiple peaks. 61

3.9 **Line cut of log(counts) along the (1,1,0) direction, centered at (6,0,0)** The dotted lines represent where the first moment of counts was determined to be, which was normalized by the lattice parameters to determine the orthrorhombic order parameter. 61

3.10 **Strain dependence of the B_{1g} elastoresistivity response** The B_{1g} quadrupole-strain susceptibility displays little sensitivity to tuning B_{1g} offset strains above the quadrupolar phase transition indicating this channel is dominated by linear behavior, and hence $\left(\frac{\Delta\rho}{\rho}\right)_{B_{1g}}/\Delta\varepsilon_{B_{1g}}$ provides a good measure of the linear elastoresistivity coefficients for this symmetry channel, m_{11}-m_{12} 67

3.11 **Non-linearity of the A_{1g} response with respect to B_{1g} strain.** The A_{1g} quadrupole-strain susceptibility displays striking sensitivity to tuning offset B_{1g} strains above the quadrupolar phase transition. 68

3.12 **Non-linearity of the A_{1g} response with respect to B_{2g} strain.** The A_{1g} quadrupole-strain susceptibility displays small sensitivity to tuning offset A_{1g} and B_{2g} strains above the quadrupolar phase transition 69

4.1 **Identification of critical temperatures of the ferroquadrupolar and magnetic phase transitions in $YbRu_2Ge_2$ from RvT and RvH measurements.** The left panel (a) displays the RvT traces obtained in magnetic fields from 0T to 27T spanning 0.35K to 12K. The color scale goes from blue to red with increasing magnetic field. The kinks at the ferroquadrupolar phase transitions can be seen easily for fields below 20T, smoothly being suppressed towards 0K. The steepness of the phase diagram prevents lower temperature ferroquadrupolar phase transitions from being easily observed in coarsely spaced RvT traces. The right panel (b) displays RvH traces at temperatures spaced from 0.35K to 1.6K. The phase transition at 21.3 ± 0.2 T is easily observed at 0.35K and 0.8K, but seems to be replaced by a prominent cusp at higher temperatures. At temperatures above 2K this cusp was no longer is seen as prominently however. 74

4.2 **H-T phase diagram of $YbRu_2Ge_2$.** The top left panel illustrates the CEF ground state quasi-quartet for $YbRu_2Ge_2$ and how the spontaneous ferroquadrupolar phase transition mixes and shifts the spectrum. Quadrupolar matrix elements between the excited Γ_7 doublet and the Γ_6 doublet mix their states, and the corresponding gap adds in quadrature with the CEF gap Δ_o. The low temperature states are still doublets as time-reversal symmetry hasn't been broken. The right frame displays the low-temperature energy spectrum when magnetic field is applied. The quadrupolar doublets split back into to the m_j eigenstates, and at high enough fields the ferroquadrupolar order is destroyed. The lower panel shows the H-T phase diagram as inferred from resistivity measurements. The closed symbols represent phase transitions measured for a sample at the Maglab in a 35T resistive magnet, the open symbols from a different sample in a 14T PPMS at Stanford University. Blue squares denote the ferroquadrupolar phase transition, and the blue shading represents when the crystal structure is no longer tetragonal. The red circles denote the anti-ferromagnetic phase transition, and the green triangles represent a proposed spin re-ordering phase transition. The signature for the low-temperature spin re-ordering wasn't resolved in the resistivity derivatives above 14T. The ferroquadrupolar phase boundary is consistent with a mean-field Hamiltonian as in Eq. 4.1 with a quasi-quartet gap of $\Delta_o = 3.5K$. 75

4.3 **Power law behavior of the resistivity proximate to the crtical field H_c.** The left plot displays the temperature derivative of the resistivity for fields at and above the critical field at temperatures from 0.35K to 1.75K. Each trace is fit to a line from 0.5K to 1.5K, as there is deviation from linear behavior below 0.5K. Linear behavior indicates a quadratic T-dependence of the resistivity. There is a robust increase in the slope (the quadratic coefficent for the resistivity) as the field approaches the critical field. The quadratic coefficients are plotted as the blue points in the right plot as a function of field, and these coefficients were extracted from the low temperature RvH traces, allowing high data density. The open blue points are also the extracted quadratic coefficents for data below the critical field, but the overall power law behavior of the resistivity ($\rho = \rho_o + AT^b$, b plotted by the red dots) below the critical field indicates that a high power law relation describes the low temperature resistivity more accurately. Above the critical field however the resistivity approaches $\rho = \rho_o + AT^2$ as the critical field is approached. 76

4.4 **Field-dependence of the T-dependence of the elastoresistivity of $YbRu_2Ge_2$.** B_{1g} Elastoresistivity data for magnetic fields from 0T (blue) to 14T (red) are shown. There is a robust increase in the magnitude with magnetic field, which was seen in multiple samples. The traces diverge towards higher temperatures as well as magnetic field is increased. This can be seen more clearly in the lower right inset graph, which depicts the reciprocal of each trace (minus a small temperature independent offset). The inverse traces appear to be just vertically offset from each other, and the offset is a monotonic function of field. This would correspond to an increase of Weiss temperature with field, given these traces were interpreted as belonging to a Curie-Weiss functional form. The lower middle diagram depicts the geometry of the experiment: anti-symmetric strain is applied to the crystal (via applying voltage to the piezoelectric device) in the ab plane along the (1 0 0) and (0 1 0) axes, and the sample's resistivity is measured via a Montgomery geometry along those same axes. In reality the Montgomery square was microstructured to precisely define the resistivity measurements. Magnetic field was applied along (0 0 1). 78

4.5 **Quadratic field-dependence of the elastoresistivity of $YbRu_2Ge_2$ at fixed temperatures.** The left plot is the measured B_{1g} elastoresistivity coefficient from -14T to 14T at 11K. There is very little contamination of field-odd terms, and it is described well by a quadratic field coefficient from -5T to 5T, with the quadratic fit shown by the dashed red line. This coefficient is plotted as a function of temperature in the right plot (blue dots) along with various simulated results with different octupolar coefficents in the mean-field Hamiltonian. The black dashed line represents the "octupolar susceptibility", or the second field derivative of the B_{1g} susceptibility, if there are no octupolar contributions to the Hamiltonian. The sign is positive even though the initial quadrupole-strain susceptibility is fixed to be negative, this signifies that the magnitude of the quadrupole-strain susceptibility reduces in field with no octupoles, as expected. The orange dashed line represents a Hamiltonian with only an additional bilinear octupolar coupling with no mean-field interactions, and it does not explain the faster divergence in the data. Finally the red dashed line is the quadrupole-strain susceptibility of a Hamiltonian that incorporates an octupole-octupole interaction term to be able to accurately describe the data. 79

5.1 $4f$ **Heat capacity of $TmAg_2$ compared to simulations with "built-in" strains.** The left panel displays a schematic of the single-ion energy spectrum showing the lowest three CEF energy states of the 4f electronic multiplet that were simulated with a model Hamiltonian with previously determined parameters. Bold symbols show the energy eigenvalues from a simulation with an appropriate longitudinal strain of order 10^{-4} to simulate the broadening of the system's heat capacity (see main text). Open symbols show results of a simulation that doesn't incorporate an applied strain, such that the splitting of the Γ_5 ground-state doublet onsets at 5K. The inset displays the order parameter dependence on temperature for both unstrained (black line) and strained simulations. The right panel displays the measured zero-field heat capacity data for $TmAg_2$ (black dots), isolating the $4f$ electronic component of the heat capacity. This was done by subtracting the heat capacity of YAg_2, in which the Y^{3+} ion acts chemically identical to the Tm^{3+} ion but has an empty 4f shell. The blue symbols are simulated heat capacity results including three B_{1g} strains as a fit parameters. The phase transition temperatures in the simulations were determined by the mean-field interaction constants $B^2/C + K$, which were chosen so the system had a critical temperature $T_Q = 5K$. This simulated heat capacity is the linear combination: $0.634C_p(\varepsilon_1) + 0.23C_p(\varepsilon_2) + 0.136C_p(\varepsilon_3)$ where $\varepsilon_1 = 0.007\%$, $\varepsilon_2 = 0.1\%$, and $\varepsilon_3 = 0.7\%$. The results of a simulation featuring a Hamiltonian with no "built-in" strains, and consequently a sharp mean-field step, are shown in red. 93

5.2 **Variation of the temperature dependence of the heat capacity with applied magnetic field.** Data are shown for fields ranging from 0-5T, with vertical offsets for clarity (no offsets for $H = 0T$). T_Q is marked by a black dotted line, showing its progressive suppression with increased magnetic field H_z. 94

5.3 **Interpolated color map of the temperature derivative of the $4f$ heat capacity in the H-T plane.** The dotted line shows a mean-field transverse Ising fit of a phase boundary with $T_Q = 5K$ at zero field and $H_c = 3.1T$ at 0K. 95

5.4 **Elastocaloric and heat capacity measurements of $TmAg_2$ at 0T (left panels) and 2.7T (right panels).** The top two graphs depict the heat capacity of $TmAg_2$ including the phonon contribution at 0T and 2.7T. The graphs below depict the elastocaloric effect via applying an AC stress along (1 1 0) for identical magnetic fields applied along the c-axis. The units of these graphs represent the temperature change in Kelvin of the thermometer attached to the sample per 100% strain applied to the sample. The actual peak-to-peak strain used for the measurements was closer to 0.01%. The phase transition, which occurs at temperatures denoted by the vertical black dashed lines, is marked by a discontinuity in the elastocaloric effect for both fields as described in the main text. 98

5.5 **Temperature dependence of the elastocaloric effect for different magnetic fields.** Elastocaloric data, measured while applying an AC stress along (1 1 0) while sweeping temperature from 20K to 2.3K, is plotted for magnetic fields applied along the c-axis from 0T (blue) to fields above the critical field of $3.32T \pm 0.1T$ (red). The ferroquadrupolar phase transition manifests in jumps in the elastocaloric traces, and the H-T phase boundary obtained by these signatures is plotted in the inset graph. The red dashed line in the inset is a mean-field transverse field Ising boundary with $T_Q(0T) = 4.8K$ and $H_c(0K) = 3.32T$. To the lowest temperatures measured in this study, the phase boundary follows mean-field expectations. 100

5.6 **Strain derivative of T_Q with respect to ε_{xy} as a function of magnetic field.** The black symbols are obtained by taking the ratio of the magnitude of the elastocaloric jump (Δ_{EC}) at the phase transition over the magnitude of the corresponding jump of the heat capacity, and multiplying by C_p^{tot}. These jumps are measured at finite strain, and the zero-strain jump is subtracted to obtain just the part proportional to the second derivative of T_Q with respect to $\varepsilon_{B_{2g}}$, as described in the text. The error bars represent the errors from extracting the magnitudes of the jumps in the elastocaloric effect and the heat capacity. These errors were estimated by using many linear fits of the quantities below and above the phase transition temperature, and extracting the range of the differences between the fits extrapolated to the phase transition temperature. The data points representing the strain derivatives shown are positive because the offset strain applied was compressive ($\sim -0.25\%$), and it multiplied the second derivative $\frac{d^2T_Q}{d\varepsilon^2_{B_{2g}}}$, which is negative since B_{2g} strain functions as a transverse field. The red dashed line is a fit from Eq. 1.49, which comes from solving the transverse-field Ising model for the derivative of the phase transition temperature as a function of the orthogonal transverse field. The measured values are consistent with this mean-field model. 101

5.7 **The B_{2g} quadrupole-strain susceptibility as probed by the elastocaloric effect.** The left panel displays elastocaloric data, normalized to display the strain multiplied by the temperature derivative of the nematic susceptibility, measured at a fixed DC strain with different magnetic fields. The dotted lines are the expected fit for the susceptibility in an Ising model with a transverse field applied, although the proportionality constant is allowed to vary and almost doubles from its value at 0T to its value at 4T. The effective Weiss temperature for this susceptibility is found to be $T^*_{B_{2g}} = 2.6K$, although if the proportionality constant is fixed then this quantity will vary in the fits from 2 to 3K as field is increased. The right panel displays the temperature dependence of the elastocaloric effect as different DC strains are induced in the sample. The black dataset represents the data which is set to a strain closest to zero-strain, yellow-green traces represent compressive strain conditions, and the orange data is collected in tensile strain. The effect is linear with strain at all temperatures for this strain range, as expected from Eq. 5.6. Notice that the magnitude of the jump at 5K varies significantly with offset strain, this is expected as well from Eq. 5.5. The inset graph displays T_Q extracted from the jumps as a function of DC strain, which exhibits a linear dependence of 0.3K/% of applied strain. 104

5.8 **Evolution of the temperature dependence of the resistivity of $TmAg_2$ as a function of magnetic field.** Resistivity data are shown for representative fields from 0T-8T, although much finer field spaced data were collected and then used to construct the interpolated color plot shown in Figure 5.9. As described in the main text, the signature of the phase transition in the resistivity is smeared and reduced in temperature as magnetic field increases. The temperature dependence of the resistivity flattens out progressively below the transition as the field gets close to the critical field. Above the critical field the temperature dependence of the resistivity is seemingly described by the integral of Schottkey terms (see main text and Figure 5.9). 106

5.9 **Interpolated color-scale plots of both C_p (left panel) and $\frac{d\rho}{dT}$ (right panel) in the H-T plane.** Both the shape of the phase transition and the signature of a Schottkey-like anomaly appear very prominently and similarly in both quantities. . . 107

Chapter 1

Introduction

1.1 Overview: Motivation and Context

One facet of the study of condensed matter physics involves probing emergent properties of materials, particularly of the degrees of freedom in a system that cooperatively cause phase transitions. Phase transitions are characterized by the spontaneous appearance of an order parameter which breaks an existing symmetry (symmetries) of the material. While phase transitions may have subtle and hard-to-measure effects for a lot of material properties, they can be robustly classified by the symmetry that they break. The different symmetries of the ordered vs. disordered states are relevant for both the thermal and quantum fluctuations of the order parameter, and the latter may dominate transport and thermodynamic properties for the material at temperatures approaching absolute zero. Of particular relevance to the work described in this thesis, the alignment of complex local electron density distributions can be defined through the spontaneous development of a term in the multipole expansion of the charge/current distribution, which is fixed to break certain symmetries by the definition of that multipole. For instance the simplest example of multipole order is local moment ferromagnetism, in which local magnetic dipoles align collectively to break time-reversal symmetry. The multipolar order observed in the $4f$ intermetallics $TmAg_2$ and $YbRu_2Ge_2$, the materials studied in this thesis, is characterized by the alignment of higher order local multipolar degrees of freedom, namely electric quadrupoles, which break the rotational symmetry of the host tetragonal crystal lattice. These low temperature ferroquadrupolar phase transitions can be suppressed towards 0K, offering avenues towards studying materials in regimes where quantum fluctuations may dominate the properties of system, also known as the quantum critical regime. Quantum criticality in general is a topic of considerable current interest from both a theoretical and experimental perspective, yet relatively little has been studied of the potential consequences of the suppression of ferroquadrupolar phase transitions. Futhermore, from a symmetry perspective, these transitions are specific realizations of electronic Ising-nematic phase transitions (exhibited, for example, by several Fe-pnictide

superconductor families [1]), as they spontaneously lower the in-plane C_4 rotational symmetry to C_2. Therefore this work is motivated not only in its contributions to understanding multipolar phase transitions and associated quantum criticality, but also from its connection to aspects of the phase diagrams of certain high Tc superconductors.

The Ising-nematic phase transitions occur at relatively low temperatures for these $4f$ ferroquadrupolar materials. This implies experimentally accessible tuning parameters for suppressing these transitions to 0K, and empirically this is the case for magnetic field, as shown in this work. Although applying a magnetic field may preclude the emergence of a superconducting phase near the completely suppressed phase transition, it still allows transport and thermodynamic measurements in the vicinity of the nematic quantum critical point, which appear in Chapters 4 and 5. More generally, the fluctuations of multipoles in these systems are easily tuned with non-disorder inducing parameters like magnetic field and strain, and so offer unique opportunities to study multi-dimensional phase diagrams of multipolar order. Because the microscopic details of local $4f$ electrons in similar intermetallic compounds have been heavily researched and well understood since the 1970's, $TmAg_2$ and $YbRu_2Ge_2$ truly serve as model materials in which terms in the Hamiltonian can be written down that precisely explain the nematic and multipolar susceptibilities/order observed that arise from thermal fluctuations [2]. These models, however, don't consider how the metallic degrees of freedom interact with the potentially quantum critical localized $4f$ lattice, and so any deviations that arise from quantum criticality can be isolated and are of considerable interest.

Both $TmAg_2$ and $YbRu_2Ge_2$ undergo ferroquadrupolar phase transitions, occurring at 5K and 10.2K respectively [3, 4]. The local $4f$ electronic multiplets, which for both the Tm^{3+} and the Yb^{3+} ions can harbor quadrupolar degrees of freedom, develop spontaneous electronic quadrupolar moments which collectively align at these phase transitions. The macroscopic quadrupolar order parameter breaks the four-fold rotational symmetry of the lattice, and so the lattice distorts in a similar fashion due to its coupling to the order parameter. Herein lies a crucial point: because strain, which represents the internal degree of freedom of the lattice to distort, is a second-rank tensor quantity (strain is defined as the symmetric spatial derivative of a displacement vector), it couples bilinearly to the quadrupoles of the same symmetry which are the second-order multipoles. This coupling guarantees that for a finite applied strain of the appropriate symmetry there will be a non-zero induced quadrupolar moment, and vice versa. In fact any second-rank tensor quantity, for instance the resistivity tensor, is governed by similar symmetry constraints and thus guarantees a response if a strain is applied or a quadrupolar moment becomes non-zero. This establishes the power of experiments which apply/induce strain to probe quadrupolar fluctuations. These experiments directly apply the conjugate field of the order parameter, and can also obtain a precise response by symmetry decomposition of the measured quantities. As I will show, this insight is at the heart of the elastoresistivity technique as a probe of quadrupole-strain susceptibility.

In this work I will present the results of several novel strain based experiments on these materials.

Chapter 3 will be dedicated to elastoresistivity measurements of $YbRu_2Ge_2$, in which the proportionality between applied strain and induced antisymmetric resistivity change grows significantly in the B_{1g} $(x^2 - y^2)$ symmetry channel as temperature is decreased. This confirms that the B_{1g} quadrupole-strain susceptibility diverges as the ferroquadrupolar phase transition is approached, and the specific details of the temperature dependence (near perfect Curie-Weiss fit with $\theta = 0 \pm 2K$) allow us to narrow down the driving mechanism to be a mean-field quadrupole-quadrupole interaction term mediated by the lattice, rather than mediated by the conduction electrons. We return to elastoresistivity measurements of $YbRu_2Ge_2$ in Chapter 4, but now apply large magnetic fields (up to 30T), which completely suppresses the ferroquadrupolar phase transition at a critical field $H_c \approx 21.3T$. We map the magnetic field phase diagram of $YbRu_2Ge_2$ via resistivity measurements, and observe potential consequences of quantum criticality at low temperatures above H_c. Excitingly, there is an anomalous increase in the elastoresistivity as field increases towards H_c, which can be potentially explained by incorporating octupolar terms (allowed in the ground-state quasi-quartet of $YbRu_2Ge_2$) into the mean-field Hamiltonian. This establishes magneto-elastoresistivity measurements as a probe of octupolar degrees of freedom, which would be one of the first measurements to do so. A second technique I have helped to develop and apply for the first time to this set of materials is the elastocaloric effect. Chapter 5 will focus on elastocaloric measurements of $TmAg_2$, in which the change in electronic entropy induced by strain is measured as a temperature change, which changes sharply at the ferroquadrupolar phase transition. Because this material only undergoes a ferroquadrupolar phase transition, and also because of the simplicity of its $4f$ electronic ground state doublet, the elastocaloric measurements present a persuasive case that both strain and magnetic field act as effective transverse fields in a mean-field Ising model, which would guarantee both strain and magnetic field induce quantum critical points (and a quantum critical line between them in this material). In addition, I present the results of heat capacity and resistivity measurements in the proximity of the putative field-induced quantum critical point, and comment on an apparent quasi-proportionality between $\frac{\partial \rho}{\partial T}$ and C_p that appears throughout the phase diagram. More generally, I hope these results convey the power of strain-based measurements particularly in measuring multipolar fluctuations/order, and the utility in using these model multipolar systems to study exciting and relevant condensed matter problems, such as investigating the effects of nematic quantum criticality.

The rest of this introduction will be devoted to providing the necessary knowledge to understand these results, as well as focus on topics that I find to be particularly useful in appreciating the broader context of these experiments. To set the stage for why localized multipole moments exist in these materials, it is necessary to understand both the relevant $4f$ energy scales and the finer details of multipolar expansions, which will be covered next. There will be a brief detour into group theory to motivate which moments are allowed and which are not, as well as to be able to connect these systems to the well known statistical mechanics Ising models. The introduction will end with

an in-depth look at some of the terms in a $4f$ Hamiltonian to see the consequences for multipolar susceptibilities/order in these materials.

1.2 Multipoles

A multipolar expansion can be used in general to describe the angular distribution of a 3D spatial function. In the context of this work it will be used to describe the shape of electron density or magnetic charge (current) density, particularly of localized electron orbitals/electronic multiplets. By writing the full charge density into a sum of multipole terms, this expansion will allow a symmetry decomposition of relevant interactions and their energy scales. The multipole expansions we will consider use the spherical harmonics as a basis. Consider an arbitrary local distribution of charge (i.e a $4f$ electronic multiplet), which can be written as a series of terms:

$$\rho(\theta,\phi,r) = \sum_{l=0}^{\infty}\sum_{m=-l}^{l} C_l^m Y_l^m(\theta,\phi) R_l(r) \tag{1.1}$$

Where Y_l^m are the usual spherical harmonics and C_l^m are coefficients appropriate for the point charge distribution. The radial part of the multipoles is described by $R_l(r)$. Because the integer l spherical harmonics are a complete basis in SO3, any charge distribution can be completely described by a sum of multipole moments. One way to derive the functional form of the multipoles is to solve Laplace's equation in spherical coordinates, and consider only the angular parts of the solutions.

$$\nabla^2 f = \frac{1}{r^2}\frac{\partial f}{\partial r}\left(r^2\frac{\partial f}{\partial r}\right) + \frac{1}{r^2\sin\theta}\frac{\partial}{\partial\theta}\left(\sin\theta\frac{\partial f}{\partial\theta}\right) + \frac{1}{r^2\sin^2\theta}\frac{\partial^2 f}{\partial\phi^2} = 0 \tag{1.2}$$

Solving this differential equation gives solutions: $f(r,\theta,\phi) = R(r)Y(\theta,\phi)$ with $Y_l^m(\theta,\phi) = e^{im\phi}P_l^m(\cos\theta)$, where the integer l denotes the order of the spherical harmonic, and m can range from -l to +l . P_l^m are the Legrendre polynomials, which can be seen in Ref.[5], and $R(r) = \frac{1}{r^{l+1}}$. Thus, there is one spherical harmonic of order 0 (monopole), 3 of order 1 (dipole), 5 of order 2 (quadrupole), 7 of order 3 (octupole), and so on. Since the spherical harmonics form an orthogonal basis, each multipole is orthogonal to every other one. This will restrict potential orbital interlap integrals when considering multiple electronic interactions between multipole sites.

When considering the electronic energy that arises from multipolar charge distributions, the corresponding solution for large R, ($R >> r_{int}$), where r_{int} represents the largest internal distance between charge elements in the distribution, from the electric potential is governed by:

$$V(R) = \sum_{l=0}^{\infty}\frac{C(l)}{R^{l+1}}\sum_{m=-l}^{l}(-1)^m Y_l^{-m}(\hat{R})Q_l^m \tag{1.3}$$

For which Q_l^m represents the multipole moments of the charge distribution. The potential and hence

the corresponding interaction energies fall off as $\frac{1}{R^{l+1}}$, meaning that the interaction energy for higher order multipole moments becomes progressively smaller with increasing l. This fact contributes to the empirical observation that higher-rank multipole order is less common than simple dipole order. However for certain materials, which generally contain $4f$ ions near both ends of the lanthanide series (Ce, Pr, as well as Tm, Yb) which have large orbital angular momentum numbers and small spin angular momentum numbers, these can have larger multipole interactions than dipole interactions.

Table 1.1 displays the lowest order multipoles from monopoles to octupoles, which are the relevant multipoles for $TmAg_2$ and $YbRu_2Ge_2$. Listed is the corresponding Stevens operator with its definition. Stevens operators are commonly used Hermitian operators which represent the Tesseral harmonics, which are just the real parts of the spherical harmonics. They are constructed via linear combinations of products of the standard angular momentum operators, J_z, J_x, J_y. When applied to wavefunctions, their eigenstates are the corresponding multipole angular functions, with the eigenvalues being the amount of multipole moment present.

One way in which the shapes of the multipoles can be approximated is by putting infinitesimally small charges with alternating signs infinitesimally close to each other, with the order/name of the multipole dictating how many charges there are. For instance a monopole is one positive charge at the origin, a dipole is one positive and one negative charge opposite each other which can be done along three different axes, quadrupoles can be thought of as four charges in the corner of a square arranged in a plane, an octupole as 8 alternating charges placed on the corners of a cube, and so on. From these simple pictures a pattern becomes clear: odd order multipolar charge distributions break inversion symmetry, and even ones don't. Thus for centrosymmetric crystal structures, which is the case for the two materials studied in this thesis, even electronic multipole moments that develop must be charge multipoles, and odd ones must be magnetic ones (magnetic vectors are pseudo-vectors which don't change sign under inversion). This is why they can be represented well by the Stevens operators, since because J_a is a magnetic pseudo-vector, any Stevens operator will conserve inversion symmetry. The charge multipoles will be represented by Stevens operators with even number products of J_a, and the magnetic multipoles (magnetic "charges" placed like the electric) by odd number products. Thus any quadrupoles mentioned in $TmAg_2$ and $YbRu_2Ge_2$ (both centrosymmetric) will manifestly be charge moments, and any octupoles will be magnetic moments. The final column in Table 1.1 lists the irreducible representation each multipole belongs to, which will be discussed in the next subsection.

1.3 Group theory

This section will just be a brief detour into this rich topic; for much more detail readers are referred to standard textbooks (see for example Ref [5].)

Group theory concerns the mathematics of sets of objects (elements) following certain rules,

Multipole	l	m	Steven's operator	Irrep in D_{4h}
Monopole	0	0	$O_0^0 = 1$	$A_{1g}(\Gamma_1)$
Dipole	1	1,-1	$O_1^1 = \frac{1}{2}(J_+ + J_-) = J_x$	$E_g(\Gamma_5)$
Dipole	1	0	$O_1^0 = J_z$	$A_{2g}(\Gamma_2)$
Dipole	1	1,-1	$O_1^{-1} = -\frac{i}{2}(J_+ - J_-) = J_y$	$E_g(\Gamma_5)$
Quadrupole	2	2,-2	$O_2^2 = J_x^2 - J_y^2$	$B_{1g}(\Gamma_3)$
Quadrupole	2	1,-1	$O_2^1 = P_{xz} = \frac{1}{2}(J_xJ_z + J_zJ_x)$	$E_g(\Gamma_5)$
Quadrupole	2	0	$O_2^0 = 3J_z^2 - J(J+1))$	$A_{1g}(\Gamma_1)$
Quadrupole	2	1,-1	$O_2^{-1} = P_{yz} = \frac{1}{2}(J_yJ_z + J_zJ_y)$	$E_g(\Gamma_5)$
Quadrupole	2	2,-2	$O_2^{-2} = 2P_{xy} = J_xJ_y + J_yJ_x$	$B_{2g}(\Gamma_4)$
Octupole	3	3,-3	$O_3^3 = \frac{1}{2}(J_+^3 + J_-^3)$	$E_g(\Gamma_5)$
Octupole	3	2,-2	$O_3^2 = \frac{1}{2}(O_2^2J_z + J_zO_2^2)$	$B_{2g}(\Gamma_4)$
Octupole	3	1,-1	$O_3^1 = \frac{1}{2}[(J_x)(F(J_z,J)) + (F(J_z,J))(J_x)]$	$E_g(\Gamma_5)$
Octupole	3	0	$O_3^0 = 5J_z^3 - (3J(J+1)-1)J_z$	$A_{2g}(\Gamma_2)$
Octupole	3	1,-1	$O_3^{-1} = \frac{1}{2}[(J_y)(F(J_z,J)) + (F(J_z,J))(J_y)]$	$E_g(\Gamma_5)$
Octupole	3	2,-2	$O_3^{-2} = \frac{1}{2}O_2^{-2}J_z + J_zO_2^{-2}$	$B_{1g}(\Gamma_3)$
Octupole	3	3,-3	$O_3^{-3} = -\frac{i}{2}(J_+^3 - J_-^3)$	$E_g(\Gamma_5)$

Table 1.1: **The multipoles up to the 3rd order, with their corresponding Steven's operators.** The Stevens operator notation will be used for the remainder of this thesis, as it connects the multipoles to their angular momentum operator representations. The linear combinations of the spherical harmonics that produce these Stevens operators also classify neatly into separate irreducible representations for D_{4h}, which will be discussed in Section 1.3. $F(J_z, J) = 5J_z^2 - J(J+1) - \frac{1}{2}$.

which are called groups. Because symmetry operations form groups, group theory is very relevant for studying crystal lattices. Even the symmetry operations of free space belong to a group with infinite elements (the Lie group SO3) and hence multipoles can be described in detail with group theory. Because all of the vast relevant properties and conclusions which arise from group theory can be deduced simply by the definition of the group, the formal mathematical definition is given now: A collection of elements A, B, C... are a group when these conditions are satisfied:

- The product of any two elements of the group is an element of the group. AB=C relations are valid for all members
- Associative law is valid (AB)C=A(BC)
- An identity element exists for which multiplication does not change any element. AE=EA=A
- Every element has an inverse in the group

For instance lets look at the symmetry operations in the point-group symmetry of D_{4h}, which is the point group surrounding the Yb^{3+} and Tm^{3+} ions in $YbRu_2Ge_2$ and $TmAg_2$ respectively. It is also the point group of the space group for both of these materials. As shown in Figure 1.1, the tetragonal crystal structure can be approximated by a rectangular prism, with lattice constants $a = b \neq c$. Symmetry operations will be the spatial operations which keep the crystal structure invariant, i.e. unchanged. Looking at the crystal structure, rotations of 90 degrees (C_4) and 180 degrees (C_2) around the c-axis will keep the structure invariant, for instance. All of the possible symmetry operations of D_{4h} are listed horizontally at the top of Table 1.2. These symmetry operations follow all 4 rules previously mentioned (notice the identity element E which does nothing), and thus form a group.

Groups are differentiated by the number of elements they have and the multiplication tables of those elements. For instance, for the symmetry operations of D_{4h}, applying a C_4 rotation after another C_4 rotation is equivalent to applying a C_2 rotation to the crystal, and a C_4 rotation after an inversion is equivalent to applying an S_4 improper rotation. Considering these sequential operations as multiplications, we can construct a multiplication table for these 16 elements (not included in this thesis).

Representations of the group are a set of numbers or matrices that map to these elements, following the multiplication table for the group. For instance we can map each element to the number 1, and this would satisfy the multiplication table. This is called the trivial representation, as it can map to any multiplication table. For D_{4h} this is called the A_{1g} representation, although in general it might have different names for different point groups it will always be listed first among the representations. The three other one-dimensional representations (A_{2g}, B_{1g}, and B_{2g}) have both 1 and -1 that map to the various symmetry operations, but still follow the multiplication table.

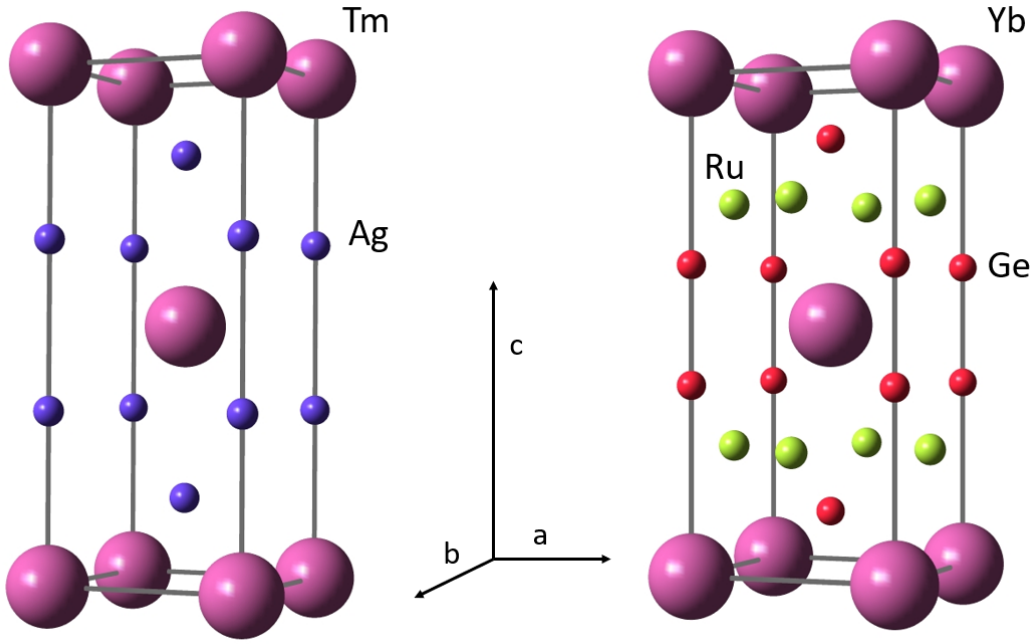

Figure 1.1: **The tetragonal crystal structures and unit cells of $TmAg_2$ on the left and $YbRu_2Ge_2$ on the right.** For $TmAg_2$ the lattice constants are: a=b=3.652Å, c=9.164Å and for $YbRu_2Ge_2$: a=b=4.8Å, c=9.2Å. The space group for these materials is I4/mmm. Both materials will be introduced in greater detail in Chapters 3 and 4.

D_{4h}	E	$2C_4(z)$	C_2	$2C_2'$	$2C_2''$	i	$2S_4$	σ_h	$2\sigma_v$	$2\sigma_d$
A_{1g}	1	1	1	1	1	1	1	1	1	1
A_{2g}	1	1	1	-1	-1	1	1	1	-1	-1
B_{1g}	1	-1	1	1	-1	1	-1	1	1	-1
B_{2g}	1	-1	1	-1	1	1	-1	1	-1	1
E_g	2	0	-2	0	0	2	0	-2	0	0
A_{1u}	1	1	1	1	1	-1	-1	- 1	-1	-1
A_{2u}	1	1	1	-1	-1	- 1	-1	-1	1	1
B_{1u}	1	-1	1	1	-1	-1	1	-1	-1	1
B_{2u}	1	-1	1	-1	1	-1	1	-1	1	-1
E_u	2	0	-2	0	0	-2	0	2	0	0

Table 1.2: **Character table for the point group symmetry D_{4h}.** The rows are all of the irreducible representations, which match the number of classes in the group. The columns are the classes of elements in D_{4h}. A class/column may have multiple elements in it (the second column $2C_4$ refers to the rotations by 90 degrees and -90 degrees,) and because they belong to the same class by definition they have the same character for all representations. The character rows are orthogonal when all 16 elements are considered. Note that the irreducible representations with a subscript u act with a negative sign under inversion, whereas those with g have a positive sign.

Because one can construct arbitrarily large matrices which satisfy the multiplication table (think of a representation where each element maps to an n-dimensional matrix with ones along the diagonal), assuming matrix multiplication serves as the multiplication operation, representations are defined by whether they are irreducible or not. For instance the mapping mentioned parenthetically looks like $A_{1g} \oplus A_{1g} \oplus A_{1g}$..... n times using direct sum notation, and so reduces to n copies of A_{1g} . That representation was a reducible one, and reduced to a series of irreducible representations. This reduction can be done for all representations except for the irreducible representations (irreps) listed in the rows of the character table. The character table lists the traces (characters) of the matrices (or just the numbers) that maps to each element in a given irreducible representation. These irreducible representations fundamentally determine the various symmetry modes that can break the point group symmetry via a continuous phase transition.

Physical objects and order parameters that when acted upon by each symmetry operation are multiplied by the corresponding number in the character table for a particular irreducible representation (or for n-dimensional irreps are a set of n objects which transform as if mulitplied by the corresponding matrix), are called partners of the representation, and colloquially belong to that representation and are often listed in the same row as the irrep in character tables. For instance, if we look at the $x^2 - y^2$ quadrupole, represented by the depiction of two positive charges placed along the x-axis with two negative charges along the y-axis, and we apply the C_4 symmetry operation, we multiply the corresponding function by -1. In fact if we applied all of the symmetry operations we would find that multiplying the function by the corresponding numbers (characters) in the B_{1g} row. Keep in mind this is more complicated for the n-dimensional irreps, for which we would need the actual matrices that map to the elements rather than just their traces to determine the partners. Nonetheless we can say that the $x^2 - y^2$ quadrupole is a B_{1g} quadrupole, and in general the multipoles are derived such that they can all be mapped as partners to their corresponding irreps. This process will be different for each point-group though, so Table 1.2 is only relevant to D_{4h}.

Here are some character table properties and definitions that are listed without justification, but they are important to understanding the theoretical and experimental results listed in Chapters 3-5. Proofs are given in any standard textbook on group theory (see for example Ref. [5].)

- Defintion: Classes are collections of elements within a group that satisfy $S * A * S^{-1} = B$ for all S, where S represents an element in the group, and A and B are elements that belong to the same class. In general for symmetry groups they correspond to collections of symmetry operations that are similar in nature (rotations of 90 degrees and -90 degrees for instance), and are often listed in the same column in character tables. This is because for a given irreducible representation its matrices which map to these elements will have the same character.

- The number of unique irreducible representations in a group is equal to the number of classes in a group.

- The sum of the squares of the dimensions of the the irreducible representations of a group is equal to the number of elements in the group. For instance in D_{4h}, $(1^2 + 1^2 + 1^2 + 1^2 + 2^2 + 1^2 + 1^2 + 1^2 + 1^2 + 2^2) = 16$
- The rows of a character table if imagined as vectors form a complete orthogonal basis for an n-dimensional vector space, where n is the number of irreps/classes in the group.
- The direct product of two representations in a group is the tensor product of the matrices of the representations, which forms another generally reproducible representation in that same group. One way this new representation can be found is by multiplying the corresponding character vectors for the representations in the direct product and then reducing this new product character vector into a linear combination of the irreducible representations. For instance if we multiply A_{2g} and B_{1g}, the resulting character vector is equivalent to B_{2g}'s character vector, and hence $A_{2g} \otimes B_{1g} = B_{2g}$.

1.3.1 Applications of group theory to $TmAg_2$ and $YbRu_2Ge_2$

We can apply the above properties to the crystal field spectrum for $TmAg_2$, for instance. The material will be discussed in detail in Chapter 5 of this thesis. Spin-orbit coupling results in a total angular momentum number of J=6 for the Tm^{3+} ion [3]. The J=6 spherical harmonics are in fact a irreducible representation of SO3, the group of symmetry operations in 3-D space. When they are placed inside a lower crystalline D_{4h} point-group symmetry, this representation is no longer irreducible, and will reduce to the direct sum of irreps of D_{4h} whose dimensions must add up to $2 * 6 + 1 = 13$. One can find the character vector for the 13x13 matrices which map to 16 symmetry operations acting upon the $m_j = -6$ to $+6$ states, and obtain that (following the notation in Ref. [6]:

$$D_6^{\pm} : 2\Gamma_1 \oplus \Gamma_2 \oplus 2\Gamma_3 \oplus 2\Gamma_4 \oplus 3\Gamma_5 \tag{1.4}$$

Thus the CEF spectrum of $TmAg_2$ is guaranteed to have 7 singlets (two Γ_1 (A_{1g}), one Γ_2 (A_{2g}), two Γ_3 (B_{1g}), two Γ_4 (B_{2g}) and 3 Γ_5 (E_g) doublets.

$YbRu_2Ge_2$ is a more complicated case. This material will be introduced in more detail in Chapter 3. Here spin-orbit coupling results in a total angular momentum number of J=7/2 for the Yb^{3+} ion [34, 4]. J=7/2 is actually an irrep of SU2, (which double covers SO3), but nonetheless

$$D_{\frac{7}{2}}^{\pm} : 2\Gamma_6 \oplus 2\Gamma_7 \tag{1.5}$$

Where Γ_6 and Γ_7 are spinor irreducible representations, which act differently than the normal irreps under rotations of 2π. These states are all doublets though, so we know that $YbRu_2Ge_2$'s CEF spectrum will have 4 doublets [6].

The definition/property relating to direct products (see previous section) is also particularly relevant to the formulation of free energies. In considering the terms allowed by symmetry for constructing a free energy for a system, the direct product irrep of the irreps of the terms must be the trivial representation, as only the trivial representation is unchanged by all of the symmetry operations, just as the free energy as well. In other words the free energy belongs to the trivial representation, so products of terms in it must also belong to the trivial representation. For instance if we were to consider in the free energy the product of a magnetic field H_z, which belongs to the irrep A_{2g}, and the strain $\varepsilon_{xx}-\varepsilon_{yy}$, which belongs to the irrep B_{1g}, and recalling that $A_{2g}\otimes B_{1g} = B_{2g}$ for D_{4h} it would have to couple to a term which belongs to the irrep B_{2g} (and also breaks time reversal symmetry), as $B_{2g}\otimes B_{2g} = A_{1g}$. Thus a potential multipolar coupling could be:

$$H_{oct} = -B_{oct}O_3^2 H_z(\varepsilon_{xx} - \varepsilon_{yy}) \tag{1.6}$$

as O_3^2 belongs to B_{2g} and breaks time-reversal symmetry. Here B_{oct} is just a coupling constant, the value of which is determined by microscopics of the system. We will return to the significance of this type of coupling later in the thesis.

It also is relevant for the Jahn-Teller theorem, whose second part states that: An electronically degenerate state is unstable to perturbations with irreducible representations contained in the direct product of the ground state with itself.

Looking at an E_g doublet for $TmAg_2$, which we will show in section 1.4.1 is the CEF ground state, any possible perturbations which may break the degeneracy will be given by:

$$E_g \otimes E_g = A_{1g} \oplus A_{2g} \oplus B_{1g} \oplus B_{2g} \tag{1.7}$$

Now, perturbations belonging to A_{1g} irreps won't break any symmetries, so we are left with only three possible symmetry channels for breaking degeneracy. The lowest order multipoles that belong to these symmetry channels are H_z (A_{2g}), O_2^2 (B_{1g}), and P_{xy} (B_{2g}), so we can expect for these terms and their conjugate fields to play roles as tuning parameters or order parameters in the low temperature physics of this system.

For $YbRu_2Ge_2$, again this is complicated by the fact that the ground state is a quasi-quartet. However if we make the assumption that the ground state can be viewed as a quartet consisting of Γ_6 and Γ_7 character ($\Gamma_6 \oplus \Gamma_7$), then:

$$(\Gamma_6 \oplus \Gamma_7) \otimes (\Gamma_6 \oplus \Gamma_7) = 2A_{1g} \oplus 2A_{2g} \oplus 2B_{1g} \oplus 2B_{2g} \oplus 4E_g \tag{1.8}$$

This can encompass all of the multipoles up to and including octupoles, if the quasi-quartet is approximated as consisting of only $|\pm\frac{1}{2}\rangle$ and $|\pm\frac{3}{2}\rangle$ states. Otherwise higher order multipoles which still belong to those irreps will be present.

1.4 Hamiltonians of local $4f$ orbitals

We now turn to the effective Hamiltonians that describe local $4f$ orbitals. A much more in-depth description of this topic can be found in Ref. [2].

The localized nature of the $4f$ electrons dictate that the relevant energy scales are in this order from largest to smallest:

- Electron-electron repulsion (electron-nuclear screening) to fill $4f$ orbitals (gives Hund's first 2 rules): $H_{el-el} \approx 1\text{eV}$
- Spin-orbit coupling determines J to be a good quantum number and gives Hund's 3rd rule, which dictates that $J = L + S$ if the $4f$ shell is more than half full, $J = L - S$ if not: $H_{SOC} \approx 0.4\text{eV}$
- Crystalline electric field (CEF) from the surrounding ligands : $H_{CEF} \approx 30\text{meV}$

We will assume for the rest of this section that the rare-earth ion takes the 3+ valence, i.e. there is no mixed valence taking place. This approximation is quite accurate for both $TmAg_2$ and $YbRu_2Ge_2$, as there is no experimental evidence of ions with the 2+ valence in these materials [3, 4, 35].

These energy scales manifest in the spectrum for $TmAg_2$ depicted in Figure 1.2. We will focus only on the $J = 6$ and $J = \frac{7}{2}$ multiplet for $TmAg_2$ and $YbRu_2Ge_2$ respectively. The lower energy scales are incorporated in this general Hamiltonian, where only the relevant terms for this work are included:

$$\hat{H}_{4f} = H_{CEF} + H_{ZEE} + H_{MM} + H_{QQ} + H_{ME} + E_{el} \tag{1.9}$$

where the various terms will be defined in the following sections. For now we are restricting ourselves to only considering multipolar interaction terms up to second-order (quadrupoles), although later we will show that we must consider higher-order multipoles for certain ground state manifolds. We are also explicitly neglecting any hybridization with the conduction electrons. For Tm^{3+} this is a safe assumption. For Yb^{3+} the Kondo effect can become relevant, but as we will show in Chapter 3 this seems to be relatively weak for $YbRu_2Ge_2$.

1.4.1 H_{CEF}

The arrangement of charged ions and metallic bonds surrounding the $4f$ electrons provides an electric potential which breaks the degeneracy of the $|m_J\rangle$ states. Assuming the ions are significantly far away relative to the extent of the $4f$ electronic multiplet, this electric potential can be represented by the interior multipole moments corresponding to the arrangement of the surrounding charges, i.e. the point charge model. Thus a Hamiltonian can be written down with Stevens operators to represent

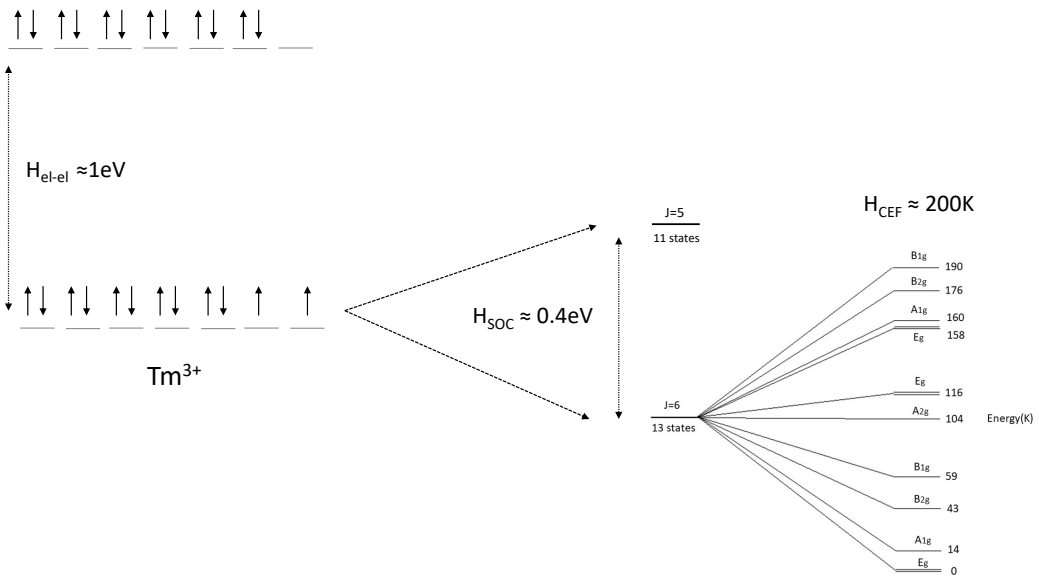

Figure 1.2: **A visual depiction of the relevant energy scales for the 4*f* electrons in the $TmAg_2$.** The CEF state energies, which are proposed from previous neutron diffraction experiments [3], are not to scale and have been expanded for clarity. This work will only focus on energy scales at and below H_{CEF}. $YbRu_2Ge_2$ would have a similar diagram but with different multiplicities (different Js) and a different CEF spectrum.

these multipoles. Because the point-group symmetry of the $4f$ ion constrains the arrangement of the surrounding charges, there are relatively few free parameters compared to the number of nearest neighbors once the point group symmetry is given. In the case of a tetragonal point group symmetry, the form of H_{CEF} is given by:

$$\hat{H}_{CEF}^{Tet} = B_2^0 O_2^0 + B_4^0 O_4^0 + B_4^4 O_4^4 + B_6^0 O_6^0 + B_6^4 O_6^4 \tag{1.10}$$

where the B_l^m terms are coefficients, and O_l^m are Stevens operators which in this case represent quadrupoles, hexadecapoles and higher order multipoles. Notice that time-reversal symmetry prevents any odd-ordered multipoles from appearing, and the other spatial symmetries rule out any other terms. The B_l^m coefficients are not known *a priori*, and differ for every environment with different surrounding atoms. Nonetheless H_{CEF} splits the $4f$ electronic multiplet into a spectrum of states where the degeneracies for each subset is known. For instance, for J=6 $4f$ ions (Tm), in D_{4h} the 13 states are split into 3 doublets and 7 singlets. This is known by group theory, as was mentioned in section 1.3. However the energies of those manifolds cannot be determined without knowing the details of the surrounding atoms which determines the B_l^m coefficients. In the case of $TmAg_2$, H_{CEF} creates a spectrum displayed in Figure 1.2 [3]. Notably the ground state is a doublet which can harbor quadrupolar degrees of freedom. For $YbRu_2Ge_2$, which has a spectrum displayed in Figure 3.6, it has a quasi-quartet ground state which can be approximated as a J=3/2 quartet, which can support up to octupolar degrees of freedom [4] . Further details of the CEF spectrum for each material will be discussed in Chapters 3 and 4.

1.4.2 H_{ZEE}

H_{ZEE} is the common Zeeman term that arises from applying a magnetic field.

$$H_{ZEE} = -g_J \mu_B \vec{J} \cdot \vec{H} \tag{1.11}$$

Where g_J is the Lande factor for the magnetic ion, and μ_B is a Bohr magneton. The Lande factor indicates the effective magnetic susceptibility of an electronic multiplet with a quantum number J that was formed from having a certain L and S. The Lande factor is:

$$g_J = \frac{3J(J+1) - L(L+1) + S(S+1)}{2J(J+1)} \tag{1.12}$$

It will be most relevant for this work when a magnetic field is applied along the c-axis. At low temperatures the effective magnetic susceptibility will be determined by the m_j quantum numbers of the ground state. In the case of $TmAg_2$ its doublet is constructed from $|\pm 1\rangle$, $|\pm 3\rangle$, and $|\pm 5\rangle$ states [3]. For $YbRu_2Ge_2$, it is proposed to be mostly $|\pm \frac{1}{2}\rangle$ and $|\pm \frac{3}{2}\rangle$ states that make up its quasi-quartet [4].

1.4.3 H_{MM}

H_{MM} is the magnetic interaction energy. Because of the tetragonal symmetry there is an allowed symmetric magnetic interaction and a separate anisotropic interaction:

$$H^1_{MM} = -g_j^2\mu_B^2 n_1 \langle J\rangle J \tag{1.13}$$

$$H^2_{MM} = -g_j^2\mu_B^2 n_2 (2\langle J_z\rangle J_z - \langle J_y\rangle J_y - \langle J_x\rangle J_x) \tag{1.14}$$

These terms are mean-field approximations of interactions of $4f$ magnetic moments with the internal magnetic field. For $4f$ intermetallics, this mean field interaction is mostly provided by the Ruderman–Kittel–Kasuya–Yosida (RKKY) interaction. This interaction arises from second-order perturbation theory with exchange interactions between local $4f$ electrons and conduction electrons, and it manifests as an effective long range coupling between the spins of $4f$ sites [10]. These terms can result in magnetic order at finite temperature, but other higher rank multipolar interactions can be at or above these energy scales. Materials that contain $4f$ ions near both ends of the lanthanide series (Ce, Pr, as well as Tm, Yb), which have large orbital angular momentum numbers and small spin angular momentum numbers, can have larger multipole interactions than dipole interactions, as is the case for the $TmAg_2$ and $YbRu_2Ge_2$.

1.4.4 E_{el}

E_{el} represents the elastic energy of the lattice, although we include only the relevant terms for applying in-plane stresses:

$$E_{el} = \frac{C_\alpha}{2}\varepsilon^2_{A_{1g}} + \frac{C_\gamma}{2}\varepsilon^2_{B_{1g}} + \frac{C_\epsilon}{2}\varepsilon^2_{B_{2g}} \tag{1.15}$$

Where C_i are the unrenormalized elastic constants of the material for each symmetry channel. These terms describe the energy cost to distorting the lattice for the different symmetry channels, which are labeled in Table 1.3.

1.5 Cooperative Jahn-Teller ferroquadrupolar transitions from H_{QQ} and H_{ME}

H_{QQ} is the quadrupolar interaction term. It incorporates the five different allowed quadrupoles and their mean field interactions with the internal quadrupolar fields. Again these mean field interactions are mediated through the conduction electrons via the RKKY interaction, which also provides a long-range coupling between quadrupoles [10].

$$H_{QQ} = -K_\alpha\langle O^0_2\rangle O^0_2 - K_\gamma\langle O^2_2\rangle O^2_2 - K_\alpha\langle P_{xy}\rangle P_{xy} - K_\epsilon(\langle P_{xz}\rangle P_{xz} - \langle P_{yz}\rangle P_{yz}) \tag{1.16}$$

Irrep in D_{4h}	Strain	Conjugate quadrupole
$A_{1g,1}$	$\frac{1}{2}(\varepsilon_{xx}+\varepsilon_{yy})$	O_2^0
$A_{1g,2}$	ε_{zz}	O_2^0
B_{1g}	$\frac{1}{2}(\varepsilon_{xx}-\varepsilon_{yy})$	O_2^2
B_{2g}	ε_{xy}	P_{xy}
E_g	ε_{xz}, ε_{yz}	P_{xz},P_{yz}

Table 1.3: **The irreducible representations of strain for D_{4h} and the conjugate quadrupoles.** For D_{4h} two distinct strains span the A_{1g} representation, we have chosen a convenient basis which differentiates in-plane from out-of-plane strain.

H_{ME} is the magnetoelastic term, which includes the bilinear coupling between the quadrupoles and their conjugate strains.

$$H_{ME} = -(B_{\alpha 1}\varepsilon_{\alpha 1} + B_{\alpha 2}\varepsilon_{\alpha 2})O_2^0 - B_\gamma(\varepsilon_{xx}-\varepsilon_{yy})O_2^2 - B_\delta\varepsilon_{xy}P_{xy} - B_\epsilon(\varepsilon_{xz}P_{xz}-\varepsilon_{yz}P_{yz}) \quad (1.17)$$

K_n are the mean-field coupling constants, and B_n are the magnetoelastic coupling constants. As mentioned before, the bilinear couplings in H_{ME} stem from the fact that quadrupoles and strain are both symmetric second-rank tensors, and hence decompose into the same irreducible representations. All of the couplings here involve a quadrupole coupled to the same irrep strain. Notice that for tetragonal systems O_2^0 has a nonzero value by definition, so while that quadrupole-quadrupole coupling term isn't forbidden it doesn't factor into any symmetry breaking phase transitions.

In considering $TmAg_2$ and $YbRu_2Ge_2$ we will restrict ourselves to looking at the B_{1g} quadrupole O_2^2, and the B_{2g} quadrupole P_{xy}, (and associated strains), as the relevant order parameters are B_{1g} for the ferroquadrupolar phase transitions at 5K and 10.2K respectively [3, 4], and we only apply in-plane stresses (although this will induce strains in the z-direction which will appear in the magnetoelastic coupling of O_2^0, this will not induce out of plane shear strains.)

From these two terms and the elastic energy we can get a sense of the quadrupolar behavior in these systems. We can write down the corresponding generic free energy for a material with a magnetoelastic coupling in a given symmetry channel. We can solve for the value of the strain that minimizes the free energy:

$$F = -BQ\varepsilon + \frac{C}{2}\varepsilon^2 \tag{1.18}$$

$$\frac{\partial F}{\partial \varepsilon} = -BQ + C\varepsilon = 0 \tag{1.19}$$

$$\varepsilon = \frac{B}{C}Q \tag{1.20}$$

At least perturbatively the strain will adopt a value proportional to the order parameter. We can substitute this back into H_{ME} and combine this with H_{QQ} to get the total effective mean field quadrupolar interaction terms:

$$H_{QQ}^{eff} = \sum_{\beta} -\left(\frac{B_\beta^2}{C_\beta} + K_\beta\right)\langle Q_\beta\rangle Q_\beta \tag{1.21}$$

where the sum is over the different types of quadrupoles. Thus the effective mean field coupling constant is actually $\frac{B^2}{C} + K$ for each symmetry channel, with the strength of the strain mediated part of the interaction represented by $\frac{B^2}{C}$ and the part that is mediated by the conduction electrons represented by K. If this coefficient is large and negative it can cause a finite temperature ferro-quadrupolar phase transition. If we assume the ground state of the $4f$ electrons is a non-magnetic doublet that has non-zero quadrupolar matrix elements (like in $TmAg_2$'s case), and we assume only one quadrupole is active, then we can diagonalize this Hamiltonian and find the thermal expectation value of the order parameter to obtain the usual self-consistent equation familiar from mean-field treatments of S=1/2 Ising models:

$$\langle Q\rangle = Q_o^2\left(\frac{B^2}{C} + K\right)\tanh\left(\frac{\langle Q\rangle}{T}\right) \tag{1.22}$$

Where K and $\frac{B^2}{C}$ are in Kelvin so $k_B = 1$, and Q, B, C, and K all belong to the same irreducible representation. Q_o is the value of the quadrupolar matrix element between the two states of the ground state. A phase transition occurs right as $\langle Q\rangle$ becomes non-zero, so this transition occurs at :

$$T_Q = Q_o^2\left(\frac{B^2}{C} + K\right) \tag{1.23}$$

We can also find the corresponding quadrupolar fluctuations for this system, which through the fluctuation-dissipation theorem will be represented by the quadrupole-strain susceptibility:

$$\left.\frac{d\langle Q\rangle}{d\varepsilon}\right|_{\varepsilon\to 0} = \frac{BQ_o^2}{T - KQ_o^2} \tag{1.24}$$

Although these equations only hold when the ground state is an isolated doublet (i.e. the Ising model), we will see in section 1.6.3 that for $TmAg_2$ that the quadrupole-strain susceptibilities should

map on to this model exactly at low temperatures. With some further approximations described in section 1.6.5, this may be the case as well for $YbRu_2Ge_2$.

1.6 The Ising Model and its application to ferroquadrupole order

The low temperature behavior of $TmAg_2$ and $YbRu_2Ge_2$ both map on to the Ising model. We therefore take a brief detour to describe some basic aspects of the Ising model, including the effects of tranverse fields. With that understanding in place, I demonstrate how each of thse materials maps on to the Ising model, and futhermore how strain and magnetic field map onto transverse fields for $TmAg_2$. These results will provide an important context for investigating these materials' phase diagrams in the proximity of where their ferroquadrupolar phase transitions have been completely suppressed to 0K.

1.6.1 The Ising Model

For a more detailed look at Ising models, the reader is referred to Ref [9]. The Ising model is a classic statistical mechanics model, and it has been used to describe a variety of systems, from magnetic spins in a lattice to neurons in the brain. The simplest variant is the spin 1/2 Ising model. It considers a lattice of interacting spins with two states, up and down. Each spin interacts with its neighbors with an interaction term, and the spins align with an energy gain/cost of J depending on its sign. An external magnetic field can also be applied, which will make it energetically favorable for spins to choose that direction. This can be written with a Hamiltonian:

$$H^{tot} = J\sum_i \sum_{j\neq i}^{nn} S_i^z S_j^z + g\sum_i H_z S_i^z \tag{1.25}$$

Where S_i^z is the z-component of the spin on the ith site which can either be $\hbar/2$ or $-\hbar/2$, H_z is the applied magnetic field, and g is the field coupling constant. This model has been solved for one, two, and three dimensions, with different critical scaling behavior for each case. In fact for one dimension there is only a phase transition at 0K, whereas a finite temperature phase transition for two and three dimensions. Above three dimensions the solution to this model is identical to its mean-field approximation. The corresponding mean-field model is:

$$H^{mf} = nJ\sum_i \langle M\rangle S_i^z + gH_z S_i^z \tag{1.26}$$

where $\langle M\rangle$ is the thermal expectation value of the spin, and represents the effective "internal field" each site interacts with and approximates the nearest neighbor interactions. More generally

as we consider systems with increasing dimensionality the number of nearest neighbor interactions increases, and so $\langle M \rangle$ becomes a better approximation. Specifically the Ginzburg criterion, which states that the mean field approximation is correct when fluctuations are smaller than the order parameter in the critical regime, is satisfied for the Ising model at dimensions at and above the upper critical dimension of 4.

The mean-field Ising model can be solved in the standard way to obtain a self-consistent equation for the internal field $\langle M \rangle$ (assuming $g = 1$):

$$\langle M \rangle = \frac{1}{2} \tanh \left(\frac{nJ\langle M \rangle + H_z}{2k_B T} \right) \tag{1.27}$$

Which gives a finite temperature phase transition at $T_c = \frac{nJ}{4k_B}$, and a Curie-Weiss susceptibility of

$$\left. \frac{d\langle M \rangle}{dH} \right|_{H \to 0} = \frac{1}{4(k_B T - nJ/4)} \tag{1.28}$$

At temperatures close to and below T_c, M (when $H_z = 0$) can be expanded as:

$$\langle M \rangle \propto \left(1 - \frac{T}{T_c} \right)^{\frac{1}{2}} \tag{1.29}$$

We will shortly show how ferroquadrupole order among the local $4f$ orbitals in $TmAg_2$ and $YbRu_2Ge_2$ map on to the Ising model, but we remark here that when applied to these systems long range strain interactions reduce the upper critical dimension to 2 [7], such that mean-field behavior is in fact anticipated for such systems. We will discuss in section 1.6.3 that the ground state manifolds for these materials can be analyzed through considering them as three-dimensional pseudo-spin spaces, but that the interactions for this materials are highly anisotropic such that the Ising model is applicable rather than the Heisenberg model, which describes pseudo-spins with isotropic interactions.

1.6.2 Transverse field Ising model

The transverse field Ising model adds a term in the Hamiltonian which is the coupling of an applied field with the x component of the spin, S_x. Since the field is oriented transverse to the ordering component S_z, this is referred to as a transverse field. The S_x operator does not commute with S_z, but rather follows the canonical Pauli commutation relation: $[S_x, S_z] = iS_y$. Thus this term will induce quantum fluctuations which will suppress the phase transition.

$$H_{tr}^{mf} = nJ \sum_i \langle M^z \rangle S_i^z + \sum_i \left(g_z H_z S_i^z + g_x H_x S_i^x \right) \tag{1.30}$$

This model can be solved at a mean-field level by using the matrix formulism for these operators (g_z and g_x are assumed to be 1). In the spin 1/2 basis (assuming $\hbar = 1$):

$$S_z = \frac{1}{2}\begin{bmatrix} 1 & 0 \\ 0 & -1 \end{bmatrix} \tag{1.31}$$

$$S_x = \frac{1}{2}\begin{bmatrix} 0 & 1 \\ 1 & 0 \end{bmatrix} \tag{1.32}$$

The total Hamiltonian can be diagonalized to find the eigenenergies and corresponding eigenstates. Similarly as before $\langle M^z \rangle$ is obtained via this self-consistent equation:

$$\langle M^z \rangle = \frac{nJ\langle M^z \rangle + H_z}{2\sqrt{(nJ\langle M^z \rangle + H_z)^2 + H_x^2}} \tanh\left(\frac{\sqrt{(nJ\langle M^z \rangle + H_z)^2 + H_x^2}}{2k_B T}\right) \tag{1.33}$$

With a critical temperature that is now a function of H_x following:

$$k_B T_Q = \frac{H_x}{2\tanh^{-1}\left(\frac{2H_x}{nJ}\right)} \tag{1.34}$$

Because $\tanh^{-1}(x) \approx x + x^3/3+....$, an increasing H_x will result in supressing T_Q, eventually to 0K at a critical field of

$$H_c = \frac{nJ}{2} \tag{1.35}$$

If a material's phase diagram aligns with this calculated phase boundary, (plotted in Figure 1.3), that provides evidence that the system is governed by a mean-field transverse field Ising model. In Chapter 5 both elastocaloric and heat capacity measurements will show $TmAg_2$'s phase boundary is consistent with this model.

The susceptibility for this model is also clearly affected by the inclusion of the transverse field term, and is:

$$\left.\frac{d\langle M^z \rangle}{dH_z}\right|_{H_z \to 0} = \frac{\frac{1}{2}\tanh\left(\frac{H_x}{2k_B T}\right)}{H_x - \frac{nJ}{4}\left(\tanh\left(\frac{H_x}{2k_B T}\right)\right)} \tag{1.36}$$

As seen in Figure 1.4, the susceptibility lowers in magnitude and diverges towards lower temperatures as H_x increases.

More generally, the model is not only relevant to this work in the sense that it maps approximately to $TmAg_2$ and $YbRu_2Ge_2$, but also because it guarantees a second order phase transition that is smoothly suppressed to 0K. This will be a quantum critical point for the system, and can potentially

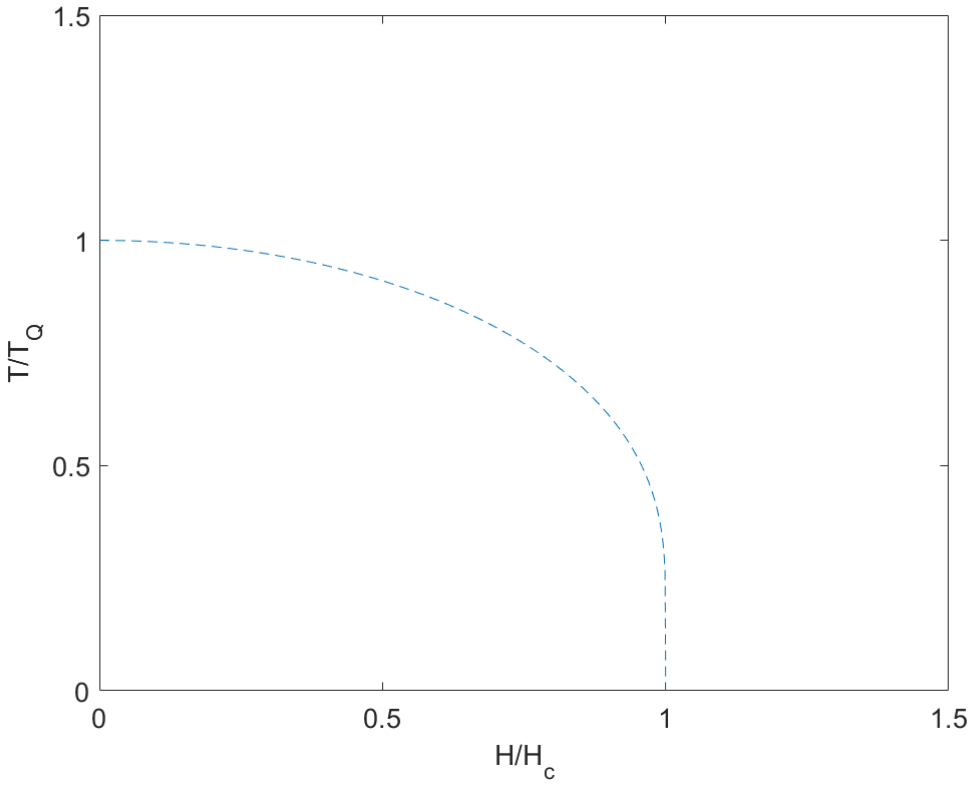

Figure 1.3: **The phase boundary for the mean-field transverse field S=1/2 Ising model.** Notice in the proximity of H_c that the phase boundary is very steep, making this a difficult phase diagram to be experimentally investigated.

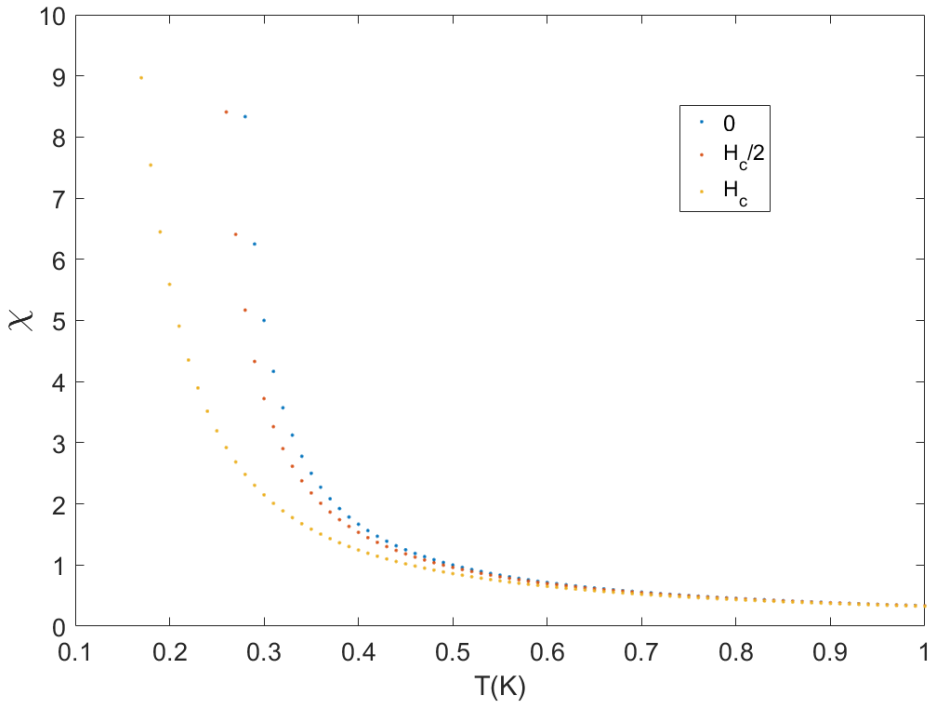

Figure 1.4: **The order parameter susceptibility vs. temperature for different values of tranvserse field H_x.** Here $nJ = 1$, so $T_Q(H_x = 0) = 0.25$, and $H_c = 0.5$.

offer exciting physics.

1.6.3 Mapping of the low energy effective Hamiltonian of $TmAg_2$ to the Transverse field Ising model

In this section we will consider an effective Hamiltonian in which both magnetic field and strain are applied to $TmAg_2$. This is relevant to the elastocaloric measurements in Chapter 5, which apply perturbative strains of both A_{1g} and B_{2g} symmetry to a sample in the presence of a finite magnetic field oriented along the c-axis.

The E_g (Γ_5) doublet ground state of $TmAg_2$ consists of states $|s_\pm\rangle = a|\pm 1\rangle + b|\mp 3\rangle + c|\pm 5\rangle$, where a=-0.664, b=0.135, c=0.735, as reported in Ref. [3]. The nearest excited state is an A_{2g} singlet consisting of states $0.4392|-4\rangle - 0.784|0\rangle + 0.4392|4\rangle$ at 14 K. It will have no matrix elements with either of the doublet states for any of the relevant magnetic dipole or quadrupole operators. In fact the only excited states with non-zero matrix elements will be other E_g doublets, and in the case of $TmAg_2$'s CEF spectrum the nearest excited doublet is at ∼100K. Thus considering just the reduced Hilbert space of the ground state doublet is justified at low temperatures.

If we consider the multipoles previously mentioned in the group theory section which map to A_{2g}, B_{1g}, and B_{2g}, which are S_z, O_2^2, and P_{xy} respectively, they have matrix elements in this doublet basis that looking at S_z for example, can be found as:

$$S_z^M(i,j) = \langle s_i|S_z|s_j\rangle \tag{1.37}$$

Where $|s_1\rangle = |s_+\rangle$ and $s_2 = |s_-\rangle$ Because in the m_J basis S_z only connects states which have components with the same m_J quantum number, S_z^M can be written as:

$$S_z = \begin{bmatrix} A & 0 \\ 0 & -A \end{bmatrix} \tag{1.38}$$

Where $A = 5c^2 - 3b^2 + 1a^2 \approx 3.09$.

The matrix for the operator O_2^2 in the doublet ground state can be found similarly, but because $O_2^2 = \frac{1}{2}(J_+^2 + J_-^2)$ it will connect states with m_J components that differ by ±2. Thus it will have matrix elements between the two doublet states and be in the form:

$$O_2^2 = \begin{bmatrix} 0 & Q \\ Q & 0 \end{bmatrix} \tag{1.39}$$

Where $Q = 12\sqrt{10}ab + 2\sqrt{165}bc + 21a^2 \approx 15.2$

Finally P_{xy} acts similarly to O_2^2 but will have imaginary matrix elements as it is defined as

$P_{xy} = \frac{i}{4}(J_+^2 - J_-^2)$

$$P_{xy} = \begin{bmatrix} 0 & iQ_{xy} \\ -iQ_{xy} & 0 \end{bmatrix} \tag{1.40}$$

Where $Q_{xy} = -6\sqrt{10}ab + \sqrt{165}bc + 10.5a^2 \approx 4.2$;

These three operators map to the canonical Pauli spin matrices when they are rescaled such that $A = Q = Q_{xy}$. These scaled operators will satisfy the Pauli commutation relations, and hence form a set of transverse operators for this Ising doublet.

1.6.4 Applying the Transverse Field Ising model: Strain derivatives of T_Q

We can apply the results of the transverse field Ising model to obtain derivatives of the ferro-quadrupolar phase transition temperature for $TmAg_2$ with respect to both strains. These quantities are relevant as they can be inferred by the elastocaloric method (this will be shown in Chapter 2), and so we include the calculations for that here.

Consider first the $4f$ Hamiltonian for $TmAg_2$ where both transverse fields H_z and ε_{xy} have been applied:

$$\hat{H} = g_j\mu_B H_z S_z - B_g(\varepsilon_{xx} - \varepsilon_{yy})O_2^2 - K_g\langle O_2^2\rangle O_2^2 - B_{xy}\varepsilon_{xy}P_{xy} - K_{xy}\langle P_{xy}\rangle P_{xy} \tag{1.41}$$

or

$$\hat{H} = A_o S_z + B_o O_2^2 + C_o P_{xy} \tag{1.42}$$

Where A_o, B_o, and C_o are defined by comparing to Eq. 1.41. Restricted to the ground state Hilbert space, this Hamiltonian takes the matrix form:

$$\hat{H} = \begin{bmatrix} A_o & B_oQ + C_oQ_{xy}i \\ B_oQ - C_oQ_{xy}i & -A_o \end{bmatrix} = \begin{bmatrix} A & B + Ci \\ B - Ci & -A \end{bmatrix} \tag{1.43}$$

Where A, B, and C have absorbed the magnitude of matrix elements of the quadrupole operators O_2^2 and P_{xy}, i.e. $A = A_o$, $B = B_oQ$, and $C = C_oQ_{xy}$. Diagonalizing this matrix gives energy eigenvalues:

$$E_\pm = \pm\sqrt{A^2 + B^2 + C^2} \tag{1.44}$$

And an associated gap:

$$\Delta = 2\sqrt{A^2 + B^2 + C^2} \tag{1.45}$$

Because H_z, $\varepsilon_{B_{1g}}$, and $\varepsilon_{B_{2g}}$ form a set of transverse fields for the ground state doublet of $TmAg_2$, the energy gaps associated with each field add in quadrature to form the total energy gap between the two mean-field eigenstates. It is analogous to a 3 dimensional coordinate pseudo-spin space where the three corresponding transverse operators form the orthogonal axes. Normalized properly the total energy gap is just the magnitude of the vector in this space. Applying a transverse field in the ordered state reduces the magnitude of the order parameter and actually corresponds to a rotation in the pseudo-spin space which leaves the total gap unchanged.

The self-consistent equation for either quadrupole is identical to the magnetic self-consistent equation obtained in the transverse field Ising model except now the gap is a function of three mutually tranverse effective fields instead of two.

$$\langle O_Q^i \rangle = \frac{2Q^i B}{\Delta} \tanh\left(\frac{\Delta}{2k_B T}\right) \tag{1.46}$$

where $\langle O_Q^i \rangle$ is the order parameter for either the B_{1g} or B_{2g} quadrupole, and Q^i represents the corresponding quadrupolar matrix element.

Focusing on the order parameter, T_Q occurs when $\langle O_2^2 \rangle$ first becomes 0 with increasing longitudinal field, so

$$k_B T_Q = \frac{\sqrt{A^2 + C^2}}{\tanh^{-1}\left(\frac{\sqrt{A^2+C^2}}{Q^2 G_g}\right)} \tag{1.47}$$

where $G_g = K_g + \frac{B_g^2}{C_g}$. This equation indicates the magnitude of the critical effective transverse field $F_c = Q^2 G_g = \sqrt{A^2 + C^2}$

To find $\frac{d^2 T_Q}{d\varepsilon_{xy}^2}|_{\varepsilon_{xy}=0}$ (the first derivative is 0 by symmetry), we can expand both the numerator and denominator for small C^2 and keep only the first terms:

$$k_B T_Q = \frac{A + C^2/(2A)}{\tanh^{-1}\left(\frac{A}{F_c}\right) + \frac{C^2}{2A(F_c - A^2/(F_c))}} \tag{1.48}$$

Thus at the limit of $C \to 0$, i.e. $\varepsilon_{B_{2g}} \to 0$, the critical effective transverse field is just the critical magnetic field $F_c = A_c$, and

$$\left.\frac{d^2 T_Q}{d\varepsilon_{B_{2g}}^2}\right|_{\varepsilon_{B_{2g}} \to 0} = B_{xy}^2 Q_{xy}^2 \frac{\tanh^{-1}(\frac{A}{A_c}) - \frac{A}{A_c - A^2/A_c}}{2A(\tanh^{-1}(\frac{A}{A_c}))^2} \tag{1.49}$$

This is plotted in Figure 1.5.

Notice that A_{1g} strain ($\varepsilon_{A_{1g}} = \frac{1}{2}(\varepsilon_{xx} + \varepsilon_{yy})$), has not been included in this Hamiltonian. Nonetheless it does appear when applying uniaxial stress as is done in the elastocaloric measurements, and hence is relevant. Specifically it will also tune the phase transition, even though it doesn't function as a transverse field.

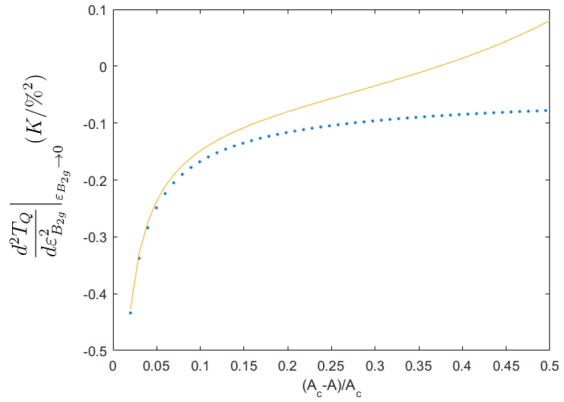

Figure 1.5: **Calculated B_{2g} strain derivative of T_Q plotted as a function of the reduced magnetic field (blue dots).** A power law fit in the proximity of A_c is shown as a yellow line. The scale of the y-axis is arbitrary, although the sign is fixed to be negative by the nature of a transverse field.

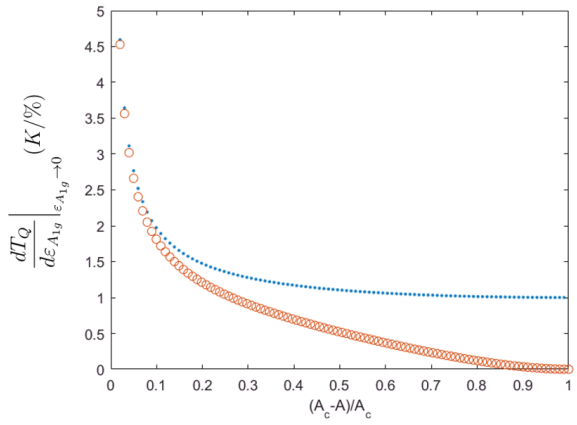

Figure 1.6: **Calculated A_{1g} strain derivative of T_Q plotted as a function of the reduced magnetic field (blue dots).** A power law fit in the proximity of A_c is shown as a red circles. The scale of the y-axis is arbitrary, and the sign has been arbitrarily chosen to match empirical data.

T_Q will be shown empirically to vary linearly with respect to A_{1g} strain in Chapter 5. Looking at Eq. 1.47 the only way that the right hand side can provide a non-zero $\frac{dT_Q}{d\varepsilon_{A_{1g}}}|_{\varepsilon_{A_{1g}}\to 0}$ is if G_g is a function of $\varepsilon_{A_{1g}}$. If we assume G_g=G_g^0+ $B_2^0\varepsilon_{A_{1g}}$, then expanding as we did before gives:

$$\left.\frac{dT_Q}{d\varepsilon_{A_{1g}}}\right|_{\varepsilon_{A_{1g}}\to 0} = -\frac{A^2}{A^2-A_c^2}\frac{B_2^0 Q^2}{\left(\tanh^{-1}(\frac{A}{A_c})\right)^2} \tag{1.50}$$

which is plotted in Figure 1.6.

Note neither of these derivatives are particularly well described by a power law fit. As the critical field is approached the strain derivatives for both symmetry channels are expected to diverge which is matched empirically by the experiments in Chapter 5.

1.6.5 Ising model applied to $YbRu_2Ge_2$

$YbRu_2Ge_2$'s ground state is proposed to be a quasi-quartet with a gap $\Delta_0 < 10K$ [4], shown in Figure 3.6, so it cannot map precisely to the spin 1/2 transverse field Ising model. Nonetheless if we consider the quasi-quartet as consisting of a doublet (basis states $|\frac{3}{2}\rangle$ and $|-\frac{1}{2}\rangle$), and its time reversed partner, we can gain some insight into the expected magnetic field phase diagram and the quadrupole-strain susceptibility.

Looking at the three relevant quadrupole operators, which correspond to the axis of the quadrupole oriented along [0 0 1] (z^2 symmetry), along [1 0 0] or [0 1 0] (x^2-y^2 symmetry), and along [1 1 0] or [1 -1 0] (xy symmetry), these are given respectively by the familiar Stevens operators:

$$O_2^0 = 3J_z^2 - J(J+1) \tag{1.51}$$

$$O_2^2 = J_x^2 - J_y^2 = \frac{1}{2}(J_+^2 + J_-^2) \tag{1.52}$$

$$P_{xy} = \frac{1}{2}(J_xJ_y + J_yJ_x) = \frac{-i}{4}(J_+^2 - J_-^2) \tag{1.53}$$

In the restricted Hilbert space corresponding to the quasi-quartet CEF groundstate of $YbRu_2Ge_2$, and making the approximation the ground state Γ_6 doublet solely consists of $|\pm\frac{1}{2}\rangle$ and the excited Γ_7 doublet $|\pm\frac{3}{2}\rangle$, these operators have the following matrix elements, where for convenience the basis of states is represented in the order (3/2, -1/2, -3/2, 1/2)

$$O_2^0 = \begin{bmatrix} -15 & 0 & 0 & 0 \\ 0 & -9 & 0 & 0 \\ 0 & 0 & -15 & 0 \\ 0 & 0 & 0 & -9 \end{bmatrix}$$

$$O_2^2 = \begin{bmatrix} 0 & 2\sqrt{15} & 0 & 0 \\ 2\sqrt{15} & 0 & 0 & 0 \\ 0 & 0 & 0 & 2\sqrt{15} \\ 0 & 0 & 2\sqrt{15} & 0 \end{bmatrix}$$

$$P_{xy} = \begin{bmatrix} 0 & -i\sqrt{15} & 0 & 0 \\ i\sqrt{15} & 0 & 0 & 0 \\ 0 & 0 & 0 & i\sqrt{15} \\ 0 & 0 & -i\sqrt{15} & 0 \end{bmatrix}$$

Of course:

$$H_z = \begin{bmatrix} 3/2 & 0 & 0 & 0 \\ 0 & -1/2 & 0 & 0 \\ 0 & 0 & -3/2 & 0 \\ 0 & 0 & 0 & 1/2 \end{bmatrix}$$

Noticing the correspondence to the Pauli spin matrices, we introduce for completeness a third, octupole, operator, that will also have finite matrix elements in this basis: $O_3^{-2} = \frac{-i}{4}(J_z(J_+^2 - J_-^2) + (J_+^2 - J_-^2)J_z)$

$$O_3^{-2} = \begin{bmatrix} 0 & -i\sqrt{15} & 0 & 0 \\ i\sqrt{15} & 0 & 0 & 0 \\ 0 & 0 & 0 & -i\sqrt{15} \\ 0 & 0 & i\sqrt{15} & 0 \end{bmatrix}$$

Inspection of these expressions reveals they can be written as tensor products of the canonical Pauli matrices and the identity, I:

$$O_0^2 = I \otimes (-3\sigma_z - 12I) \tag{1.54}$$

$$O_2^2 = I \otimes (2\sqrt{15}\sigma_x) \tag{1.55}$$

$$P_{xy} = \sigma_z \otimes (\sqrt{15}\sigma_y) \tag{1.56}$$

$$H_z = \sigma_z \otimes (2\sigma_z + 1/2I) \tag{1.57}$$

$$O_3^{-2} = I \otimes (\sqrt{15}\sigma_y) \tag{1.58}$$

With reference to the tensor product formula:

$$[I \otimes A, I \otimes B] = I \otimes [A, B] \tag{1.59}$$

and noting that constants don't affect commutation relations, the three operators O_2^0, O_2^2, and O_3^{-2} obey the canonical commutation relations. These three operators will then serve as the effective spin operators in the three spatial dimensions of the pseudo-spin space. The quartet is split (by roughly $\Delta_0 = 10K$ [4]) due to the tetragonal point symmetry of the CEF, yielding a finite σ_z (i.e a finite O_2^0 quadrupole moment) above T_Q. Thus the B_{1g} quadrupole susceptibility for $YbRu_2Ge_2$ in the absence of magnetic field will be exactly analogous to the magnetic susceptibility χ_z in the spin 1/2 transverse field Ising model with a field H_x applied equivalent to the quasi-quartet gap.

However in magnetic field the picture changes, as H_z does not follow the canonical commutation relations with O_2^2 for instance. The quasi-quartet in the presence of both a magnetic field and B_{1g} order parameter can instead be thought of as two doublets both with O_2^2 acting as a transverse field, but with longitudinal fields $\Delta_o/2 - H_z$ and $\Delta_o/2 + H_z$, and average energies shifting as $H_z/2$ and $-H_z/2$ respectively. Thus, following a similar procedure outlined for $TmAg_2$ in the previous section, the magnetic field phase boundary will be determined implicitly by this equation:

$$\frac{1}{T_Q(0)} = \frac{2e^{-H_z/2T}\frac{\sinh\left(\frac{\Delta_o+2H_z}{2T}\right)}{\Delta_o+2H_z} + 2e^{H_z/2T}\frac{\sinh\left(\frac{\Delta_o-2H_z}{2T}\right)}{\Delta_o-2H_z}}{e^{-\Delta_o/2T}\cosh(3H_z/2T) + e^{\Delta_o/2T}\cosh(H_z/2T)} \tag{1.60}$$

This is similar in shape to the spin 1/2 TFIM phase boundary but less steep and is shown in Figure 1.7. When the phase transition is suppressed to near 0K with magnetic field, note that only the thermal occupation of the doublet consisting of states $|-3/2\rangle$ and $|1/2\rangle$ will be relevant, for which H_z and O_2^2 do map precisely as transverse fields. Thus, if we restrict ourselves to considering only the $4f$ electronic lattice, its phase diagram should exhibit a quantum critical point guaranteed by the transverse field Ising model. However it is unknown how the metallic degrees of freedom will interact with the $4f$ subsystem besides providing an effective exchange through the RKKY interaction, and this motivates the resistivity measurements in the proximity of the completely suppressed phase transition that are performed in Chapter 4.

Finally we note that octupolar moments are allowed in this Hilbert space. The relevance of this will also be expanded upon in Chapter 4, where the inclusion of applied magnetic fields and strains can induce octupole moments, which can couple to the quadrupole moments and renormalize quadrupole susceptibilities.

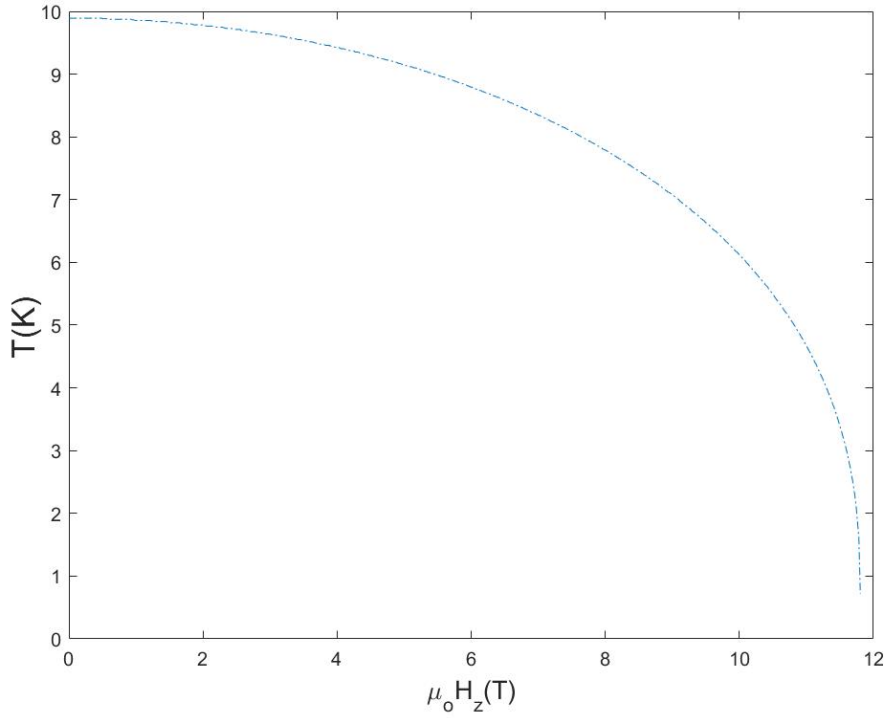

Figure 1.7: **Calculated mean-field phase diagram for the quasi-quartet described in the main text.** This model is appropriate to describe the low temperature properties of the ferro-quadrupolar phase transition of $YbRu_2Ge_2$ with applied magnetic field. The scale of the magnetic field is set such that without a gap $H_c = 10T$, although the quasi-quartet gap estimated in Chapter 4 to be $\Delta_o = 3.6K$ pushes the critical field out further.

Chapter 2

Experimental Methods

This chapter will first discuss the details of the crystal growth procedures developed for both $TmAg_2$ and $YbRu_2Ge_2$. It will then describe the measurements featured in this thesis. These include the results of several novel strain-based experiments, which serve as a pivotal aspect of this work, and so this chapter will delve into more generally how stress was applied to the material and how the corresponding strain the material experienced was approximated. How the strain-induced changes in the thermodynamic and transport properties of $TmAg_2$ and $YbRu_2Ge_2$ were measured will also be discussed in detail.

2.1 Crystal Growths of $TmAg_2$ and $YbRu_2Ge_2$

2.1.1 $TmAg_2$

$TmAg_2$ was grown by slow-cooling a stoichiometric melt, sealed in a tantalum crucible. Roughly 3 grams of Tm and the corresponding amount of Ag were added into a Ta tube that had already been welded at the bottom inside a mono-arc furnace with a Ta cap. The crucible was sealed with a top cap in a tetra-arc furnace, which had a vacuum chamber that pumped down to 1e-7 Torr. It was purged with high purity Ar gas multiple times to ensure a clean oxygen-free environment inside the crucible. The sealed Ta crucible was then sealed in quartz, and heated up to 1175°C in a box furnace and held there for 2 hours. It was cooled down to 975°C in 50 hours and held there for an additional 50 hours, to anneal the crystals *in situ*. Longer anneal times did not have a noticeable difference in the quality of the crystals as measured by RRR, which was about 100 for the cleanest crystals. The melting point of $TmAg_2$ was determined to be 1060°C $\pm$ 10°C via differential scanning calorimeter measurements.

The resulting solid contained many intergrown crystals. The solid was then crushed by a vice, and small pieces were extracted for more careful separations and alignment. Large crystalline planes

of (0 0 1) were observed. The crystals were then cut via a wire saw, aligned with single crystal X-ray diffraction, and polished to obtain rectangular samples of approximately 2mm x 0.6mm x 0.04mm for resistivity measurements and measuring the elastocaloric effect. Thicker samples were used for heat capacity measurements.

2.1.2 $YbRu_2Ge_2$

Single crystals of $YbRu_2Ge_2$ were grown using an unseeded flux method, with Indium being the flux and the other precursors added in stoichiometrically acoording to the formula $(YbRu_2Ge_2)_xIn_{1-x}$, with x varying from 0.02 to 0.04. The ratio $x = 0.025$ was found to produce both the largest size individual crystals and also the greatest yield. To help ensure inclusion of the high-melting point Ru into the melt, the elemental Ru and Ge precursors were arc-melted in a mono-arc furnace. The elements were then combined into an alumina crucible, which was sealed inside a Ta crucible to prevent oxidation and to contain the flux. The crucibles were heated in a horizontal tube furnace with flowing argon to a max temperature of 1450°C for 6-12 hours, and then cooled to 1200°C at approximately 4K/hour. The alumina crucibles were then sealed in quartz and spun in a centrifuge at 400° C or higher to remove the Indium flux from the crystals. The resulting crystals were etched in 4M HCl acid for several months until they were easily cleaveable. The resulting delicate crystals, which had a plate-like morphology, with the c-axis perpendicular to the plane of the plates, could be cleaved to a thickness of 20μm or less, and were identified and oriented using single crystal X-ray diffraction.

2.2 Elastoresistivity with microstructuring

2.2.1 Transverse Elastoresistivity

Elastoresistivity measurements were used extensively to characterize the quadrupole-strain susceptibility of the materials studied in this work. I provide here a brief introduction to the experimental measurement of elastoresistivity coefficients. Readers are referred to Shapiro et al. "Measurement of the B_{1g} and B_{2g} components of the elastoresistivity tensor for tetragonal materials via transverse resistivity configurations" [40] for a more detailed description.

The elastoresistivity tensor describes the proportionality relations between the elements of the second-rank resistivity tensor and the second-rank strain tensor and is thus a fourth-rank tensor. More specifically it is defined as the derivative of the normalized change in resistivity with respect to strain and thus can be written as:

$$m_{ij,kl} = \frac{d\left(\frac{\Delta\rho}{\rho}\right)_{ij}}{d\varepsilon_{kl}} \tag{2.1}$$

Although this is a fourth rank tensor it can be simplified by using Voigt notation, in which the elements of the second-rank tensors are arranged in a vector such that the relevant terms are labeled with numbers. $1 = xx$, $2 = yy$, $3 = zz$, $4 = xz$, $5 = yz$, and $6 = xy$. Thus the elastoresistivity terms that represent the relation between A_{1g}, B_{1g}, and B_{2g} strain and resistivity tensor elements are respectively:

$$2m_{A_{1g},1} = m_{11} + m_{12} = \frac{d\left(\left(\frac{\Delta\rho}{\rho}\right)_{xx} + \left(\frac{\Delta\rho}{\rho}\right)_{yy}\right)}{d\left(\varepsilon_{xx} + \varepsilon_{yy}\right)} \tag{2.2}$$

$$2m_{B_{1g}} = m_{11} - m_{12} = \frac{d\left(\left(\frac{\Delta\rho}{\rho}\right)_{xx} - \left(\frac{\Delta\rho}{\rho}\right)_{yy}\right)}{d\left(\varepsilon_{xx} - \varepsilon_{yy}\right)} \tag{2.3}$$

$$m_{B_{2g}} = m_{66} = \frac{d\left(\frac{\Delta\rho}{\rho}\right)_{xy}}{d\varepsilon_{xy}} \tag{2.4}$$

These are the symmetry terms that were measured in Chapter 3 for $YbRu_2Ge_2$. Later, in Chapter 4, $m_{B_{1g}}$ and $m_{A_{1g}}$ are measured as a function of field.

To experimentally measure these strain derivatives, strain was applied *in situ* to a crystal using a piezoelectric (PZT) stack. The crystal was glued to the side of the PZT stack, with the c-axis perpendicular to the plane of the PZT stack, using a rigid epoxy. The resulting coupled mechanical object comprising of a large very stiff PZT stack and a very thin sample attached to its surface is assumed to be in a limit where the sample deforms similarly to the stiffer PZT stack. The only non-ideality is then any reduction in strain that occurs through the epoxy binding the two objects. In the case of elastoresistivity measurements of microstructured $YbRu_2Ge_2$ crystals, 50μm thick silicon pieces were used as substrates which were glued onto the PZT, and so the strain is additionally reduced through them. Voltage applied to the PZT which causes it to experience a strain will also apply a strain with both anti-symmetric and symmetric parts to the crystal. A commerical strain gauge is glued on the other face of the piezo to measure the strain experienced by the PZT stack and hence estimate the strain experienced by the sample. Typical AC voltages applied to the PZT stack were 50V rms waveforms, at 1.6Hz.

To measure the anti-symmetric elements of the resistivity tensor a transverse geometry was used, which is displayed in Figure 2.1. To measure the B_{2g} resistivity element, for instance, a 5mA rms current was applied along the (1 0 0) direction and the voltage was measured along the transverse direction, (0 1 0):

$$V_y = \rho_{xy} t I_y \tag{2.5}$$

Where t is the thickness of the sample, and x and y are along the current direction and perpendicular to that direction respectively. Similarly for the B_{1g} resistivity element it was measured by applying the current along the (1 1 0) direction and measuring the voltage along the (1 -1 0) direction. This is the measurement that was performed on the sample in Figure 2.1. This voltage measurement measured contributions from both the induced B_{1g} resistivity and in-plane A_{1g} resitivity which arose from misaligned contacts (misaligned along the current path direction). To account for this contamination the symmetric A_{1g} resistivity was measured simultaneously, (via contact pads V_1 and V_2 in Figure 2.1) and the approximate zero strain value of the transverse voltage measurement was assumed to be from this misalignment. The ratio of the zero-strain transverse voltage to the longitudinal voltage determined the ratio of the length between the longitudinal contacts and the misaligned length of the transverse contacts. Strain induced changes in the transverse voltage measurement arising from the contaminating A_{1g} elastoresistivity could then be canceled out by subtracted a term multiplying this ratio by the simultaneous A_{1g} elastoresitivity measured in the voltage $V_1 - V_2$.

However obtaining the zero-strain value of the transverse voltage was non-trivial, given the gluing procedure applies strain even at room temperature. Microstructuring using a Focused Ion Beam (FIB) was instead used to lower the contamination almost completely (the room temperature ratio of R_{xy} to the R_{xx} measurement with voltage pads 300μm apart was approximately 1/100). The edges of a Hall bar pattern were etched into the sample as depicted in Figure 2.1, determining the current paths and voltage measurements. The sample were cleaved to be 30μm thick or less to reduce etching time and increase strain transmission. Before the samples were etched they were glued to 50μm thick silicon pieces which were oxidized to ensure insulating surfaces. The epoxy that was used was Angstrom Bond (AB9110), which has a low pre curing viscosity that allowed it to seep into and under the etched sections. The Si pieces were then glued on to the PZT stacks, which were Piezomechanick PST 150 (9x5x5mm) models. Strain transmission was determined to be 50% $\pm$ 3% and nearly temperature independent by first measuring with a strain gauge on top of the silicon. AC voltages were applied to the PZT, and the elastoresisitivity response was locked-in at the sum of electrical current frequency and the strain frequency using SRS 830 lock-ins. This procedure is detailed more in Ref [44]. The strain frequency used was near DC at 1.6Hz, to prevent PZT heating effects and potential anomalous frequency dependent noise.

2.2.2 Elastoresistivity measurements in magnetic fields using the Montgomery technique

For Chapter 4 elastoresitivity measurements were also performed on $YbRu_2Ge_2$ crystals in magnetic fields, but implemented different microstructured geometries to measure the resistivity tensor elements. The Montgomery technique was used to measure the resistivity, as the previously described

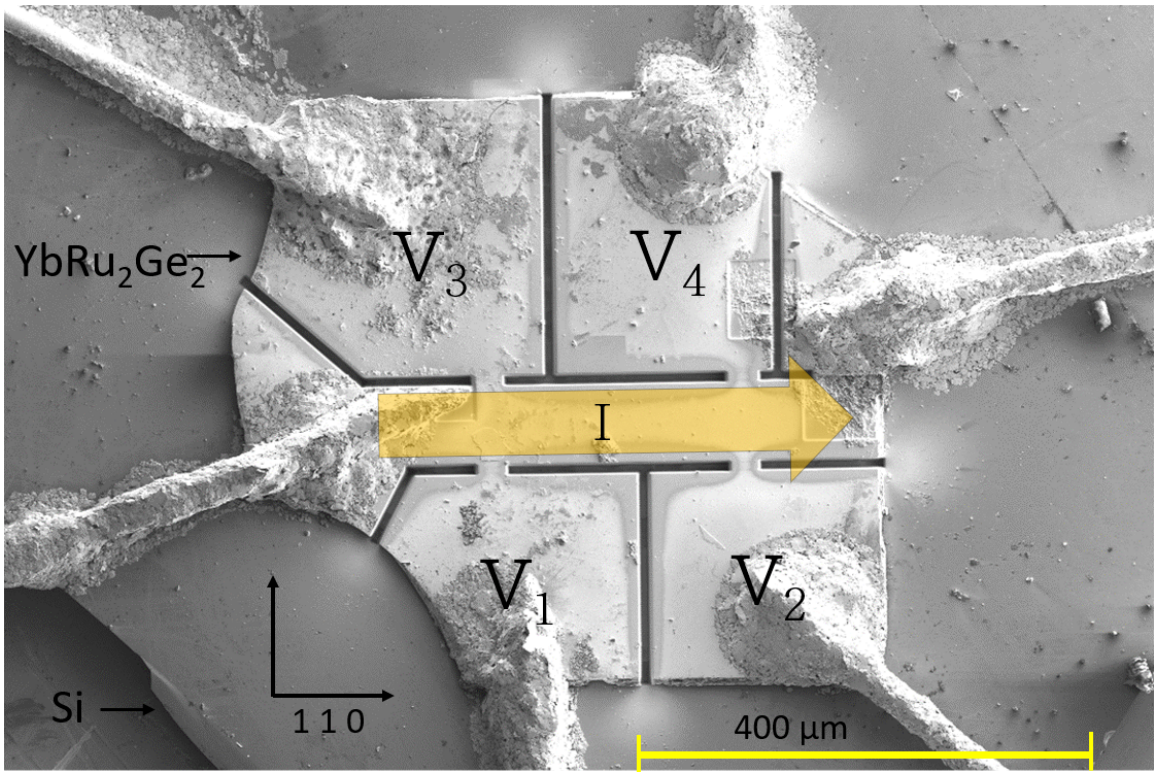

Figure 2.1: **Scanning electron micrograph of a representative micro-structured sample used for transverse elastoresistance measurements.** The $YbRu_2Ge_2$ sample is glued to a 50 μm thick Si substrate. The crystal axes (indicated by black arrows) were previously determined by x-ray diffraction, and identified here by the horizontal facets. Line cuts were etched using a Focused Ion Beam to control the current path (indicated by yellow arrow) and precisely define the voltage contact positions (labelled V_1 through V_4) .

transverse elastoresistivity method would have measured an unwanted signal in the transverse voltage measurement at finite magnetic field due to the Hall Effect. The edges of a 150μm x 150μm square were etched into the sample, leaving 15 μm x 15 μm corners unetched to allow current into the square and voltage pad placement outside of the square, as shown in Figure 2.2. Current (5mA rms) is applied between the top two corners for instance, and a voltage V_{xx} is measured at the bottom two corners. A similar arrangement is performed for V_{yy}, using horizontal pairs of corners. These voltages can be transformed to find ρ_{xx} and ρ_{yy}, using a process detailed in Ref. [43]. Because the microstructuring precisely defines the effective sample's dimensions, these transforms can be performed very accurately. For the B_{1g} measurements the square was aligned such that the edges were along (1 0 0), and the crystal was glued on the PZT such that the strains were along these directions as well. The B_{1g} resistivity mode was the simultaneous subtraction of the two resistivity measurements: $\rho_{xx} - \rho_{yy}$, and the A_{1g} mode the addition. The PZT stack was placed in the PPMS 14T cryostat such that the magnetic field was directed along the c-axis, perpendicular to the face of the crystal.

2.3 Elastocaloric Effect

For a more detailed look at this technique, we refer readers to Ref [8]. This section will discuss both the theoretical motivation for investigating the elastocaloric effect as well as how the experiments shown in Chapter 5 were performed. The elastocaloric effect is defined as the strain derivative of the temperature of the sample, and is a thermodynamic quanitity. It will be presented and derived first at a more general level relating to strain induced electronic entropy changes, and then discussed with regards to its relevancy to the materials studied in this thesis. Namely for $TmAg_2$ it can serve as a proxy for both the strain derivative of T_Q at the phase transition and the nematic susceptibility above T_Q. The measurements for the B_{2g} aligned crystals, which used RuO_2 thermometers, will be then described in detail.

2.3.1 Physical Origin of the Elastocaloric Effect

The elastocaloric effect is defined as the derivative of the temperature of the sample with respect to strains the sample experiences. Only stresses can be applied to materials, and those materials' elastic stiffness tensors determines the strains they experience resulting from the applied stress. Thus derivatives of quantities of materials with respect to strain are not trivial to measure. However by securing the sample between stiff metal plates, and measuring the displacement of the plates, the strain the sample experiences can be approximated.

As the elastocaloric effect manifests in a temperature change induced from strain the sample experiences, this quantity is ideally measured in adiabatic conditions, in which case the total entropy of the sample remains constant. Thus:

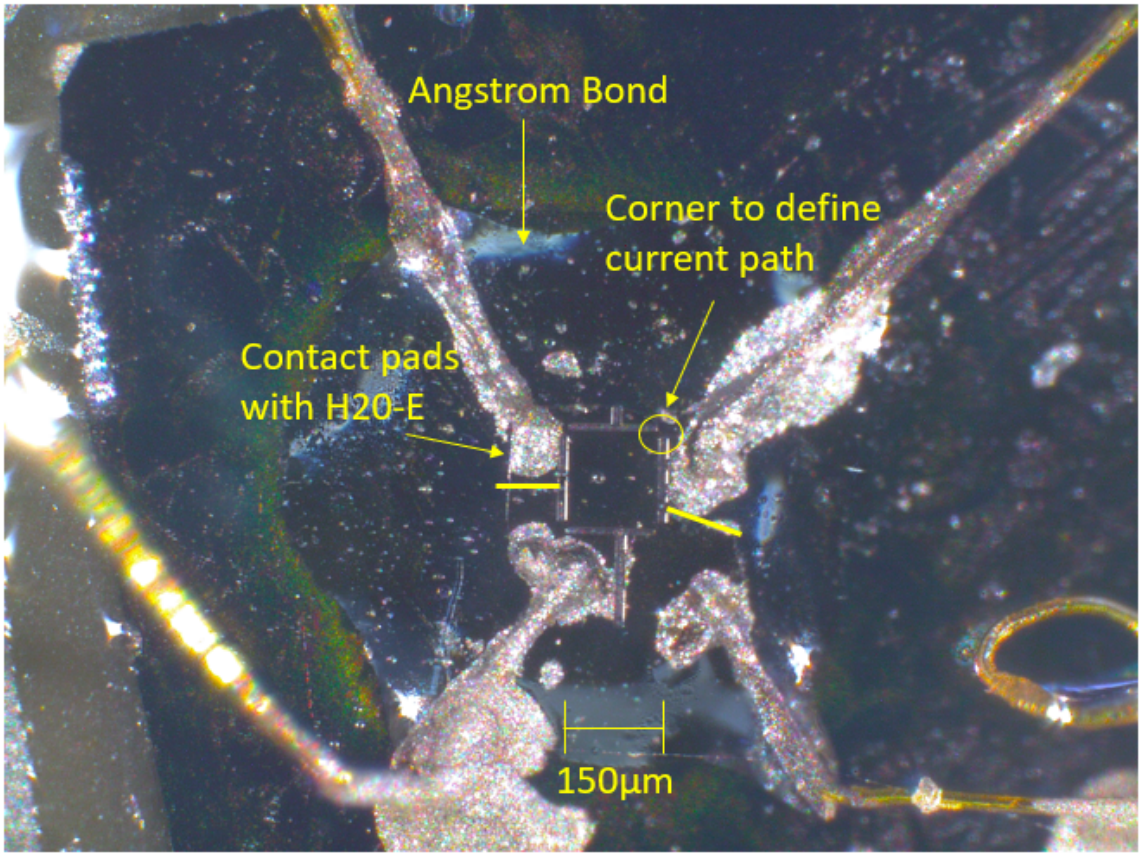

Figure 2.2: **Representative micro-structured sample used for Montgomery-style elastoresistance measurements in magnetic fields.** The $YbRu_2Ge_2$ sample is glued with Angstrom Bond to a 50 μm thick Si substrate. Line cuts were etched using a Focused Ion Beam to control the current path and precisely define the voltage contact positions such that they are at the corners of a 150μm by 150 μm square. The yellow lines are used to guide the eye to the cuts made to separate the contacts, and those contacts were formed with H-20E silver epoxy.

$$dS = \left.\frac{dS}{dT}\right|_{\varepsilon} dT + \left.\frac{dS}{d\varepsilon}\right|_{T} d\varepsilon = 0 \tag{2.6}$$

$$\frac{dT}{d\varepsilon} = -\frac{\left.\frac{dS}{d\varepsilon}\right|_{T}}{\left.\frac{dS}{dT}\right|_{\varepsilon}} = -T\frac{\frac{dS}{d\varepsilon}}{C_v} \tag{2.7}$$

For this thesis we will assume $C_v = C_p$, as the difference at low temperatures for these materials is of order 0.1% [8]. The change in temperature of the sample arises when the strain-induced isothermal change in entropy "heats" (or cools) the sample, which changes its temperature inversely to its heat capacity.

If the following three assumptions are satisfied which is the approximate case for the materials studied in this thesis (brief justification after each assumption):

- The entropy can be divided into a critical part which depends on strain and relates to a phase transition $\mathrm{S}^c(\varepsilon, T)$ and a noncritical part $\mathrm{S}^{nc}(T)$. For $4f$ intermetallics in particular, the entropy arising from the local $4f$ electronic degrees of freedom dominates over the entropy from phonons at temperatures below approximately 10K. The materials in this thesis undergo phase transitions involving the $4f$ degrees of freedom at critical temperatures that depend on strain, whereas the phonon spectrum is not strongly affected by strain.

- The critical entropy $\mathrm{S}^c(\varepsilon, T)$ is only strain dependent through strain moving the transition temperature, and so strain does not changes its shape but only shifts it. $S^c = S^c(T - T_Q(\varepsilon))$. For the mean-field transverse field Ising model this is approximately true for small strains. For $TmAg_2$ we have shown that the $4f$ system maps to this model with B_{2g} strain as a transverse field, and so hence we have reason to believe this assumption will be true for small strains of that symmetry.

- The corresponding heat capacity parts are $\mathrm{C}_p^c(\varepsilon, T)$ and a non critical background $\mathrm{C}_p^{nc}(T)$ This is satisfied if assumption 1 is satisified, as $C_p = T\frac{dS}{dT}|_p$

Then an alternate more informative form of Eq. 2.7 is (justification appears in Ref. [8]):

$$\frac{dT}{d\varepsilon} = \frac{C_p^c}{C_p^c + C_p^{nc}} \frac{dT_Q}{d\varepsilon} \tag{2.8}$$

For the materials studied in this work, the ratio of the critical parts of the heat capacity against the non-critical part experiences a large jump at the low temperature phase transitions, and so one expects a large signal proportional to the derivative of the phase transition temperature with strain at T_Q.

Not only will the elastocaloric effect probe the strain derivatives of the ferroquadrupolar phase transitions, but it will also be sensitive of the nematic/quadrupole-strain susceptibilities. To motivate this, consider the free energy for a system above a nematic phase transition, and minimize it with respect to the electronic nematic order parameter:

$$\begin{aligned} F &= \frac{a_o}{2}(T - T^*)\psi^2 - \lambda\psi\varepsilon \\ \frac{dF}{d\psi} &= a_o(T - T^*)\psi - \lambda\varepsilon = 0 \\ \psi &= \frac{\lambda}{a_o(T - T^*)}\varepsilon = \chi_N\varepsilon \\ F &= -\frac{\lambda^2\varepsilon^2}{2a_o(T - T^*)} = -\frac{\lambda\chi_N}{2}\varepsilon^2 \end{aligned} \tag{2.9}$$

Where ψ represents the nematic order parameter, λ the bilinear coupling constant, ε the strain of the appropriate symmetry, and χ_N is the nematic susceptibility. Since $S = -\frac{dF}{dT}$

$$\begin{aligned} \frac{dS}{d\varepsilon} &= \frac{d}{d\varepsilon}\left(-\frac{dF}{dT}\right) = \lambda\varepsilon\frac{d\chi_N}{dT} \\ \frac{dT}{d\varepsilon} &= -\frac{T}{C_p}\lambda\varepsilon\frac{d\chi_N}{dT} \end{aligned} \tag{2.10}$$

Thus the elastocaloric effect above the phase transition will have a signal proportional to the external strain on the system and the derivative of the nematic susceptibility. $TmAg_2$ allows more than one symmetry channel for an order parameter which couples to strain to exist (both the B_{1g} order parameter which spontaneously develops in the phase transition, and a B_{2g} quadrupole which couples to ε_{xy}), and so different alignments of the strain being applied will induce different susceptibility terms to be present in the elastocaloric effect.

2.3.2 Elastocaloric Experimental setup

This experimental setup is based off of the methods described in Ref. [8], the reader is referred there for more detailed explanations of this experiment. More generally this experimental setup can be viewed as a three element thermal circuit, in which the thermometer is thermally connected to the sample, which is thermally connected to the bath that applies a stress to the sample. As mentioned in the beginning of this section, an experimental setup that accurately measures the elastocaloric effect, must be adiabatic or quasi-adiabatic, otherwise the heat generated by the sample will dissipate into the environment and no corresponding temperature fluctuations will be measured. It also must enable the thermometer to thermally couple to the sample well enough to measure a substantial fraction of the sample's temperature fluctuations. In order to measure the elastocaloric effect these three major techniques were implemented:

- The sample is glued between the mounting plates of a commercial Razorbill CS-100 strain cell

rather than on a piezoelectric stack, so as to reduce thermal conductivity to the bath.

- AC stress was applied from the strain cell, and the frequency was tuned such that period of oscillations of the strain was between the (fast) thermal time constant of the thermometer on top of the sample and the (slow) thermal time constant to the bath.
- The displacement of the plates was measured through a capacitive sensor on the strain cell, and this was approximated as the displacement of the sample.

To increase strain transmission a hard epoxy (Stycast 2850FT Epoxy) was used to secure the sample between two sets of mounting plates as depicted in Figure 2.3. The samples were polished as thin as possible (approximately 50μm thick) to ensure that only the sample distorted in repsonse to the voltage applied to the strain cells' inner PZT stacks and not the titanium body of the cell. Nonetheless, as $TmAg_2$ is quite hard, when the sample was attached the displacement per volt of the strain cell was found via the capacitance measurement to be 64% $\pm$ 3% of the calibrated value of the cell without a sample at temperatures from 2K to 20K, indicating the sample had a substantial spring constant, and that the body did indeed distort during the measurement. The sample geometry was roughly 2mm x 0.6mm x 0.05mm, with a sample gap of 0.6mm.

The temperature fluctuations were measured using a RuO_2 resistor/thermometer which was heat piped to the sample via a 50μm diameter gold wire, as shown in Figure 2.3. The thermometers that were chosen were 2500 Ω resistors, as this ensured a large signal but necessitated a small excitation current ($\sim$ 0.1mA) to avoid self-heating. The gold wire was silver painted to the sample as well as the back of the thermometer, to provide high thermal conductivity from the thermometer to the sample. The thermometer was polished to have dimensions of 150μm x 75μm x 20μm to reduce its heat capacity. This reduction decreased the thermal time constant of the connection to the sample, and also reduced the error in the estimation of the value C_v^{nc}.

The temperature signal was measured at the sum of the strain frequency and the thermometer excitation frequency, similar to the AC elastoresistivity technique described in section 2.1.1 and in Ref [44]. A small current (0.1mA) at approximately 500 Hz was applied to the thermometer to reduce self-heating. To reduce the thermal conductivity of the thermometer to the probe wiring and the thermal bath high thermal resistance constantan wires were used for contacting. To increase the signal to noise ratio the thermometer was measured using a custom Wheatstone bridge in which the 3 other resistive components were identical resistors to the thermometer, and the bridge was thermally anchored to the cell. This ensured that the background temperature of all 4 components of the bridge was nearly the same, implying the Wheatstone bridge was balanced at all probe temperatures. The resulting output voltage of the bridge consisted nearly solely of the temperature fluctuations caused by the sample's elastocaloric effect, and the total signal was then demodulated with a SRS 860 lock-in at the strain frequency of 72 Hz. This frequency was empirically found to correspond to the maximum of the thermal transfer function of the temperature fluctuations of

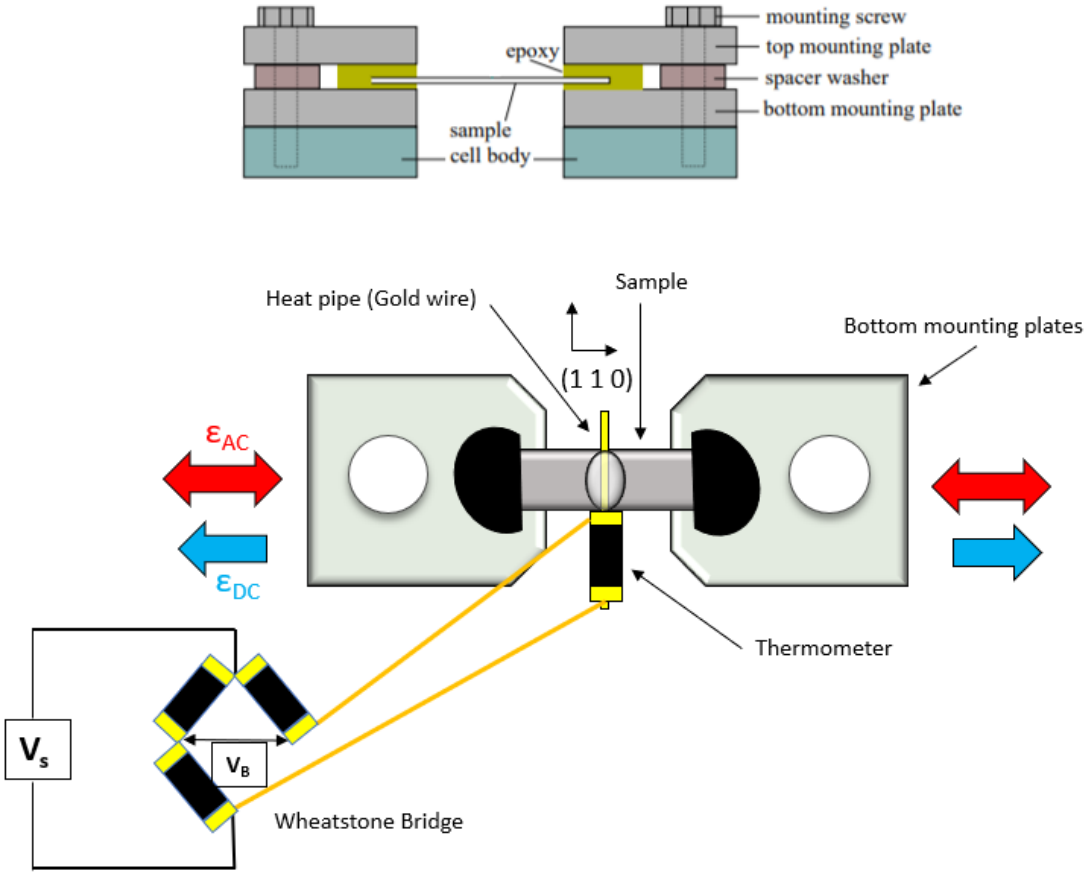

Figure 2.3: **Schematic of the elastocaloric experimental setup.** The top picture represents a side view of the sample secured between the jaws of the strain cell, and this figure was taken from Ref. [8]. The bottom schematic represents the top view before the final top set of mounting plates are positioned. The black semi-circles represent the Stycast epoxy, which secures the edges of the sample to both the bottom and top sets of mounting plates. The orange lines represent the thermally resistive constantan wires which electrically connect the thermometer's contact pads (represented by yellow rectangles) to the corresponding resistors' contact pads of the Wheatstone Bridge, which is thermally anchored to the strain cell in reality, expanded in the lower left hand corner. V_s is the source voltage for the bridge, and V_B is the output voltage of the bridge which isolates the temperature fluctuations of the thermometer and sample. The parts of the Wheatstone bridge where the resistors' contact pads touch represent electrical contacts. Notice that the stress is aligned along (1 1 0), so this is a B_{2g} measurement.

the sample. The thermal transfer function is similar to one described in Ref [8], just shifted up in frequency due to the increased ratio of thermal conductivities to heat capacities of the various experimental components at lower temperatures. An AC voltage of 20V rms was applied to the outer PZT stacks of the strain cell, which corresponded to applying an AC displacement of the sample of roughly 0.01% of its length. Previous works have estimated via finite element simulations that the typical strain transmission ratio using standard epoxies is roughly 70% [8], so any absolute values of strains that are referenced are not known precisely and most likely overestimations. This setup is depicted in the schematic in Figure 2.3.

To obtain the value of the temperature fluctuations of the sample the thermometer was assumed to have a negligible heat capacity compared to the sample, for which the sample and the thermometer would be at the same temperature. The thermometer's resistance vs temperature was calibrated by thermally anchoring it to a PPMS sample block and measuring resistance while slowly sweeping temperature down previous to the elastocaloric measurement. From this calibration the AC strain induced temperature fluctuations of the sample could be calculated as :

$$\frac{dT}{d\varepsilon} = \frac{1}{I_o}\frac{dV_{Th}}{d\varepsilon} * \frac{1}{\frac{dR_{Th}}{dT}} \tag{2.11}$$

Where V_{Th} and R_{Th} denote the voltage and resistance of the thermometer respectively, and I_o is the current sent through the thermometer.

For B_{2g} measurements the crystal was aligned such that principal stress axis was along (1 1 0). This induced strains of B_{2g} character as well as A_{1g} character. Because the resultant temperature change of the sample is not a tensor, the elastocaloric technique cannot isolate the entropy response of the material to different symmetry strains, but the temperature signal combines them instead. Thus it is important to determine the relative amounts of different symmetry strains the sample is experiencing. The ratio of the strain components is dependent on the elastic constants of the material through the relevant poisson ratio:

$$\frac{\varepsilon_{B_{2g}}}{\varepsilon_{A_{1g}}} = \frac{1+\nu_2}{1-\nu_2} \tag{2.12}$$

Where ν_2 refers to the in-plane poisson ratio for stress applied along (1 1 0), and ν_1 would refer to the in-plane poisson ratio for stress applied along (1 0 0). Following this notation, the in-plane poisson ratios for tetragonal materials in general is:

$$\nu_i = \frac{-C_{13}^2 + \left(\frac{C_{A_{1g},1} - C_{B_{ig}}}{2}\right)C_{33}}{-C_{13}^2 + \left(\frac{C_{A_{1g},1} + C_{B_{ig}}}{2}\right)C_{33}} \tag{2.13}$$

Where ν_1 incorporates the B_{1g} elastic constants and ν_2 incorporates B_{2g} elastic constants.

Unfortunately for measurements with stress applied along (1 1 0), the relevant elastic constants are unknown, but is assumed that because none of them are expected to soften that the poisson ratio ν_2 is essentially temperature independent. If C_{33} and C_{13} do not vary much in the temperature window of 20-2K, which is to be expected, then Eq. 2.13 implies that the ratio of the displacement of the sample and $\varepsilon_{B_{2g}}$ experienced by the sample is constant in the temperature regime of the experiment discussed in Chapter 5.

For future B_{1g} measurements (not shown in thesis) the stress from the strain cell will be aligned along (1 0 0). For this alignment the ratio between the anti-symmetric and symmetric strains will not be temperature independent, as the B_{1g} elastic constants undergo a pronounced softening, shown in Ref [3].

Chapter 3

Divergence of the quadrupole-strain susceptibility of the electronic nematic system $YbRu_2Ge_2$

This work appeared in Ref. [11].

3.1 Abstract

Ferroquadrupole order associated with local $4f$ atomic orbitals of rare earth ions is a realization of electronic nematic order. However, there are relatively few examples of intermetallic materials which exhibit continuous ferroquadrupole phase transitions, motivating the search for additional materials that fall into this category. Furthermore, it is not clear *a priori* whether experimental approaches based on transport measurements which have been successfully used to probe the nematic susceptibility in materials such as the Fe-based superconductors, will be as effective in the case of $4f$ intermetallic materials, for which the important electronic degrees of freedom are local rather than itinerant and are consequently less strongly coupled to the charge-carrying quasiparticles near the Fermi energy. In the present work, we demonstrate that the intermetallic compound $YbRu_2Ge_2$ exhibits a tetragonal-to-orthorhombic phase transition consistent with ferroquadrupole order of the Yb ions, and go on to show that elastoresistivity measurements can indeed provide a clear window on the diverging nematic susceptibility in this system. This material provides a new arena in which to study the causes and consequences of electronic nematicity.

3.2 Introduction

Electronic nematic order in crystalline solids corresponds to a spontaneously broken discrete rotational symmetry driven by interactions between low-energy electronic degrees of freedom [12]. The empirical observation that nematic order occurs in, or near to, superconducting phases in Fe-based materials [13, 14, 15, 16, 17] and possibly also cuprates [18, 19, 20, 21, 22, 23, 24, 25, 26] motivates a series of fundamental questions about the possible role(s) that nematicity might play in such systems [27, 28, 29, 30]. Fe-based and cuprate superconductors are complicated materials, with a variety of other intertwined electronic phases, making it highly desirable to identify simpler model systems that exhibit nematic order for which the underlying effective Hamiltonian is better-understood. Ferroquadrupole order associated with local $4f$ atomic orbitals of rare earth ions is a realization of electronic nematic order [31], and in principle can provide just such a model system.

The effective Hamiltonian describing the low energy properties of rare earth ions incorporated in crystalline solids is understood in great detail. The $4f$ electronic wavefunctions are spatially localized, and strong spin-orbit coupling yields an electronic multiplet that is described by a total angular momentum number J. Due to the local nature of the electrons, the crystal electric field (CEF) from the surrounding ligands acts as a weak perturbation, splitting the degeneracy of the $2J + 1$ spherical harmonic basis states. Significantly, the low energy states of these $4f$ electronic multiplets can exhibit degeneracies or near degeneracies. In these degenerate or near degenerate manifolds, there can exist states with large multipolar moments. Both the coupling of the lattice with quadrupolar degrees of freedom, and a $4f - 4f$ coupling from the generalization of the RKKY interaction mediated by conduction electrons, can then provide energetically favorable conditions for multipolar instabilities to occur [2]. A variety of multipolar behavior has been observed in such materials. The specific case of ferroquadrupole order, in which each atomic site takes on a quadrupole moment of the same orientation, breaks the rotational symmetry of the point group of the crystal and hence provides an example of a lattice in which sites exhibit collective nematic order. There are, however, relatively few examples of intermetallic materials which exhibit continuous ferroquadrupole phase transitions, the primary examples being tetragonal-to-orthorhombic phase transitions observed for $TmAg_2$ [3] and $TmAu_2$ [33, 32], motivating the search for additional materials that fall in to this category. The present work adds $YbRu_2Ge_2$ to that list.

$YbRu_2Ge_2$ has a tetragonal crystal structure at room temperature (space group I4/mmm), belonging to the same $ThCr_2Si_2$ structure type as the familiar "122" Fe-pnictides such as $BaFe_2As_2$. The $4f$ electrons of the trivalent Yb ion form local multiplets with a total angular momentum quantum number J = 7/2. The CEF for the tetragonal point group symmetry results in 4 Kramers doublets, two with Γ_6 and two with Γ_7 character [34] (see Section 3.6.1). The material displays some weak heavy fermion characteristics [4], but the low temperature properties can be well-understood in terms of these local $4f$ orbitals [34]. Analysis of heat capacity, susceptibility and inelastic neutron scattering measurements indicate that the CEF groundstate is a quasi-quartet comprising states

with almost pure $m_j = |\pm 1/2\rangle$ (Γ_6) and $m_j|\pm 3/2\rangle$ (Γ_7) character, split by approximately 300 K from the other two doublets [4, 34]. The material exhibits three continuous phase transitions at low temperature associated with the quasi-quartet: a non-magnetic phase transition at $T_Q = 10.2$K, and two magnetic phase transitions (one at $T_{N1} = 6.5$K, corresponding to the onset of a collinear amplitude modulated antiferromagnet state, and a subsequent one at $T_{N2} = 5.7$K, the origin of which is currently unknown [4, 35]). Based on analysis of the multipole moments of the CEF groundstate, combined with a mean-field treatment of the effective Hamiltonian for the system, it has been suggested that the origin of the non-magnetic transition is a ferroquadrupolar ordering of the local $4f$ electrons (see Ref. [4] and Section 3.6.3). However, to-date no measurements have confirmed the ferroquadrupolar nature of the phase transition, nor has the quadrupole strain susceptibility been investigated.

In the present work, we use high-resolution X-ray diffraction to reveal that the non-magnetic phase transition corresponds to a tetragonal-to-orthorhombic phase transition, consistent with spontaneous ferroquadrupole order with a B_{1g} symmetry. We then present elastoresistivity measurements which reveal a divergence of the quadrupole strain susceptibility (i.e. the nematic susceptibility) in the same (B_{1g}) symmetry channel, $\chi_{B_{1g}}$. Comparison of the divergence of $\chi_{B_{1g}}$ and the critical temperature for the ferroquadrupole order T_Q allows evaluation of the Levy criterion (defined below), from which it is inferred that the ferroquadrupole transition in $YbRu_2Ge_2$ is driven primarily by magneto-elastic coupling. Our measurements establish $YbRu_2Ge_2$ as a model system to explore electronic nematicity, for example as a possible starting point from which the ferroquadrupole order could be continuously suppressed towards a nematic quantum phase transition.

We start by describing the quadrupole strain susceptibility (i.e. the nematic susceptibility for the $4f$ quadrupolar system) and its significance for ferroquadrupole order.

A minimal Hamiltonian can be written down which describes the quadrupolar behavior of the $4f$ electrons in $YbRu_2Ge_2$:

$$H_{eff} = H_{CEF} + \sum_i -\Big(B_i Q_i \varepsilon_i + K_i \langle Q_i \rangle Q_i\Big) \tag{3.1}$$

The first term in the sum is the bilinear magnetoelastic quadrupole-strain coupling, and the second term is a mean-field quadrupole interaction term originating from an effective RKKY coupling mediated by the conduction electrons [2]. The sum is over the three relevant symmetry channels for the tetragonal system, A_{1g}, B_{1g}, and B_{2g}. Q_i are the quadrupole operators of the ith symmetry channel (for B_{1g} symmetry these are $O_2^2 = J_x^2\text{-}J_y^2$, for B_{2g} symmetry $P_{xy} = (J_xJ_y+J_yJ_x)/2$), and ε_i is the corresponding strain (for B_{1g} symmetry, $(\varepsilon_{xx} - \varepsilon_{yy})/2$, for B_{2g} symmetry, ε_{xy}). H_{CEF} describes the crystal electric field from the surrounding Ru and Ge atoms that produces the ground state quasi-quartet (See Section 3.6.1). The gap between the ground state doublet and first excited doublet has been proposed to be $\Delta_{CEF_1} \approx 10K$ from entropy considerations [4]. The other doublets have been shown to be much higher in energy ($\Delta_{CEF_2} \approx 300K$) and can be ignored for any low

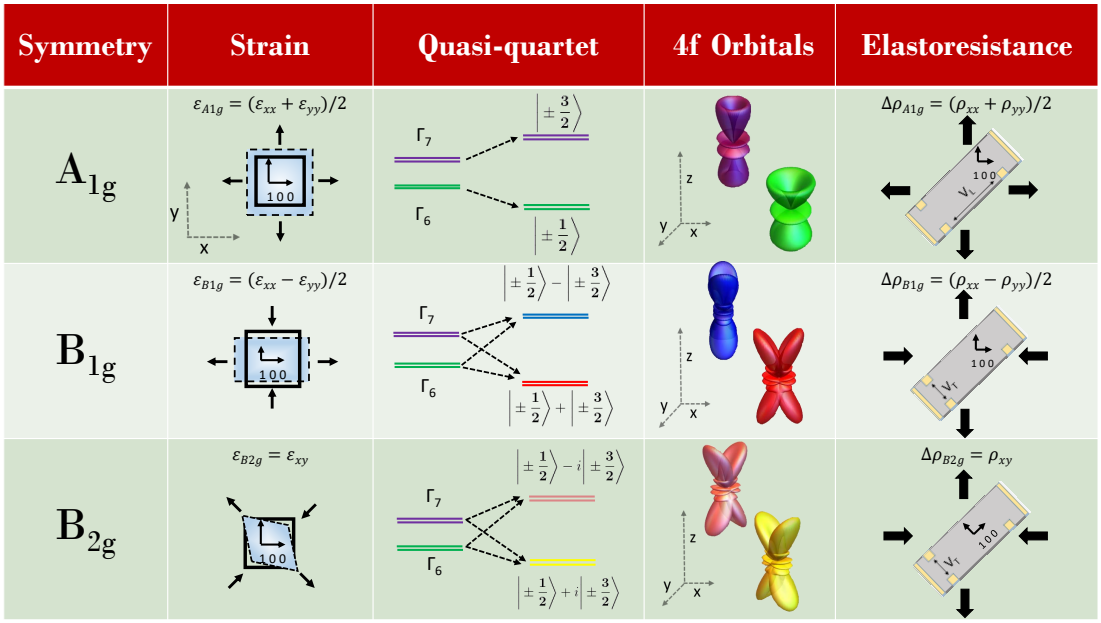

Figure 3.1: **Effect of strains of different symmetries on the CEF eigenstates of $YbRu_2Ge_2$, and measurement of the associated elastoresistivity coefficients.** Strains corresponding to distinct irreducible representations, induced by external stresses, are indicated by thick black arrows. These strains admix and split the CEF eigenstates; the effect on the low energy CEF quasi-quartet and the charge density of the ground state orbitals is illustrated. For simplicity, the Γ_6 and Γ_7 eigenstates are illustrated for pure $|\pm 1/2\rangle$ and $|\pm 3/2\rangle$ character respectively (see main text). The far right column shows the required orientation of the normal strain (thick black arrows), crystal axes (insets to grey schematic crystals) and voltage contacts (yellow pads, with measured voltages indicated for longitudinal and transverse pairs) for measurement of the associated elastoresistivity coefficients in each symmetry channel.

temperature physics.

Strain ϵ_i, induced by an external stress, admixes and splits the CEF eigenstates (see Figure 3.1), resulting in an induced quadrupole moment. The associated quadrupole strain susceptibility χ_i can be defined for each symmetry channel i. Considering first the case in which $K_i = 0$, the quadrupole strain susceptibility has the form

$$\chi_i = \left.\frac{dQ_i}{d\varepsilon_i}\right|_{\varepsilon\to 0} = \frac{2\langle q_i\rangle_o^2 B_i}{\Delta_{CEF_1}} \tanh\left(\frac{\Delta_{CEF_1}}{2T}\right) \tag{3.2}$$

where $\langle q_i\rangle_o$ is the magnitude of the quadrupole moment (see Section 3.6.3). In the limit $T > \Delta_{CEF_1}$, this reduces to an approximate Curie form $\chi_i \sim \frac{\langle q_i\rangle_o^2 B_i}{T}$, which becomes exact for $\Delta_{CEF_1} = 0$.

Adding quadrupole interactions to this model renormalizes the quadrupole-strain susceptibilities. Considering again the limit $\Delta_{CEF_1} = 0$, this results in a Curie-Weiss functional form:

$$\chi_i' = \left(\frac{dQ}{d\epsilon}\right)_i = \frac{\langle q_i\rangle_o^2 B_i}{T - \langle q_i\rangle_o K_i} \tag{3.3}$$

Thus the Weiss temperature of the quadrupole-strain susceptibility in a given symmetry channel is proportional to the strength of the quadrupole-quadrupole interaction term and the saturated quadrupole moment in that channel. If the lattice were infinitely stiff (i.e. strain is treated as a fixed parameter), the system would have a tendency to undergo quadrupolar order at this "bare" critical temperature.

Of course, the lattice is not infinitely stiff, and the magneto-elastic coupling renormalizes the critical temperature. Minimizing the free energy with respect to strain, including the elastic energy terms, the ordering temperature is found to be:

$$T_Q = \left(\left(K + \frac{B^2}{C}\right)\langle q\rangle_o\right)_i = G_i\langle q_i\rangle_o \tag{3.4}$$

Where B and C are the magnetoelastic and elastic constants respectively of the ordering symmetry channel i, and G represents the renormalized quadrupolar interaction coefficient.

The relative magnitudes of $\frac{B_i^2}{C_i}$ and K_i dictates whether the nematic phase transition is driven by strain, in the traditional Cooperative Jahn-Teller sense [36] or by electronic quadrupolar fluctuations, as inferred for certain $4f$ ferroquadrupole systems [2, 3, 32] and underdoped "122" Fe-pnictides [37, 15, 17]. Thus a precise measurement that determines the ratio of these two components, known as the Levy criterion, is an essential development to understanding the nature of quadrupolar phase transitions in any given $4f$ system.

While the quadrupole-strain susceptibility is frequently invoked from a theoretical perspective [2], it has rarely been determined experimentally. Simple consideration of thermodynamic relations imply that χ_i can be inferred from softening of the elastic constants, magnetostriction, and measurements of the third-order magnetic susceptibility [2], and all of these approaches have been

utililized previously in other candidate $4f$ systems [33]. However, while measurements of the elastic moduli provide a direct perspective on the lattice symmetry modes, a large temperature dependent background and a strict reliance on a suitable geometry of the sample make it difficult in practice to obtain the temperature-dependence of χ_i with quantitative accuracy. Similarly, magnetic measurements face difficulties in obtaining the temperature-dependence of χ_i, in part because of issues with demagnetization fields, and in part because quadrupolar-field susceptibilities must be untangled from the quadrupole-strain susceptibilities to properly infer them. Here, rather than inferring χ_i based on a combination of thermodynamic measurements, we outline how this quantity can be determined via elastoresistance measurements.

Although resistivity is not a thermodynamic measurement, it is a sensitive measure of the electronic scattering rate in a crystal. Considering $4f$ intermetallic systems, the local $4f$ electronic sites serve as strong scatterers of the conduction electrons. Anisotropic scattering from these sites and their associated quadrupolar moments has previously been described for cubic materials [38] but not investigated in the context of quadrupolar phase transitions in tetragonal materials. Under two conditions, which can be readily justified for $YbRu_2Ge_2$, we can directly relate a change in the normalized anisotropic resistivity (divided by the isotropic resistivity) to a change in the corresponding quadrupole moment (see Section 3.6.5, and [39]). The first condition is that the resistivity is dominated by scattering of the conduction electrons from the lattice of $4f$ electronic mutliplets. As we demonstrate, this is indeed the case for $YbRu_2Ge_2$. The second condition is that the induced quadrupole moment is perturbative, which is by definition the case for the technique that we use to determine the elastoresistivity.

When these two conditons are satisfied, an elastoresistivity technique, in which a tunable strain is applied to a material while measuring the induced anisotropic resistivity (illustrated schematically in Figure 3.1), provides an ideal method to directly probe the temperature-dependence of the material's quadrupole-strain susceptibility. For example, considering the B_{1g} symmetry channel (second row of Figure 3.1), a B_{1g} symmetry strain (caused by some external stresses) induces a finite B_{1g} symmetry change in the resistivity $(\frac{\Delta\rho}{\rho})_{B_{1g}} = \frac{(\rho_{xx}-\rho_{yy})}{\rho_0}$ where ρ_{xx} and ρ_{yy} are measured in the presence of the strain and ρ_0 is the unstrained isotropic in-plane resistivity. If the scattering rate Γ is dominated by scattering from the 4f orbitals, and if the effective mass of the conduction electrons is not strongly affected by the induced strain, then

$$\left(\frac{\Delta\rho}{\rho}\right)_{B_{1g}} \approx \left(\frac{\Gamma_{xx}-\Gamma_{yy}}{(\Gamma_{xx})_0+(\Gamma_{yy})_0}\right)_{4f} \propto \langle O_2^2\rangle \tag{3.5}$$

Taking the appropriate derivatives with respect to strain gives:

$$\frac{\left(\frac{d\rho}{\rho}\right)_{B_{1g}}}{d\varepsilon_{B_{1g}}} \propto \chi_{B_{1g}} \tag{3.6}$$

Thus, measuring the symmetry decomposed elements of the elastoresistivity tensor provides direct measurements of the corresponding quadrupole-strain susceptibilities. Appropriate orientation of crystal axes, normal strain axes, and contact placement necessary to measure each symmetry channel are illustrated in Figure 3.1, and described in greater detail in [40].

Elastoresistance techniques have previously been used to determine the nematic susceptibility of materials for which the nematicity derives from itinerant electronic states, including Fe-based superconductors [37, 41, 42, 40, 43, 44] and URu_2Si_2 [45]. Here, we demonstrate that the technique is also appropriate to determine χ_i of materials that undergo ferroquadrupole order of local $4f$ orbitals. Since for such systems χ_i can in principle be large in several symmetry channels i, we introduce new means (described in Materials and Methods) to ensure appropriate symmetry decomposition, using a Focused Ion Beam to prepare the sample for each measurement.

3.3 Materials and Methods

Single crystals of $YbRu_2Ge_2$ were grown from a high-temperature indium flux, as described elsewhere [46] (see Section 3.6.9.) The flux was decanted in a centrifuge and the crystals etched in HCl acid for several months. The resulting crystals, which had a plate-like morphology, with the c-axis perpendicular to the plane of the plates, could be cleaved to a thickness of 20μm or less, and were identified and oriented using single crystal X-ray diffraction.

Low temperature, high-resolution, X-ray diffraction measurements were performed on beamline A2 at CHESS (Cornell High Energy Synchrotron Source). The intensity profiles of the (6 0 0) Bragg peak were mapped out in momentum space from 40K to 6.6K. The orthorhombicity parameter $(a-b)/(a+b)$ was obtained by finding the first moment of the intensity (integrating counts multiplied by position) of line scans of the orthorhombic Bragg peaks (see Section 3.6.2). Flat samples with a uniform thickness between 5 and 20 μm were bonded to 50 μm thick Si substrates using Angstrom Bond (AB9112-2.5G). Current and voltage contacts were made by connecting gold wires to the sample using Epotech H-20E silver paste. Hall-bar patterns were then etched into the sample using a Focused Ion Beam (FIB) (see Section 3.6.8 for beam parameters) in order to precisely define current directions and contact geometry (Figure 3.1). Typical bar dimensions were 200-400μm in length, by 70-120μm in width. The Si substrate was then bonded to the center of a side of a Piezomechanick 5x5x9 mm PZT piezoelectric stack (Piezomechanik PSt150/5x5/7 cryo 1) in the appropriate orientation using Devcon 5-Minute Epoxy. Uncertainty in alignment with respect to the crystal axes was estimated to be less than 2 degrees. Strains experienced by the sample as a consequence of varying the voltage applied to the PZT stack were estimated via resistive strain gauges positioned on the opposite side of the piezoelectric stack, as well as a resistive strain gauge glued on top of a Si substrate mounted on the PZT [37]. The PZT stack was mounted on a thermally anchored probe in a helium flow cryostat.

To ensure that the elastoresistive response was linear, the voltage applied to the PZT stack was varied while the temperature was held constant, and the sample's response plotted against that of the strain gauge. For both B_{1g} and B_{2g} responses, the elastoresistance was always linear. Detailed elastoresistivity measurements were then taken using an amplitude demodulation technique, following the method described in Ref. [44]. This technique was applied using a 1.6Hz 50V rms sinusoidal excitation while simultaneously driving a 5 mA rms current through the sample at 107 Hz, sourced by a Keithley 6221 DC and AC current source. The combination of mechanical and electrical excitations produces voltage signals at the sum and difference of the two frequencies, proportional to the unstrained resistivity of the sample. The signal is first measured by a SRS830 lock-in amplifier (LIA) with a time constant $<$ 30ms referenced to 107 Hz, and the output of that LIA is measured by a second LIA with a time constant of $>$ 3s referenced at 1.6Hz to detect the elastoresisitivity signal. Care was taken to ensure the phase of the output signal was properly accounted for and the strain was measured simultaneously [44]. Strain transmission was measured from the piezo surface to the top surface of the Si where the samples were glued, and was determined to be roughly 50% and essentially temperature independent from 4K to 100K. This was taken into account in determining the magnitude of the elastoresistivity coefficients. Data were taken while the temperature was slowly swept between 4 K and 100 K.

A 1.6Hz 50V rms sinusoidal wave was applied to the PZT stack. The carrier frequency for the current in the sample was locked-in to using an SRS830 lock-in amplifier (LIA). The display output from this LIA was input to another SRS830 to lock-in to the strain modulation of the resistivity at 1.6Hz. Time constants for the current LIA were kept to $<$30ms to avoid attenuation of the strain sideband. Care was taken to ensure the phase of the output signal was properly accounted for and the strain was measured simultaneously [44]. Strain transmission was measured from the piezo surface to the top surface of the Si where the samples were glued, and was determined to be roughly 50% and essentially temperature independent from 4K to 100K. This was taken into account in determining the magnitude of the elastoresistivity coefficients. Data were taken while the temperature was slowly swept between 4 K and 100 K.

3.4 Results

Splitting of the (6 0 0) Bragg peak was observed below 10.2K along the (1 1 0) and (1 -1 0) directions, with the new peaks indicative of a B_{1g} orthorhombic structural distortion. The temperature dependence of the orthorhombicity parameter of $YbRu_2Ge_2$ is shown in Figure 3, together with the anticipated temperature dependence of a mean-field Ising order parameter that onsets at 10.2 K [56]. No evidence for a similar phase transition is found for the non-magnetic analog YRu_2Ge_2 (see [47] and inset to Figure 3.4). The data for $YbRu_2Ge_2$ are consistent with a continuous ferroquadrupole phase transition, as predicted previously based on analysis of the CEF parameters [4]. Of the two

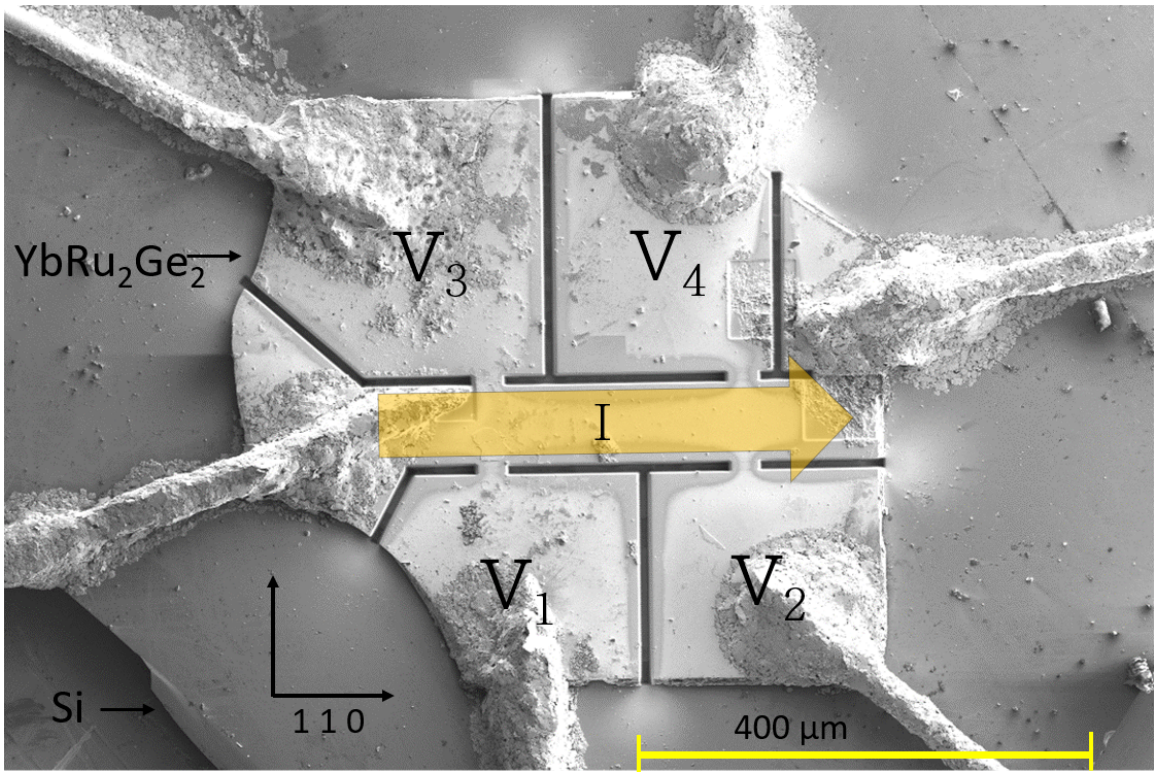

Figure 3.2: **Scanning electron micrograph of a representative micro-structured sample used for elastoresistance measurements.** The $YbRu_2Ge_2$ sample is glued to a 50 μm thick Si substrate. The crystal axes (indicated by black arrows) were previously determined by x-ray diffraction, and identified here by the horizontal facets. Line cuts were etched using a Focused Ion Beam to control the current path (indicated by yellow arrow) and precisely define the voltage contact positions (labelled V_1 through V_4) .

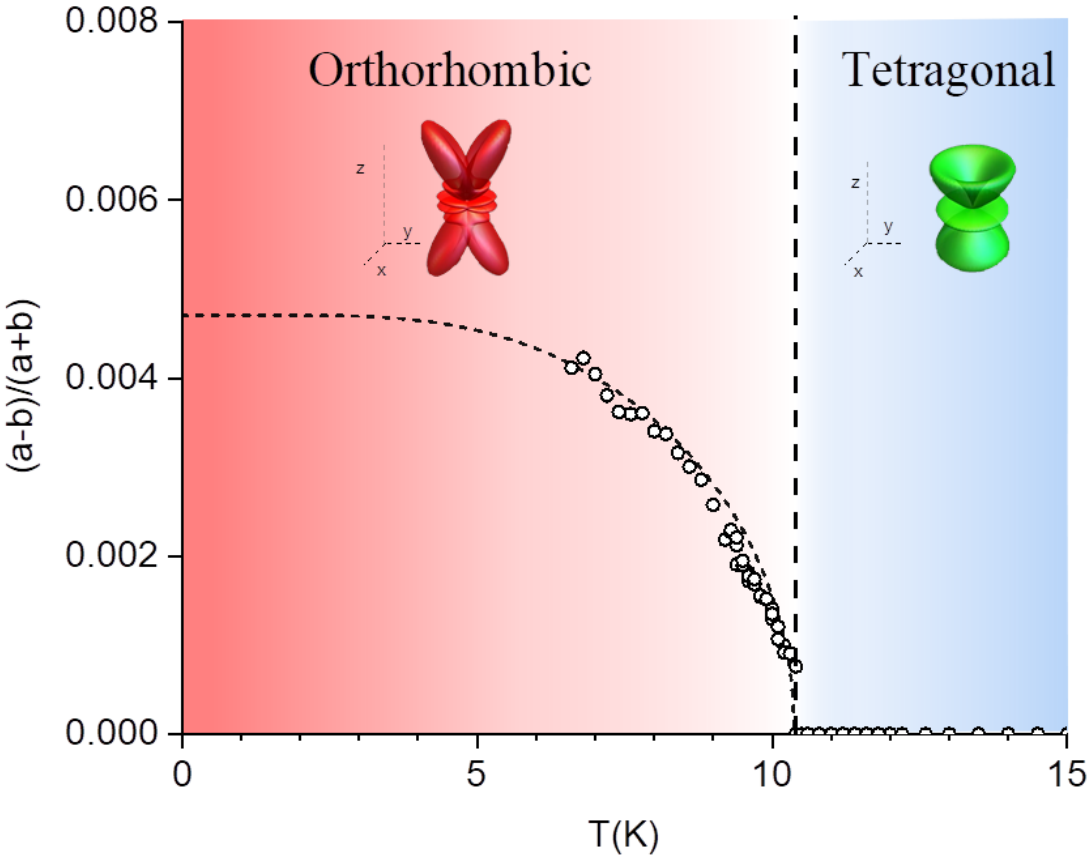

Figure 3.3: **Orthorhombicity of $YbRu_2Ge_2$** The order parameter of the orthorhombic structural phase transition is plotted against temperature. A mean-field Ising order parameter that becomes finite is 10.2K is overlaid as a guide to the eye. Insets illustrate the charge density of the $4f$ CEF quasi-quartet groundstate of $YbRu_2Ge_2$ in the tetragonal phase (green, with 4-fold symmetry), and that of the orthorhombic phase (red, with two-fold symmetry) . Ferroquadrupole order of the $4f$ orbitals is inferred from the observed orthorhombicity.

possibilities (corresponding to either B_{1g} or B_{2g} symmetry), these measurements detemine that the ferroquadrupolar state has a B_{1g} symmetry.

The temperature dependence of the in-plane resistivity of unstrained (i.e. free-standing) $YbRu_2Ge_2$ is shown in Figure 3.4. The data are consistent with previously published measurements, revealing a Kondo-like rise below 50 K and sharp features (seen more clearly in the derivative $\frac{d\rho}{dT}$) signifying the ferroquadrupole and magnetic phase transitions. Similar measurements of the non-magnetic, iso-structural, iso-electronic analog, YRu_2Ge_2, also shown in Figure 3.4, reveal a considerably smaller in-plane resistivity, and no signatures of any phase transitions. Since the band structure of the two materials is presumably quite similar, the large difference in the resistivity can be attributed to scattering from the local $4f$ orbitals in $YbRu_2Ge_2$. Significantly, since the resistivity of $YbRu_2Ge_2$

in the temperature window above T_Q (blue shading in Figure 3.4) is dominated by $4f$ scattering, the elastoresistivity (described below) can be directly related to the quadrupole strain susceptibility in the same symmetry channels, as described previously.

Elastoresistivity measurements were performed for multiple samples. Responses in the B_{1g} and B_{2g} symmetry channels were always found to be linear. Representative data for both of these symmetry channels (taken for samples of equal dimensions) are shown in Figure 3.5 as a function of temperature. Elastoresistivity data for the A_{1g} symmetry channel were also recorded during these measurements; while these data do not correspond to a susceptibility of a symmetry breaking quadrupole order, the measurements are presented in Section 3.6.7 for completeness. The response in the B_{1g} channel was found to be considerably larger than that in the B_{2g} channel. If the proportionality constants relating the resistivity anisotropy to the local quadrupole moment (see Section 3.6.5) are similar for the two symmetry channels, which would be the case for an isotropic Fermi surface but is certainly not guaranteed by symmetry, then the observed large anisotropy in the elastoresistivity would imply that the magneto-elastic coupling coefficient B_i for $i = B_{1g}$ is significantly larger than that for the B_{2g} symmetry channel. This would certainly be consistent with the observed B_{1g} symmetry of the orthorhombic distortion, but needs to be verified by other thermodynamic measurements. The B_{1g} and B_{2g} elastoresistivity coefficients were also measured for YRu_2Ge_2. No significant temperature dependence for either channel was found within experimental error, as anticipated given the absence of partially filled $4f$ orbitals in this compound.

Since the resistivity of $YbRu_2Ge_2$ in this temperature range is dominated by scattering from $4f$ orbitals (Figure 3.4), the temperature dependence of the elastoresistivity provides a good measure of the temperature dependence of the quadrupole strain susceptibility. Motivated by the previous discussion, the B_{1g} elastoresistivity was fit to a Curie-Weiss functional form:

$$\chi^{fit}_{B_{1g}} = -\frac{448.6 \pm 1.2}{T - 0.11 \pm 0.03} + 4.48 \pm 0.02 \tag{3.7}$$

The quality of fit over the full temperature range, right down to T_Q, (Figure 3.5 and inset to Figure 3.5), indicates that the splitting Δ_{CEF_1} of the quasi-quartet in the tetragonal state is less than T_Q in magnitude, consistent with previous estimates from inelastic neutron scattering [35]. Significantly, with reference to Equation 3.2, since the Weiss temperature is found to be close to 0K, it is clear that quadrupolar interactions mediated by the conduction electrons do not play an important role in the eventual ferroquadrupole phase transition. In other words, referring back to Equation 3.4 and the Levy criterion, we find that $B_i^2/C_i >> K_i$ for $YbRu_2Ge_2$ in the B_{1g} symmetry channel, and hence deduce that the ferroquadrupole transition must be driven primarily by magneto-elastic coupling in this material.

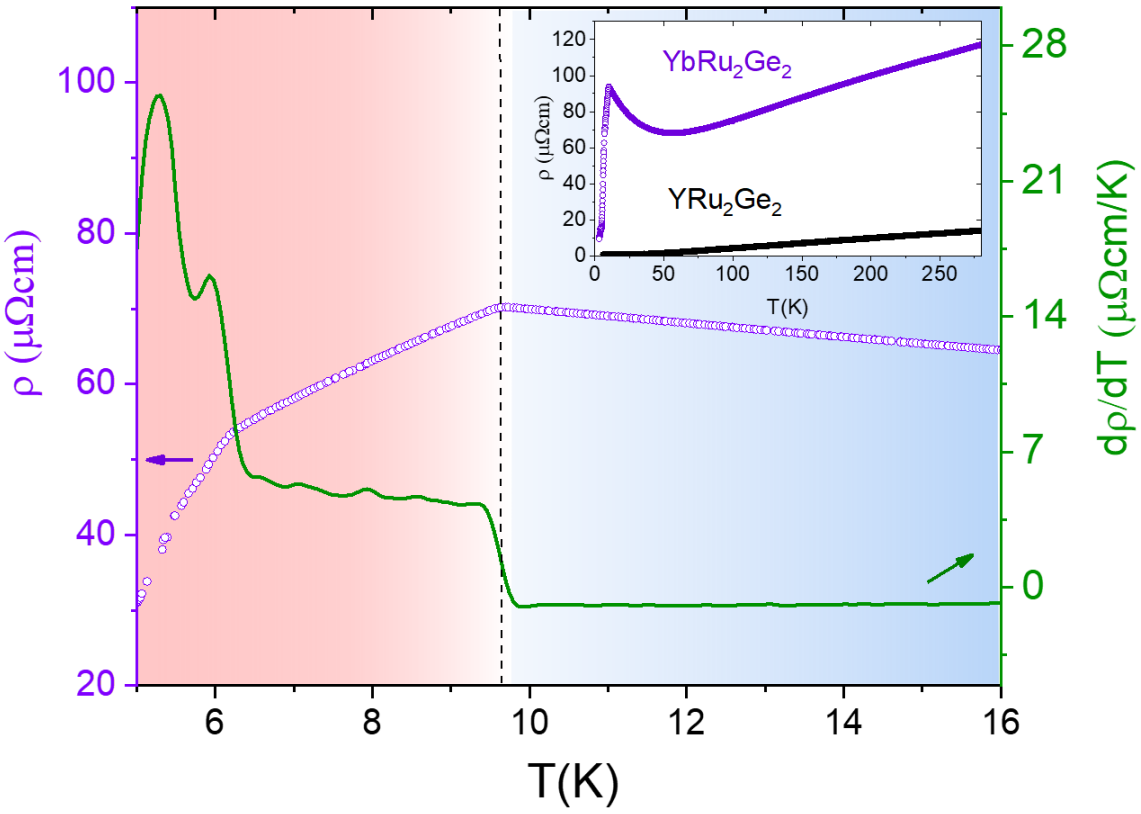

Figure 3.4: **Temperature dependence of the resistivity of $YbRu_2Ge_2$.** The resistivity (purple data points) and its derivative with respect to temperature (green data points) show clear features at T_Q (marked by vertical dashed line), as well as T_{N1} and T_{N2}. Slight differences in estimates of the critical temperatures relative to values extracted from x-ray diffraction measurements are attributed to differences in sweep rates of the two measurements. Inset shows the resistivity over a larger temperature range, in which a different $YbRu_2Ge_2$ single crystal is measured. Data are also shown for the non-magnetic analog, YRu_2Ge_2, for which no phase transitions are observed. Yttrium has an empty $4f$ shell but otherwise the electronic structure of the two materials is anticipated to be very similar, and differences in the resistivity between the two compounds are primarily attributed to $4f$ scattering.

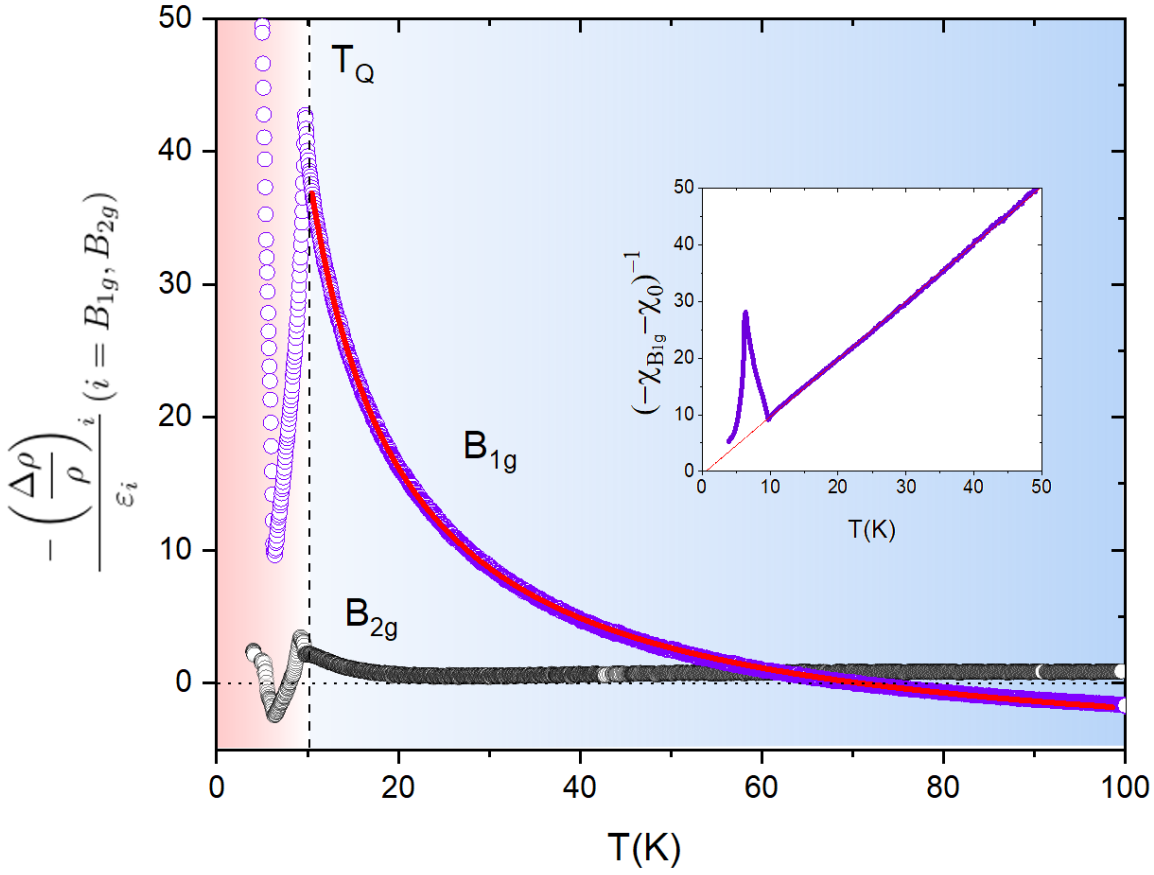

Figure 3.5: **Temperature dependence of the elastoresistivity of $YbRu_2Ge_2$ in the B_{1g} and B_{2g} symmetry channels.** As described in the main text, these quantities (shown by blue and black data points respectively) are proportional to the quadrupole strain susceptibility of the same symmetry channels. Inset shows the inverse of the quadrupole strain susceptibility $(-\chi_{B_{1g}} - \chi_0)^{-1}$ for the B_{1g} channel having subtracted a temperature-independent offset $\chi_0 = 4.48$. Red lines in the main panel and inset show fit to a Curie-Weiss functional form, with fit parameters described in the main text. The Weiss temperature is found to be 0 K within experimental error. Vertical dashed lines indicate T_Q, separating tetragonal (blue) from orthorhombic (red) phases.

3.5 Summary and Discussion

$YbRu_2Ge_2$ is a counterpoint to underdoped Fe-based superconductors, such as $BaFe_2As_2$, in terms of how the nematic phase transition is driven. Numerous measurements, including elastoresistivity [37, 41, 42, 40, 43, 44], elastic moduli [48, 1], Raman scattering [49, 50, 51, 52] and NMR [53, 54], have shown that the nematic susceptibility of $BaFe_2As_2$ and its analogs follow a Curie-Weiss functional form, with a Weiss temperature that is only slightly lower than the critical temperature for the coupled nematic/structural phase transition. Thus, while nematic-elastic coupling is still a necessary factor in driving the structural phase transition in those materials, the critical temperature is predominantly determined by electronic coupling between the nematic degrees of freedom [2]. In contrast, $YbRu_2Ge_2$ presents a case in which magneto-elastic coupling is the dominant driving force for the phase transition. Even so, the material is clearly nematic: a separate degree of freedom (the local $4f$ quadrupole moment) that couples bi-linearly to elastic strain with the same symmetry is evident from the temperature dependence of the quadrupole strain susceptibility, and its divergence drives a pseudo-proper ferroelastic phase transition. The lattice provides the effective coupling between the local quadrupole moments, but does not itself harbor any tendency towards a structural instability, as demonstrated by the absence of a comparable phase transition in the non-magnetic analog YRu_2Ge_2.

The significance of the present observation is twofold. First, we have shown that elastoresistance measurements can be used to probe the nematic susceptibility (quadrupole strain susceptibility) for local $4f$ systems, at least in this specific case of $YbRu_2Ge_2$. This provides a new avenue to characterize a critically important characteristic of intermetallic quadrupolar systems. Since the quadrupole strain susceptibility can, at least in principle, be large in several symmetry channels, we adopted a new methodology of micro-structuring the crystal using a FIB to guarantee symmetry decomposition of the resulting elastoresistivity. Second, we have established $YbRu_2Ge_2$ as a model system to explore effects of nematicity in metals. These ideas and measurements can be extended in this system, for example probing nematicity proximate to a putative quantum phase transition if the ferroquadrupole order were to be suppressed towards zero temperature. Methods of suppressing ferroquadrupole order using doping, magnetic field, or transverse strain [31] are readily experimentally accessible.

3.6 Supporting Information (SI)

3.6.1 CEF splitting of the J=7/2 Hund's rule multiplet of $YbRu_2Ge_2$

The Hund's rule groundstate multiplet of the Yb^{3+} ion, which is characterized by a total angular momentum number J=7/2, is split by the crystal electric field (CEF) according to the effective

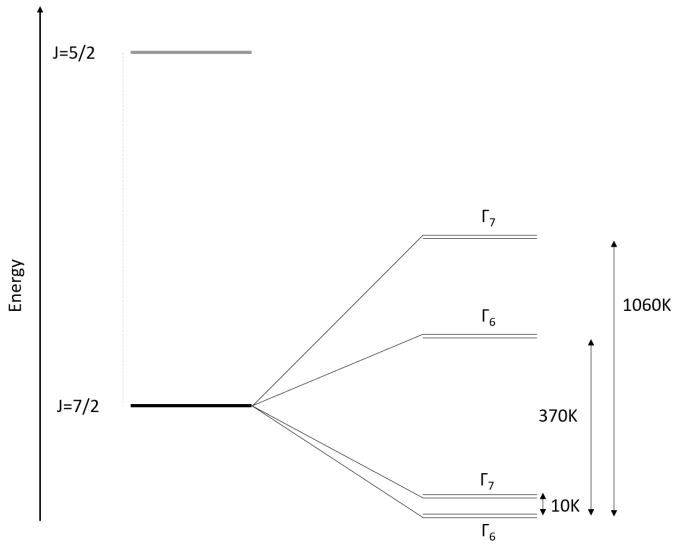

Figure 3.6: **$YbRu_2Ge_2$ CEF spectrum** Spin-orbit coupling determines the ground state electronic mulitplet to have J=7/2, which is split by the surrounding crystalline potential to have 4 doublets, the lowest two in energy forming a quasi-quartet split by roughly 10K.

Hamiltonian:

$$H_{CEF} = B_2^0 O_2^0 + B_4^0 O_4^0 + B_4^2 O_4^4 + B_6^0 O_6^0 + B_6^4 O_6^4 \tag{3.8}$$

Where O_l^m are the conventional Steven's operators [2] and B_l^m are coefficients to be determined. The resulting energy spectrum comprises 4 Kramers doublets (two doublets with Γ_6 symmetry, and two doublets with Γ_7 symmetry) and has been characterized by a combination of inelastic neutron scattering [35] and thermodynamic probes [4]. The tentative spectrum of states proposed by Jeevan in [46] is Γ_6 at 91meV, Γ_7 at 32 meV, Γ_7 at 0.9 meV, and Γ_6 at 0 meV (ground state), illustrated in Figure 3.6. This is the spectrum that we use to calculate the low-temperature quadrupole strain susceptibility, as described in the main text and below in Section 3.6.3.

3.6.2 X-ray diffraction data for $YbRu_2Ge_2$

Low temperature, high-resolution, X-ray diffraction measurements were performed on beamline A2 at CHESS (Cornell High Energy Synchrotron Source). Splitting of the (6 0 0) Bragg peak was observed below 10.2K, with the new peaks indicative of an orthorhombic structural distortion with a B_{1g} (x^2-y^2) symmetry, the associated domain structure of which results in 4 separate peaks along the (1 1 0) and (1 -1 0) directions [55]. Representative data are shown in Figures 3.7 and 3.8, taken at 12.2 K (above T_Q) and 6.6 K (below T_Q) respectively. A line cut along the (1 1 0) direction for both data sets is shown in Figure 3.9. The data in Figure 3.8 and 3.9 for $T < T_Q$

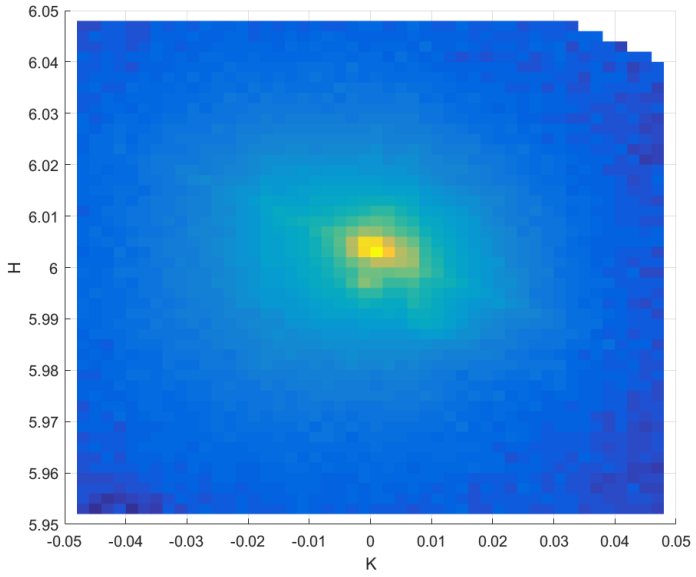

Figure 3.7: **Surface plot of log(intensity) at 12.2K** The material is still clearly tetragonal here, although it is displaying some spread in the momentum space direction that orthorhombic domains are expected, possibly indicating critical fluctuations or a static response to unintentional strains from securing the crystal to the sample holder.

reveal the persistence of the central tetragonal peak, albeit with a reduced intensity, implying that some part of the illuminated volume of the crystal remains in the tetragonal state upon cooling through T_Q. Since the phase transition is characterized via heat capacity measurements to be continuous [4], this observation implies heterogeneity of either the sample temperature or of the critical temperature T_Q. Thermodynamic and transport measurements indicate a maximum spread of critical temperatures of approximately 0.5 K but at least in principle local strains due to sample mounting for the measurement can plausibly affect the critical temperature leading to a larger variation. Additional measurements would be necessary to characterize how rapidly T_Q is affected by homogeneous strains of various symmetries in order to assess whether this is the origin of the effect. To best account for this when determining the orthorhombic order parameter (shown in Figure 3.3 of the main text), we obtained the position of the first moment of counts along the (1 1 0) direction (above a background threshold), that were clearly not part of the original tetragonal peak.

3.6.3 Quadrupole operators

The three relevant quadrupole operators, which correspond to the axis of the quadrupole oriented along [0 0 1] (z^2 symmetry), along [1 0 0] or [0 1 0] ($x^2 - y^2$ symmetry), and along [1 1 0] or [1 -1 0] (xy symmetry) respectively, are given by the familiar Steven's operators:

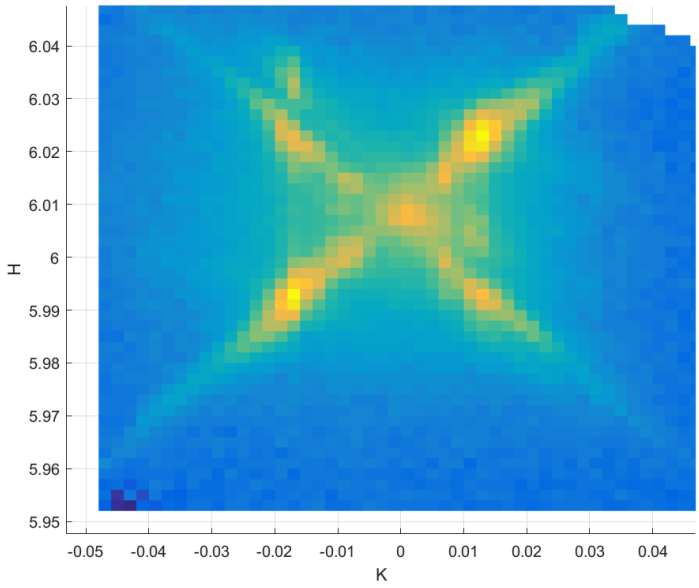

Figure 3.8: **Surface plot of log(intensity) at 6.6K** The material is clearly orthorhombic at this temperature, displaying multiple peaks.

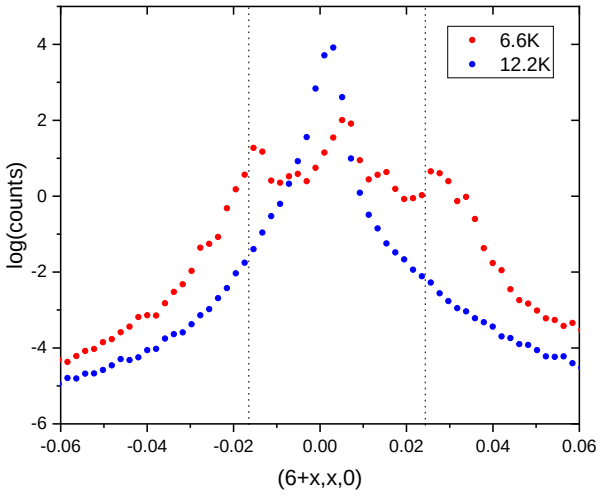

Figure 3.9: **Line cut of log(counts) along the (1,1,0) direction, centered at (6,0,0)** The dotted lines represent where the first moment of counts was determined to be, which was normalized by the lattice parameters to determine the orthrorhombic order parameter.

$$O_2^0 = 3J_z^2 - J(J+1) \tag{3.9}$$

$$O_2^2 = J_x^2 - J_y^2 = \frac{1}{2}(J_+^2 + J_-^2) \tag{3.10}$$

$$P_{xy} = \frac{1}{2}(J_xJ_y + J_yJ_x) = \frac{-i}{4}(J_+^2 - J_-^2) \tag{3.11}$$

In the restricted Hilbert space corresponding to the quasi-quartet CEF groundstate of $YbRu_2Ge_2$, these operators have the following matrix elements, where for convenience the basis of states is represented in the order (3/2, -1/2, -3/2, 1/2)

$$O_2^0 = \begin{bmatrix} -15 & 0 & 0 & 0 \\ 0 & -9 & 0 & 0 \\ 0 & 0 & -15 & 0 \\ 0 & 0 & 0 & -9 \end{bmatrix}$$

$$O_2^2 = \begin{bmatrix} 0 & 2\sqrt{15} & 0 & 0 \\ 2\sqrt{15} & 0 & 0 & 0 \\ 0 & 0 & 0 & 2\sqrt{15} \\ 0 & 0 & 2\sqrt{15} & 0 \end{bmatrix}$$

$$P_{xy} = \begin{bmatrix} 0 & -i\sqrt{15} & 0 & 0 \\ i\sqrt{15} & 0 & 0 & 0 \\ 0 & 0 & 0 & i\sqrt{15} \\ 0 & 0 & -i\sqrt{15} & 0 \end{bmatrix}$$

Noticing the correspondence to the Pauli spin matrices, we introduce for completeness a third, octupole, operator, that will also have finite matrix elements in this basis: $O_3^{-2} = \frac{-i}{4}(J_z(J_+^2 - J_-^2) + (J_+^2 - J_-^2)J_z)$

$$O_3^{-2} = \begin{bmatrix} 0 & -i\sqrt{15} & 0 & 0 \\ i\sqrt{15} & 0 & 0 & 0 \\ 0 & 0 & 0 & -i\sqrt{15} \\ 0 & 0 & i\sqrt{15} & 0 \end{bmatrix}$$

Inspection of these expressions reveals they can be written as tensor products of the canonical Pauli matrices and the identity, I:

$$O_0^2 = I \otimes (-3\sigma_z - 12I) \tag{3.12}$$

$$O_2^2 = I \otimes (2\sqrt{15}\sigma_x) \tag{3.13}$$

$$P_{xy} = \sigma_z \otimes (\sqrt{15}\sigma_y) \tag{3.14}$$

$$O_3^{-2} = I \otimes (\sqrt{15}\sigma_y) \tag{3.15}$$

With reference to the tensor product formula:

$$[I \otimes A, I \otimes B] = I \otimes [A, B] \tag{3.16}$$

and noting that constants don't affect commutation relations, the three operators O_2^0, O_2^2, and O_3^{-2} obey the canonical commutation relations. The quasi-quartet ground state can be thought of as two replicas of a pseudo-spin $\frac{1}{2}$ doublet, where the two replicas arise as a consequence of Kramer's theorem. These three operators will then serve as the effective spin operators in the three spatial dimensions of the pseudo-spin space. The quartet is split (by roughly $\Delta_0 = 10K$) due to the tetragonal point symmetry of the CEF, yielding a finite σ_z (i.e a finite O_2^0 quadrupole moment) above T_Q. Mixing of these eigenstates, as described in Figure 3.1 of the main text, can then yield finite quadrupole moments O_2^2 or P_{xy}.

3.6.4 Quadrupole-strain Susceptibility

Externally applied stresses cause finite strains, which in turn affect the eigenstates and eigenvalues of H_{CEF}, shifting and admixing the states described in Section 3.6. The magneto-elastic coupling (MEC) Hamiltonian is given by

$$H = H_{CEF} + \sum_{\Gamma_i} B_m^l \varepsilon_{\Gamma_i} Q_{\Gamma_i}$$

Where B_m^l are coefficients yet to be determined, and Γ_i are irreducible representations of the point group. Applying a non-zero stress which induces a strain ($\varepsilon_\gamma = \varepsilon_{xx} - \varepsilon_{yy}$) will induce a finite moment of $\langle O_2^2 \rangle$, which will perturbatively change the existing Hamiltonian (in the basis of the quasi-quartet) to be in the form:

$$H = H_{CEF} + B_2^2 \varepsilon_\gamma O_2^2 = I \otimes \begin{bmatrix} \Delta_0/2 & 2\sqrt{15}B_2^2\varepsilon_\gamma \\ 2\sqrt{15}B_2^2\varepsilon_\gamma & -\Delta_0/2 \end{bmatrix}$$

Diagonalizing this matrix gives a new energy gap of:

$$\Delta/2 = \sqrt{(\Delta_0/2)^2 + 60(B_2^2\varepsilon_\gamma)^2} \tag{3.17}$$

The thermal expectation value of the quadrupolar moment $\langle O_2^2 \rangle$ is now:

$$\langle O_2^2 \rangle = \frac{120 B_2^2 \varepsilon_\gamma}{\Delta} \tanh\left(\frac{\Delta}{2T}\right) \tag{3.18}$$

Thus the quadrupole-strain susceptibility is:

$$\chi_{Q_{B_{1g}}} = \left.\frac{dQ_{B_{1g}}}{d\varepsilon_{B_{1g}}}\right|_{\varepsilon \to 0} = \frac{60 B_2^2}{T} \tag{3.19}$$

when $T >> \Delta_0$, and

$$\chi_{Q_{B_{1g}}} = \left.\frac{dQ_{B_{1g}}}{d\varepsilon_{B_{1g}}}\right|_{\varepsilon \to 0} = \frac{120 B_2^2}{\Delta_0} \tanh\left(\frac{\Delta_0}{2T}\right) \tag{3.20}$$

in general.

Although in the case of the B_{2g} order parameter P_{xy} the Hamiltonian cannot be written as concisely, a similar result is still obtained:

$$\chi_{Q_{B_{2g}}} = \left.\frac{dQ_{B_{2g}}}{d\varepsilon_{B_{2g}}}\right|_{\varepsilon \to 0} = \frac{15 B_{xy}}{T} \tag{3.21}$$

when $T >> \Delta_0$, and

$$\chi_{Q_{B_{2g}}} = \left.\frac{dQ_{B_{2g}}}{d\varepsilon_{B_{2g}}}\right|_{\varepsilon \to 0} = \frac{30 B_{xy}}{\Delta_0} \tanh\left(\frac{\Delta_0}{2T}\right) \tag{3.22}$$

in general.

Hence both the B_{1g} and B_{2g} quadrupole strain susceptilities can be put in the form:

$$\chi_{Q_{\Gamma_i}} = \left.\frac{dQ_{\Gamma_i}}{d\varepsilon_{\Gamma_i}}\right|_{\varepsilon \to 0} = \frac{2\langle Q_{\Gamma_i}\rangle_o^2 B_{\Gamma_i}}{\Delta_0} \tanh\left(\frac{\Delta_0}{2T}\right) \tag{3.23}$$

Assuming no B_{1g} or B_{2g} strain is being applied, the A_{1g} quadrupole-strain susceptibility is:

$$\chi_{Q_{A_{1g}}} = \left.\frac{dQ_{A_{1g}}}{d\varepsilon_{A_{1g}}}\right|_{\varepsilon \to 0} = \frac{\langle Q_{A_{1g}}\rangle_o^2 (B_2^0)_1 sech^2\left(\frac{\Delta_0}{2T}\right)}{T} \tag{3.24}$$

Where $\langle Q_{A_{1g}}\rangle_o = 3$

Adding in mean-field interactions of the form $H_{QQ} = K_{\Gamma_i}\langle Q_{\Gamma_i}\rangle Q_{\Gamma_i}$ will renormalize the quadrupole-strain susceptibilities to be in the form:

$$\chi_{Q_{\Gamma_i}} = \left.\frac{dQ_{\Gamma_i}}{d\varepsilon_{\Gamma_i}}\right|_{\varepsilon \to 0} = \frac{2B_{\Gamma_i}\langle Q_{\Gamma_i}\rangle_o^2 \tanh\left(\frac{\Delta_0}{2T}\right)}{\Delta_0 - 2K_{\Gamma_i}\langle Q_{\Gamma_i}\rangle_o^2 \tanh\left(\frac{\Delta_0}{2T}\right)} \tag{3.25}$$

For $T >> \Delta/2$ this becomes the familiar expression:

$$\chi_{Q_{\Gamma_i}} = \frac{B_{\Gamma_i}\langle Q_{\Gamma_i}\rangle_o^2}{T - \langle Q_{\Gamma_i}\rangle_o^2 K_{\Gamma_i}} \tag{3.26}$$

For A_{1g} this renormalizes it to become:

$$\chi_{A1g} = \frac{B_0^2\langle Q_2^0\rangle_o^2 sech^2\big(\beta\big(\Delta/2 + 3K_2^0\langle O_2^0\rangle|_{\varepsilon=0}\big)\big)}{T - \langle Q_2^0\rangle_o^2 K_2^0 sech^2\big(\beta\big(\Delta/2 + 3K_2^0\langle O_2^0\rangle_{\varepsilon=0}\big)\big)} \tag{3.27}$$

The proposed CEF quasi-quartet states [46] can be substituted in to find the actual values : $\langle Q_i\rangle_o$: $\langle O_2^0\rangle_o = 3.035$, $\langle O_2^2\rangle_o = 8.3185$, and $\langle P_{xy}\rangle_o = 3.4660$

With these values the elastoresistivity measurements can be fit to to obtain absolute values for K_i and the gap Δ and relative ratios of B_i.

3.6.5 Relation of Elastoresistivity to Quadrupole-strain Susceptibility

To show how the proportionality between the quadrupole-strain susceptibilities and the elastoresistivity coefficients is obtained, we follow Friederich and Fert [39] and extend their argument to tetragonal systems, replacing the magnetic field with strain as the source of the quadrupole moment. If we make the following assumptions that: a) the strain is perturbative, hence the quadrupole moments can be treated as impurities but the system has a infinitesimal overall quadrupole moment; b) The scattering is dominated by isotropic (in the ab plane) elastic scattering potentials $V\delta(r_i)$ at each Yb site i; c) We can use the first Born approximation to obtain the scattering rate $W_{kk'}$; and d) The conduction electrons are primarily s-wave and p-wave in character, then we can follow the argument laid out in Ref. [39].

We begin by writing down the scattering interaction between s and p wave conduction electrons and $4f$ sites originally derived by Kondo:

$$V_{scatt} = \sum_{kk'}\left[V - \frac{D}{k_f^2}\left((J\cdot k)(J\cdot k') - \frac{J(J+1)}{3}k\cdot k'\right)\right]a_{k'}^{\dagger}a_k' \tag{3.28}$$

Where D is the coefficient of the quadrupolar scattering potential from the $4f$ electrons, and V in the sum is the previously mentioned strength of the isotropic scattering potential. When this potential is plugged into Fermi's Golden rule, assuming the quadrupole term is perturbatively small, the anisotropic cross terms lead to a resistivity ratio directly from Ref. [39], Equation 3:

$$\frac{\rho_i^Q}{\rho_0} = \frac{2D}{3V}\left(\langle J_i^2\rangle - \frac{J(J+1)}{3}\right) \tag{3.29}$$

Where i is the direction of the current, and ρ_0 is the resistivity due to the isotropic scattering potential (isotropic only in the ab plane in the case of $YbRu_2Ge_2$)

Thus:

$$\frac{\rho_x^Q - \rho_y^Q}{2\rho_0} = \frac{D}{3V}\left(\langle J_x^2\rangle - \langle J_y^2\rangle\right) = \frac{D}{3V}\langle O_2^2\rangle \tag{3.30}$$

Because inelastic scattering should only be dependent on the magnitude of the gap and matrix elements like $\langle|Q_i|\rangle^2$, its B_{1g} component induced by strain should be close to zero. Similarly the anisotropic part of the Kondo scattering should be close to zero, as there is no reason to suggest there are quadrupolar aspects of the coupling of conduction electrons to the magnetic aspects of the $4f$ sites. Thus, taking the appropriate strain derivatives (in this case, with respect to $\varepsilon_{xx} - \varepsilon_{yy}$), we find that the elastoresistivity associated with scattering from the $4f$ orbital is directly proportional (with a temperature independent proportionality coefficient) to the B_{1g} quadrupole-strain susceptibility.

$$\left.\frac{\frac{\partial(\rho_{4f}^{xx} - \rho_{4f}^{yy})}{\rho_{4f}^0}}{\partial\varepsilon_{B1g}}\right|_{\varepsilon\to 0} \approx \frac{D}{3V}\frac{\partial\langle O_2^2\rangle}{\partial\varepsilon_{B1g}} \propto \chi_{B1g} \tag{3.31}$$

Several scattering processes contribute to the resistivity of $YbRu_2Ge_2$. Assuming validity of Matthiessen's rule, $\rho_{YbRu2Ge2} = \rho_{imp} + \rho_{e-ph} + \rho_{e-e} + \rho_{4f}$ where ρ_{imp} arises from impurity scattering, ρ_{e-ph} from electron-phonon interactions, ρ_{e-e} from electron-electron scattering, and ρ_{4f} is defined above. At least in principle, each of these terms can have an associated elastoresistivity; the expression derived in Eq. 24 above relates only to the $4f$ part. Contributions to the resistivity and elastoresistivity arising from ρ_{imp}, ρ_{e-ph} and ρ_{e-e} can be subtracted by considering a non-magnetic analog that has the same crystal structure, the same band structure and a similar impurity concentration. YRu_2Ge_2 (note that Y = Yttrium, different to Ytterbium Yb) potentially provides such a non-magnetic analog. Such a subtraction would then yield,

$$\frac{\frac{\partial(\rho_{4f}^{xx} - \rho_{4f}^{yy})}{\rho_{4f}^0}}{\partial\varepsilon_{B1g}} \approx \frac{\frac{\partial(\rho_{YbRu_2Ge_2}^{xx} - \rho_{YbRu_2Ge_2}^{yy})}{\rho_{YbRu_2Ge_2}^0 - \rho_{YRu_2Ge_2}^0} - \frac{\partial(\rho_{YRu_2Ge_2}^{xx} - \rho_{YRu_2Ge_2}^{yy})}{\rho_{YbRu_2Ge_2}^0 - \rho_{YRu_2Ge_2}^0}}{\partial\varepsilon_{B1g}} \tag{3.32}$$

where superscripts '0' refer to zero strain conditions.

The unstrained resistivity of YRu_2Ge_2, $\rho_{YRu2Ge2}^0$, is found to be almost an order of magnitude smaller than that of $YbRu_2Ge_2$ (see Figure 3.3 in the main text). Furthermore, normal metals far from any electronic instabilities, typically exhibit very small elastoresistivities. Hence, we can safely make the approximation that:

$$\frac{\frac{\partial(\rho_{4f}^{xx} - \rho_{4f}^{yy})}{\rho_{4f}^0}}{\partial\varepsilon_{B1g}} \approx \frac{\frac{\partial(\rho_{YbRu_2Ge_2}^{xx} - \rho_{YbRu_2Ge_2}^{yy})}{\rho_{YbRu_2Ge_2}^0}}{\partial\varepsilon_{B1g}} \propto \chi_{B1g} \tag{3.33}$$

Hence elastoresistivity will be a direct measure of the quadrupole-strain susceptibility given these conditions.

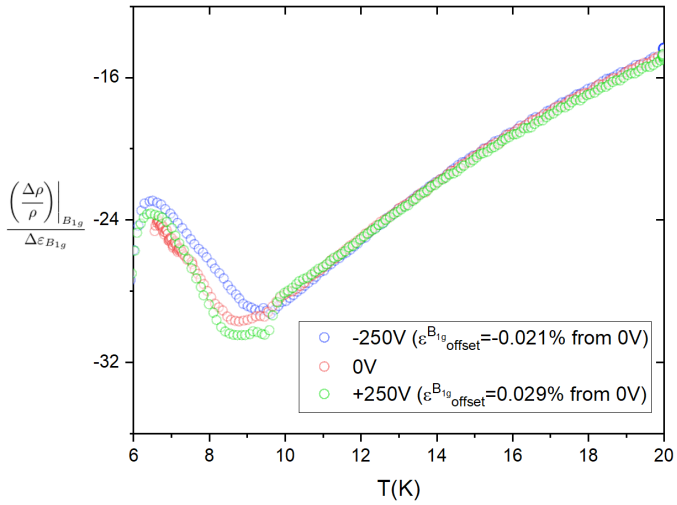

Figure 3.10: **Strain dependence of the B_{1g} elastoresistivity response** The B_{1g} quadrupole-strain susceptibility displays little sensitivity to tuning B_{1g} offset strains above the quadrupolar phase transition indicating this channel is dominated by linear behavior, and hence $\left(\frac{\Delta\rho}{\rho}\right)_{B_{1g}}/\Delta\varepsilon_{B_{1g}}$ provides a good measure of the linear elastoresistivity coefficients for this symmetry channel, m_{11}-m_{12}

3.6.6 Linearity of the B_{1g} elastoresistivity

An effective way to show that the elastoresistivity is linear in strain while using the AC technique that we describe in the main text is to perform these measurements for a variety of offset bias strains. In Figure 3.10 we show data for the B_{1g} response for measurements performed with an AC amplitude corresponding to a peak-to-peak voltage applied to the PZT stack of 40 volts, with a simultaneous DC bias voltage of 0V, -250V and + 250V in the temperature range from 6 to 20 K. Over this temperature range, these offset voltages correspond to DC strain offsets (relative to 0V) of approximately 0, -0.021%, and 0.029% . As can be seen by inspecting the figures, in the temperature range above T_Q, the data almost perfectly line up, demonstrating the absence of any significant non-linear response.

3.6.7 Non-linearity of the A_{1g} elastoresistivity

In contrast to the case of B_{1g} response, the in-plane A_{1g} response $\frac{\rho_{xx}+\rho_{yy}}{\rho_0}$ exhibited a striking non-linearity. Figure 3.11 shows the response for measurements performed with an AC amplitude corresponding to a peak-to-peak voltage applied to the PZT stack of 40 volts, with a simultaneous DC bias voltage of 0V, -250V and + 250V in the temperature range from 6 to 20 K. Over this temperature range, these offset voltages correspond to DC strain offsets (relative to 0V) of approximately 0, -0.021%, and 0.029% . The sample was oriented on the PZT stack such that the crystal experienced

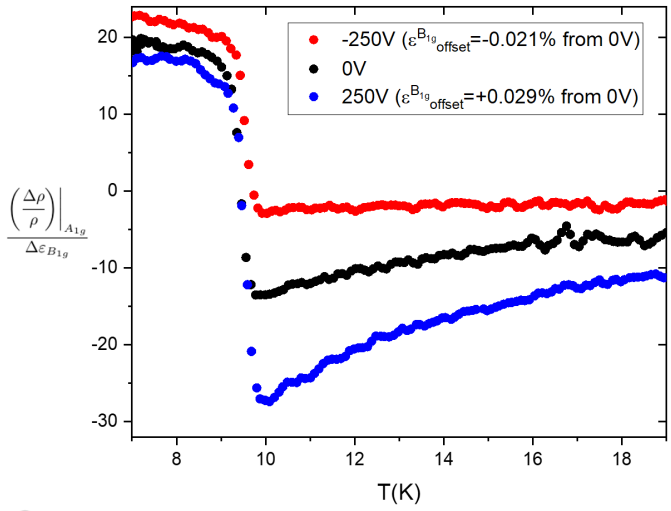

Figure 3.11: **Non-linearity of the A_{1g} response with respect to B_{1g} strain.** The A_{1g} quadrupole-strain susceptibility displays striking sensitivity to tuning offset B_{1g} strains above the quadrupolar phase transition.

a combination of A_{1g} and B_{1g} strains for Figure 3.11 , and A_{1g} and B_{2g} strains for Figure 3.12. As can be seen, there is a striking difference between the measurements, indicating the presence of a substantial non-linear A_{1g} elastoresistivity in response to B_{1g} symmetry strains.

Although the A_{1g} response is not the main subject of this text, we outline below the origin of this effect, making particular reference to how this shows up in an AC measurement.

To second order in strain, a crystal that experiences both A_{1g} and B_{1g} symmetry strains can experience an A_{1g} elastoresistance response given by

$$\left(\frac{\Delta\rho}{\rho_0}\right)_{A_{1g}} = m^{A_{1g}}_{A_{1g}}\varepsilon_{A_{1g}} + m^{A_{1g},A_{1g}}_{A_{1g}}[\varepsilon_{A_{1g}}]^2 + m^{B_{1g},B_{1g}}_{A_{1g}}[\varepsilon_{B_{1g}}]^2 \tag{3.34}$$

Where we are following the notation used in Ref.[[43]]. The linear term proportional to $\varepsilon_{A_{1g}}$ is allowed by symmetry as well as quadratic terms proportional to $\varepsilon^2_{B_{1g}}$.

Since the AC Elastoresistivity method used for these measurements locks in to the response at the frequency ω at which the strain is applied, it is useful to write the strains out as a combination of DC offset strains (arising for example from thermal expansion mismatches and glue strains, as well as intentional bias strains as mentioned previously) and AC applied strains:

$$\varepsilon_i^{tot} = \varepsilon_i^{DC} + \varepsilon_i^{AC}\cos\omega t \tag{3.35}$$

Where i represents the symmetry channel and the amplitude of the AC term depends on the voltage waveform applied to the piezo. Substituting into Eq. 3.34 and focusing on the amplitude of

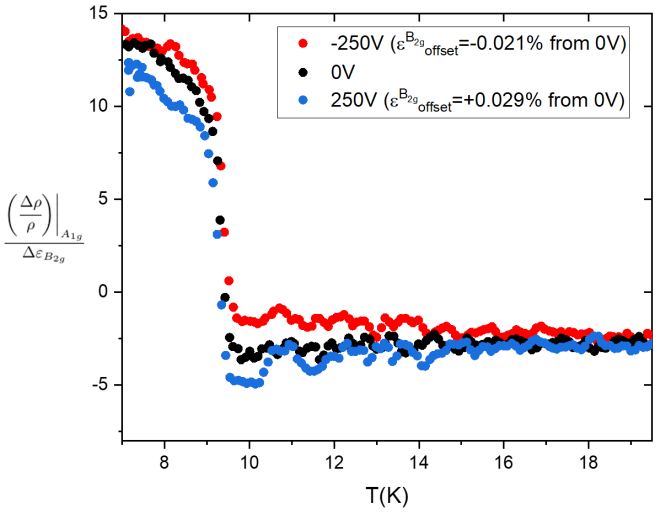

Figure 3.12: **Non-linearity of the A_{1g} response with respect to B_{2g} strain.** The A_{1g} quadrupole-strain susceptibility displays small sensitivity to tuning offset A_{1g} and B_{2g} strains above the quadrupolar phase transition

the signal that will be locked into at frequency ω:

$$(\frac{\Delta\rho}{\rho_0})^{AC}_{A_{1g}} = m^{A_{1g}}_{A_{1g}}\varepsilon^{AC}_{A_{1g}} + 2m^{A_{1g},A_{1g}}_{A_{1g}}\varepsilon^{DC}_{A_{1g}}\varepsilon^{AC}_{A_{1g}} + 2m^{B_{1g},B_{1g}}_{A_{1g}}\varepsilon^{DC}_{B_{1g}}\varepsilon^{AC}_{B_{1g}} \tag{3.36}$$

Thus we can expect both a linear and non-linear contribution to the signal, with the strength of the non-linear part determined by both the amount of offset strain and the quadratic coefficient of that channel.

A similar difference in non-linear elastoresistivity coefficients was recently observed for the underdoped Fe-based superconductor, $Ba(Fe_{0.975}Co_{0.025})_2As_2$ [43]. In that material, the nematic transition occurs in the B_{2g} symmetry channel and the quantity $m^{B_{2g},B_{2g}}_{A_{1g}}$ exhibits a divergence. In the present case, $YbRu_2Ge_2$ undergoes a nematic transition in the B_{1g} symmetry channel, and the quantity $m^{B_{1g},B_{1g}}_{A_{1g}}$ appears to grow very large. Both results highlight the role played by nematic (quadrupole) fluctuations in affecting the isotropic properties of materials . In the case of $YbRu_2Ge_2$, the observation of a large $m^{B_{1g},B_{1g}}_{A_{1g}}$ adds further evidence to our conclusion that the quadrupole-strain susceptibility is large in the B_{1g} channel but small in the B_{2g} channel.

3.6.8 Focused Ion Beam parameters

The instrument used to etch the samples was an FEI Helios NanoLab 600i DualBeam FIB/SEM, containing both a focused Ga+ ion beam ("Tomahawk") and a high resolution field emission scanning electron ("Elstar") column. Combined with advances in patterning, scripting, and a suite of

accessories, these features make milling, imaging, analysis, and sample preparation down to the nanoscale possible.

A 65 nA ion current was used to etch through the samples. Gallium implantation is expected to affect a depth of less than 100 nm from the surface roughly, which is inconsequential for the bulk resistivity measurements that were performed.

3.6.9 Crystal Growth

Single crystals of $YbRu_2Ge_2$ were grown using an unseeded flux method, with Indium being the flux and the other precursors added in stoichiometrically. The flux ratio was varied from 96-98%, with 97.5% found to produce both the largest size individual crystals and also the greatest yield. To help ensure inclusion of the high-melting point Ru into the melt, the elemental Ru and Ge precursors were arc-melted in a mono-arc furnace. The elements were then combined into an alumina crucible, which was sealed inside a Ta crucible to prevent oxidation and to contain the flux. The crucibles were heated to a max temperature of 1450°C for 6-12 hours, and then cooled to 1200°C at approximately 4K/hour. The alumina crucibles were then sealed quartz and spun in a centrifuge at 400°C to remove the Indium flux from the crystals The resulting crystals were etched in HCl acid for several months until they were easily cleaveable.

Chapter 4

Effect of magnetic field on Ferroquadrupolar Order in $YbRu_2Ge_2$

4.1 Abstract

The measurements shown in Chapter 3 suggest that $YbRu_2Ge_2$ undergoes a B_{1g} ferroquadrupolar phase transition at 10.2K, and exhibits a divergence of the associated quadrupole-strain susceptibility as inferred from elastoresistivity measurements. Applying a magnetic field along the c-axis of this material is expected to suppress this transition (see section 1.6.5), potentially inducing a quantum phase transition. This picture is, however, complicated by the multiple degeneracies of the ground-state quasi-quartet, which have magnetic degrees of freedom that manifest in antiferromagnetic phase transitions at lower temperatures (6.3K and 5.6K at zero magnetic field). Additionally the $4f$ ground state of $YbRu_2Ge_2$ can potentially exhibit local octupolar moments, which can be induced by the application of suitable combinations of magnetic field and strain. This motivates the investigation of the H-T phase diagram and associated field-induced properties of this material on two grounds; first to understand the evolution of these multipolar moments, and second to explore the interplay between the metallic degrees of freedom and the potentially quantum critical 4f sublattice. Here we use a combination of resistivity measurements and elastoresistivity measurements performed in high magnetic fields that shed light on both of those aspects. Measurements in fields up to 14T were performed at Stanford University. Measurements in fields up to 35T were performed at the NHMFL in Tallahassee, Florida.

4.2 Introduction

As discussed previously (see section 1.6.3), a magnetic field acts as a transverse field for ferroquadrupole order in a simple non-Kramer's doublet, ultimately inducing a quantum phase transition [31]. This appears to be the case for $TmAg_2$ [31]. While it is manifestly clear that sufficiently high magnetic fields will eventually suppress the ferroquadrupole order in $YbRu_2Ge_2$ simply by virtue of splitting and polarizing the crystal field groundstate, nevertheless this system is considerably more complicated than $TmAg_2$. These complications, outlined below, lead to an additional richness in the resultant behavior of the system.

As discussed previously (see Section 3.2), $YbRu_2Ge_2$ has a tetragonal crystal structure at room temperature. The $4f$ electrons of the trivalent Yb ion form local multiplets, and spin-orbit coupling determines the lowest energy manifold to have total angular momentum quantum number $J = 7/2$. The CEF for the tetragonal point group symmetry results in four Kramers doublets. Analysis of heat capacity, magnetic susceptibility, and inelastic neutron-scattering measurements indicate that the CEF ground state is a quasi-quartet comprising two doublets split by a small energy $\Delta_o < 10K$. The quasi-quartet is split by approximately 300 K from the other two higher-energy doublets [4].

A magnetic field applied along the c-axis will split the 4 states of the quasi-quartet (in the ordered state it will split each quadrupolar doublet), and at high magnetic fields a large enough gap will be induced between the states such that the spontaneous ferroquadrupole order will be totally suppressed (see discussion in section 1.6.5 and schematic diagram in Figure 4.1(b)). For magnetic fields close to and below the critical field, H_c, the phase transition will still map onto the phase transition featured in the spin 1/2 transverse field Ising model, with magnetic field acting as a transverse field and the quadrupolar interactions acting as the longitudinal field. This is because as the temperature approaches 0K, only two states will be relevant, for which there is a precise mapping to a spin 1/2 doublet. Thus we might expect a quantum phase transition at 0K and $H_z = H_c$, however this makes two assumptions. First, that the extra magnetic degrees of freedom of the quasi-quartet don't intervene via another magnetically ordered phase; and second that the metallic degrees of freedom don't couple strongly enough to the $4f$ sublattice to fundamentally change the low-temperature phase diagram of the coupled system.

In addition to the issues raised above, the degrees of freedom of the ground-state quasi-quartet can allow additional higher-order multipole moments to exist, namely octupoles. These octupoles will be magnetic (as the crystal is centro-symmetric), and can be represented by the third-order Stevens operators O_3^m where m = -3 to 3. For instance the B_{2g}^- octupole (- denotes trs. breaking) $O_3^2 = \frac{1}{2}(O_2^2 J_z + J_z O_2^2)$, will have matrix elements between the same states as O_2^2, just with an alternating sign that depends on the sign of the m_j states. This octupole will couple "bilinearly" to the two-component conjugate field of $H_z \varepsilon_{B_{1g}}$, which becomes relevant in the orthorhombic phase with applied magnetic field. The evolution of this octupole moment with magnetic field, as well as its potential consequences for the thermodynamic properties of this material, provide additional

reasons to experimentally investigate $YbRu_2Ge_2$ by applying magnetic field along the c-axis.

All of the above points motivate experimentally determining this H-T phase diagram, as well as investigating thermodynamic and transport properties in the proximity of the critical field $H_z = H_c$. In this chapter we use a combination of resistivity and elastoresistivity measurements to provide insight to the properties as the ferroquadrupolar phase transition is progressively suppressed by magnetic field oriented along the c-axis.

4.3 Experimental Methods

Single crystals were grown following the methods described in Section 2.1.2, and were oriented using single crystal X-ray diffraction. Samples were cleaved and cut to be of dimensions approximately 1mm x 0.4mm x 0.03mm, and gold wires were contacted to the samples via H-20E silver epoxy in the standard 4 point geometry. Resistivity measurements were performed in a He3 probe using a 35T resistive magnet at the National High Magnetic Field Laboratory in Tallahasse, Florida, and temperatures down to 0.35K were accessible. Measurements were made as a function of temperature in fixed field oriented along the c-axis of the samples (RvT), and as a function of field at a fixed temperature (RvH).

AC elastoresistivity measurements were performed as described in Section 2.2.2. The contacts were arranged in a modified Montgomery geometry, but because of the irregular shape of the crystal flakes a square pattern was microstructured into the sample as shown in Figure 2.2, precisely defining both the current paths and the voltage measurements, as well as their orientation relative to the crystal axes. This patterning also created an isotropic in-plane strain transmission ratio, due to the square shape of the microstructured sample. The samples were secured on 50μm thick Si substrates using Angstrom Bond (AB9110), which were then glued onto the surface of PICeramic piezoelectric stacks, also using Angstrom Bond. They were oriented such that (1 0 0) and (0 1 0) were parallel to the PZT edges, ensuring B_{1g} antisymmetric strain and in-plane symmetric strain A_{1g} would be applied. Strain gauges were used to measure the strain per voltage the stack was applying, and the strain transmission ratio of 50% was found for where the sample was glued. The stacks were oriented such that the (001) face of the crystal was perpendicular to the applied magnetic field. Fields up to 14T were used for these experiments.

4.4 Results

4.4.1 Phase diagram

As can be seen from the left panel of Figure 4.1, the ferroquadrupolar and magnetic phase transitions for $YbRu_2Ge_2$ are easily seen in the resistivity traces vs temperature, at least for fields below 20T, and the H-T phase diagram was extracted from signatures in $\frac{d\rho}{dT}$.

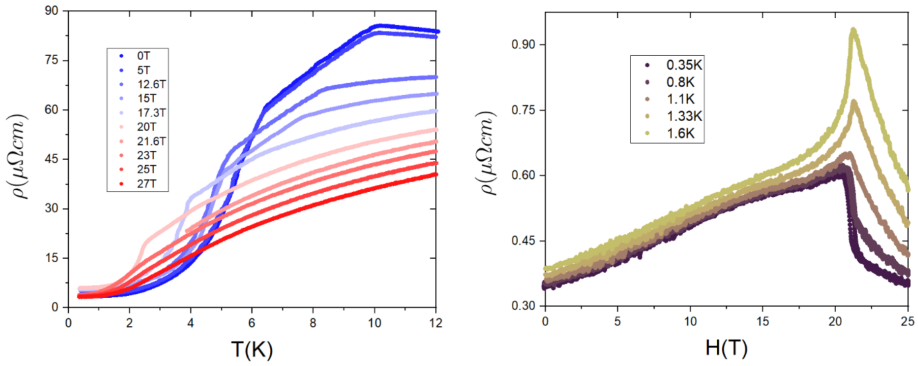

Figure 4.1: **Identification of critical temperatures of the ferroquadrupolar and magnetic phase transitions in $YbRu_2Ge_2$ from RvT and RvH measurements.** The left panel (a) displays the RvT traces obtained in magnetic fields from 0T to 27T spanning 0.35K to 12K. The color scale goes from blue to red with increasing magnetic field. The kinks at the ferroquadrupolar phase transitions can be seen easily for fields below 20T, smoothly being suppressed towards 0K. The steepness of the phase diagram prevents lower temperature ferroquadrupolar phase transitions from being easily observed in coarsely spaced RvT traces. The right panel (b) displays RvH traces at temperatures spaced from 0.35K to 1.6K. The phase transition at 21.3 ± 0.2 T is easily observed at 0.35K and 0.8K, but seems to be replaced by a prominent cusp at higher temperatures. At temperatures above 2K this cusp was no longer is seen as prominently however.

Resistivity traces were measured in fields from 0T to 30T from 0.35K to 12K, although some temperature regimes weren't available for certain magnetic fields. RvH traces were also collected at temperatures below 2K, allowing detailed insight into the low temperature transport dependence. Errors in transition temperatures arose from thermal gradients from probe to sample and the magnetoresistivity of the probe cernox thermometer, and are represented by the error bars in Figure 4.2. The ferroquadrupolar phase transition T_Q (blue circles in Figure 4.2), with $T_Q(0T) = 10.1K \pm 0.2K$ is suppressed to 0.35K at $H_c = 21.3 \pm 0.3T$. The data points below 0.8 K are inferred from kinks in RvH traces as seen in Figure 4.1(b), and the higher temperature points are extracted from signatures from $\frac{d\rho}{dT}$, which are also noticeable in the kinks in the RvT traces shown in Figure 4.1(a). Open symbols represent the transition temperatures from a second sample measured in a PPMS up to 14K. Focusing on the quadrupolar transitions, these extracted temperatures T_Q are consistent with a fit from a mean field Hamiltonian described in Eq. 4.1 in the discussion section, with a gap of $\Delta_o = 3.5K$. This work will not focus on either of the magnetic phase transitions, although it is worth noting that the phase diagram is suggestive that they are suppressed to 0K at a similar field as the quadrupolar phase transition.

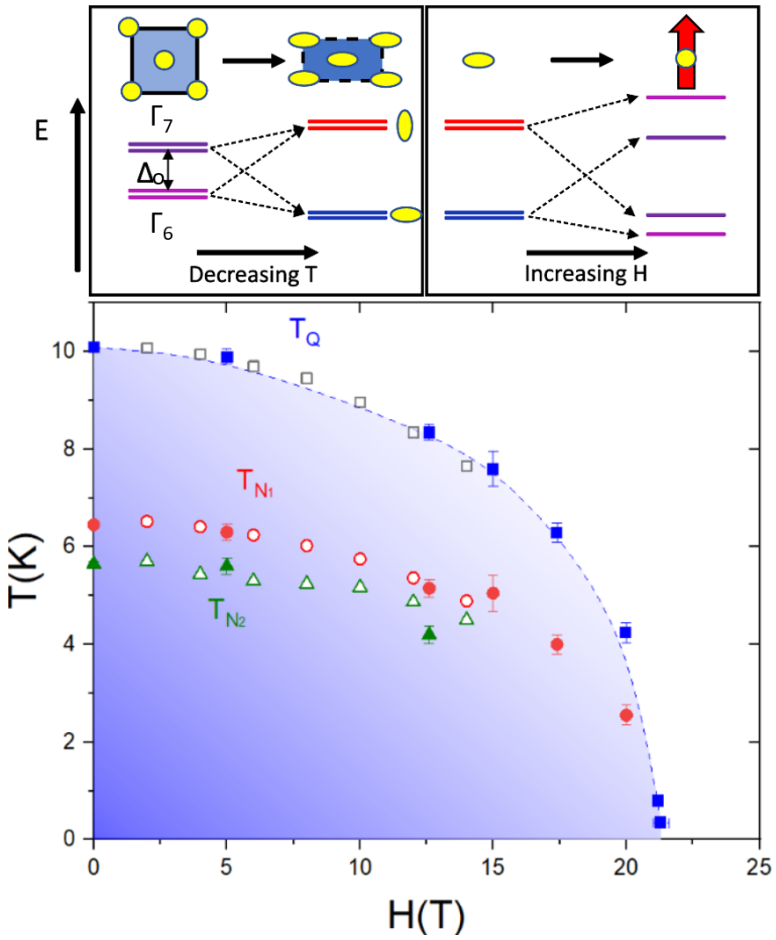

Figure 4.2: **H-T phase diagram of $YbRu_2Ge_2$.** The top left panel illustrates the CEF ground state quasi-quartet for $YbRu_2Ge_2$ and how the spontaneous ferroquadrupolar phase transition mixes and shifts the spectrum. Quadrupolar matrix elements between the excited Γ_7 doublet and the Γ_6 doublet mix their states, and the corresponding gap adds in quadrature with the CEF gap Δ_o. The low temperature states are still doublets as time-reversal symmetry hasn't been broken. The right frame displays the low-temperature energy spectrum when magnetic field is applied. The quadrupolar doublets split back into to the m_j eigenstates, and at high enough fields the ferroquadrupolar order is destroyed. The lower panel shows the H-T phase diagram as inferred from resistivity measurements. The closed symbols represent phase transitions measured for a sample at the Maglab in a 35T resistive magnet, the open symbols from a different sample in a 14T PPMS at Stanford University. Blue squares denote the ferroquadrupolar phase transition, and the blue shading represents when the crystal structure is no longer tetragonal. The red circles denote the anti-ferromagnetic phase transition, and the green triangles represent a proposed spin re-ordering phase transition. The signature for the low-temperature spin re-ordering wasn't resolved in the resistivity derivatives above 14T. The ferroquadrupolar phase boundary is consistent with a mean-field Hamiltonian as in Eq. 4.1 with a quasi-quartet gap of $\Delta_o = 3.5K$.

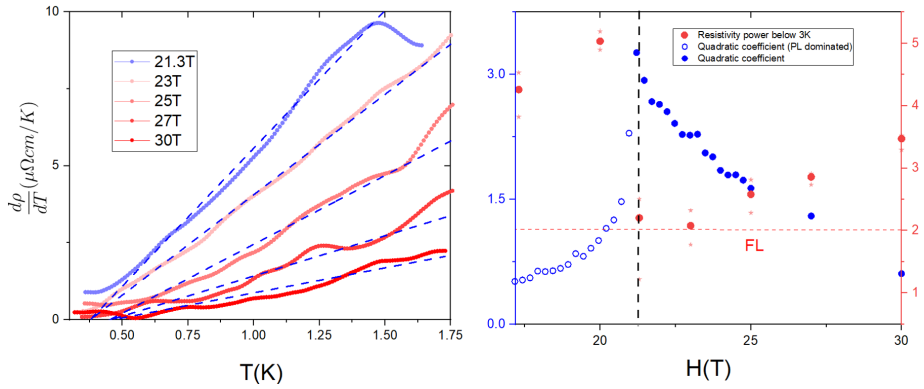

Figure 4.3: **Power law behavior of the resistivity proximate to the crtical field H_c.** The left plot displays the temperature derivative of the resistivity for fields at and above the critical field at temperatures from 0.35K to 1.75K. Each trace is fit to a line from 0.5K to 1.5K, as there is deviation from linear behavior below 0.5K. Linear behavior indicates a quadratic T-dependence of the resistivity. There is a robust increase in the slope (the quadratic coefficent for the resistivity) as the field approaches the critical field. The quadratic coefficients are plotted as the blue points in the right plot as a function of field, and these coefficients were extracted from the low temperature RvH traces, allowing high data density. The open blue points are also the extracted quadratic coefficents for data below the critical field, but the overall power law behavior of the resistivity ($\rho = \rho_o + AT^b$, b plotted by the red dots) below the critical field indicates that a high power law relation describes the low temperature resistivity more accurately. Above the critical field however the resistivity approaches $\rho = \rho_o + AT^2$ as the critical field is approached.

4.4.2 Resistivity proximate to the critical field

As this H-T phase diagram maps to a transverse field Ising-like phase diagram (see section 1.6.5 and discussion section), we are motivated to look at the resisitivity in the proximity of the critical field $H_c = 21.3T$ for any evidence of quantum criticality, particularly from the disordered part of the phase diagram approaching the critical field.

The low temperature derivatives of the resistivity are shown for magnetic fields at and above the critical field in Figure 4.3a. The resistivity below the lowest temperature magnetic phase transition can be described by a power law $\rho = \rho_o + AT^b$ with $b > 3.5$ for magnetic fields $H < H_c$. This behavior is likely associated with collective excitations/fluctuations of the antiferromagnetic state. However, for $H > H_c$, this switches to a more prominent Fermi-liquid like behavior with $b \approx 2$ (as shown by the linear T fits to the temperature derivatives in Figure 4.3a), with a quadratic T^2 coefficient that increases in magnitude as the magnetic field approaches the critical field (Figure 4.3b). This type of resistivity behavior has been seen in materials such as $BaFe_2(As_{1-x}P_x)_2$ in the proximity of a putative nematic quantum critical point [57], although importantly $YbRu_2Ge_2$ appears to provide access to a "bare" nematic quantum critical point at 21.3T without an intervening superconducting state.

4.4.3 Elastoresistivity as a function of field and temperature

Elastoresistivity was shown to be a sensitive probe of the quadrupole-strain suceptibility χ_Q (the nematic susceptibility) of this material in the previous chapter, characterizing the fluctuations of the nematic order parameter in the disordered tetragonal phase. In this section we focus on the B_{1g} elastoresistivity measurements (of the same symmetry channel as the spontaneous ferroquadrupolar order parameter) as a function of magnetic field up to 14T. Although applying a magnetic field will change the symmetry considerations such that we no longer probe just $\chi_Q^{B_{1g}}$ (see discussion section), nonetheless this measurement is sensitive to the field dependence of the quadrupole-strain susceptibility.

B_{1g} elastoresistivity traces measured on a different sample (the one with transition temperatures denoted by open symbols in Figure 4.2) in a PPMS from 0 to 14T are shown in Figure 4.4. As previously mentioned, at zero magnetic field this quantity is a direct probe of the quadupole-strain/ nematic susceptibility of the order parameter for the ferroquadrupolar phase transition. This data was acquired via elastoresistivity measurements from a square microstructured pattern (as described in and sections 2.2 and 4.2), which is different from previous elastorestivity measurements of this material. The Curie-Weiss fit for the measurement in 0T is still in agreement with the transverse elastoresistivity measurement from the previous chapter, (Weiss temperature $\theta \approx 0$) but only in the window of 10-30K. The higher temperature data deviates more substantially, likely a result from differing strain conditions as well as different geometric offset terms.

Inspection of Figure 4.4 reveals a robust increase in the magnitude of the elastoresistivity coefficient $\frac{1}{\rho}\left(\frac{d\rho_{B_{1g}}}{d\varepsilon_{B_{1g}}}\right)$ as magnetic field increases. In fact, at 11K the response nearly doubles from -60 to -110, as shown in the left panel of Figure 4.5. The field dependence of the elastoresistivity at 11K is almost completely even with respect to field, and is quadratic in field from $H_z = -5T$ to $5T$, as shown by the quadratic fit (red dashed line) in the left panel of Figure 4.5. This quadratic coefficient in this field range is plotted as a function of temperature in the right panel of Figure 4.5. It diverges as temperature is decreased, indicative of multipolar couplings which will be described in greater detail in the discussion section.

As described in the discussion section, the behavior described above is unexpected from a simplistic picture of 4f quadrupolar moments arising from a J=3/2 manifold being split by magnetic field, for which the quadrupole-strain susceptibility should *decrease* in magnitude and rollover as magnetic field is increased. If octupolar moments are included in this Hamiltonian, however, these qualitative trends in the data can be explained, and (non-unique) sets of parameters of octupolar couplings and interactions can even quantitatively explain this "anomalous" increase of the elastoresistivity in magnetic field (see discussion).

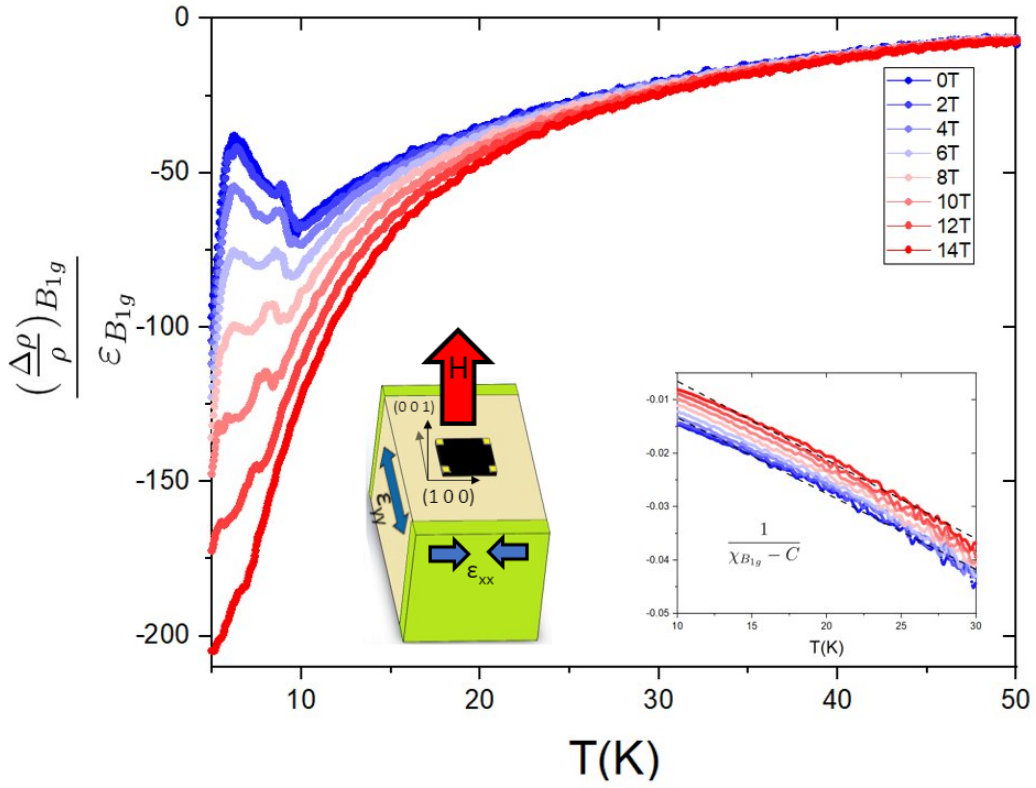

Figure 4.4: **Field-dependence of the T-dependence of the elastoresistivity of $YbRu_2Ge_2$.** B_{1g} Elastoresistivity data for magnetic fields from 0T (blue) to 14T (red) are shown. There is a robust increase in the magnitude with magnetic field, which was seen in multiple samples. The traces diverge towards higher temperatures as well as magnetic field is increased. This can be seen more clearly in the lower right inset graph, which depicts the reciprocal of each trace (minus a small temperature independent offset). The inverse traces appear to be just vertically offset from each other, and the offset is a monotonic function of field. This would correspond to an increase of Weiss temperature with field, given these traces were interpreted as belonging to a Curie-Weiss functional form. The lower middle diagram depicts the geometry of the experiment: anti-symmetric strain is applied to the crystal (via applying voltage to the piezoelectric device) in the ab plane along the (1 0 0) and (0 1 0) axes, and the sample's resistivity is measured via a Montgomery geometry along those same axes. In reality the Montgomery square was microstructured to precisely define the resistivity measurements. Magnetic field was applied along (0 0 1).

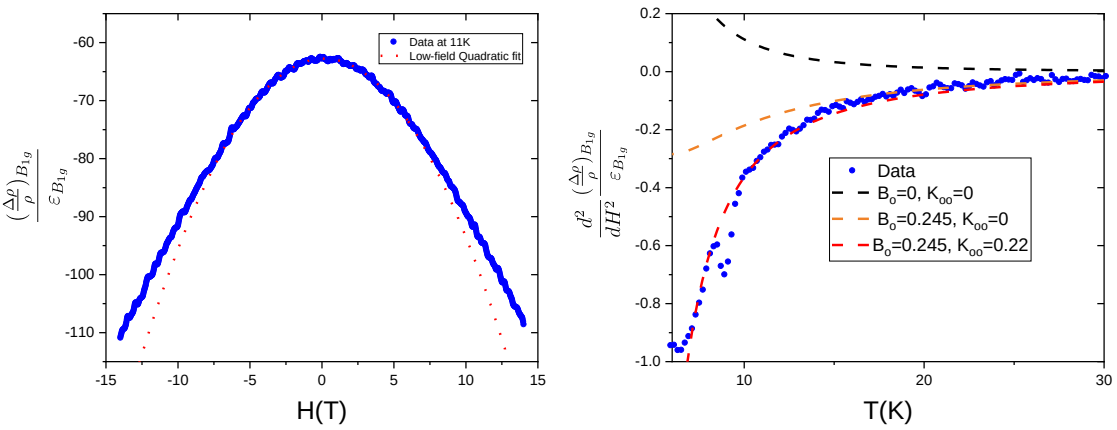

Figure 4.5: **Quadratic field-dependence of the elastoresistivity of $YbRu_2Ge_2$ at fixed temperatures.** The left plot is the measured B_{1g} elastoresistivity coefficient from -14T to 14T at 11K. There is very little contamination of field-odd terms, and it is described well by a quadratic field coefficient from -5T to 5T, with the quadratic fit shown by the dashed red line. This coefficient is plotted as a function of temperature in the right plot (blue dots) along with various simulated results with different octupolar coefficents in the mean-field Hamiltonian. The black dashed line represents the "octupolar susceptibility", or the second field derivative of the B_{1g} susceptibility, if there are no octupolar contributions to the Hamiltonian. The sign is positive even though the initial quadrupole-strain susceptibility is fixed to be negative, this signifies that the magnitude of the quadrupole-strain susceptibility reduces in field with no octupoles, as expected. The orange dashed line represents a Hamiltonian with only an additional bilinear octupolar coupling with no mean-field interactions, and it does not explain the faster divergence in the data. Finally the red dashed line is the quadrupole-strain susceptibility of a Hamiltonian that incorporates an octupole-octupole interaction term to be able to accurately describe the data.

4.5 Discussion

Here we discuss the magnetic field dependence of the B_{1g} elastoresistivity, and how local octupolar couplings and interactions can explain its "anomalous" increase as magnetic field is increased. We also comment on the resistivity data and how it is suggestive of quantum criticality in the proximity of the critical field.

4.5.1 Magneto-elastoresistivity

To discuss the magnetic field dependence of the elastoresistivity, we need to introduce the relevant Hamiltonians for the quasi-quartet ground state of $YbRu_2Ge_2$, and their corresponding quadrupole-strain susceptibilties. We will first introduce a simplistic Hamiltonian which only considers dipoles and quadrupoles, and see that the quadrupole-strain susceptibility does not adequately describe the results described in the previous section. We then introduce a Hamiltonian that incorporates octupolar degrees of freedom, and see that they potentially can explain both the qualititative and quantitative changes in the elastoresistivity, as well as being consistent with the measured H-T phase diagram.

Effective Hamiltonian in magnetic fields neglecting octupolar terms

We start by writing down the relevant mean-field Hamiltonian for the $4f$ ground state quasi-quartet, considering only dipole and quadrupole moments.

The $4f$ electrons of the trivalent Yb ion form local electronic multiplets with a total angular momentum quantum number J=7/2, dictated from spin-orbit coupling. The J=7/2 spinor representation reduces to the irreducible representations $2\Gamma_6 \oplus 2\Gamma_7$ in the D_{4h} tetragonal point group symmetry. Numerous experiments have provided evidence that the ground state is composed of a quasi-quartet, with the gap of $\Delta_0 < 10$K between the ground-state Γ_6 doublet (proposed to be primarily $\pm|1/2\rangle$ states) and the Γ_7 (primarily $\pm|3/2\rangle$ states) doublet (Figure 4.2a). The excited states are well above in energy ($> 300K$), making them irrelevant to the low temperature physics. This quasi-quartet has $4f$ quadrupolar degrees of freedom that interact via the lattice through strain, and via interactions mediated by the conduction electrons through the RKKY (Rudelman-Kittel-Kasuya-Yosida) effect. Because strain is a long-range interaction, is it proposed that a mean-field model will accurately describe the quadrupolar physics [7]. We thus consider the mean-field Hamiltonian relevant to the ground state-quasi-quartet including dipoles and quadrupoles:

$$\hat{H}_{4f}^{M,Q} = \Delta O_2^0 - B_2^2 O_2^2 \varepsilon_{B_{1g}} - K\langle O_2^2\rangle O_2^2 - g_J \mu_B H_z J_z \tag{4.1}$$

In which ΔO_2^0 is the term that creates the intra-quartet gap Δ_o (see Table 1.1 for definition of the O_2^0 operator), O_2^2 is the B_{1g} quadrupole $J_x^2 - J_y^2$, $\varepsilon_{B_{1g}}$ is the conjugate strain $\frac{1}{2}(\varepsilon_{xx} - \varepsilon_{yy})$, B_2^2 is the standard magnetoelastic coupling constant, K is the mean-field quadrupole-quadrupole coupling

constant mediated by conduction electrons, and J_z is the standard angular momentum operator. All of these operators are projected onto the ground state quasi-quartet. As shown in section 1.5, this Hamiltonian will result in a finite temperature ferroquadrupolar phase transition with a critical temperature of approximately $(B^2/C + K)Q_o^2$, although the gap term changes this by functioning as a fixed tranverse field to the B_{1g} quadrupole. The application of H_z will suppress this phase transition temperature as written in Eq. 1.60, eventually to 0K.

Quadrupole-strain susceptibility without octupoles

The quadrupole-strain susceptibility can be calculated for the Hamiltonian shown in Eq 4.1. This quantity, (which indicates the quadrupolar moment that is induced by an infinitesimal applied strain of the same symmetry), was experimentally shown to diverge in the B_{1g} symmetry channel in Chapter 3 via elastoresistivity measurements, and this was expected due to the quasi-quartet mapping to a non-Kramer's doublet. However, magnetic field does not simply map to this model, and so now the expression describing this will be more complicated. Nonetheless it will generally show the same trends, which are the reduction in amplitude and rollover of the susceptibility as a magnetic field is applied.

The thermodynamic quadrupole-strain susceptibility that would arise from the Hamiltonian in Eq. 4.1 applied to the quasi-quartet is:

$$\chi_{B_{1g}} = \frac{dQ}{d\varepsilon_{B_{1g}}}\bigg|_{\varepsilon=0} = \sum_{i=1}^{2} \frac{B_2^2 Q^2 \sinh(\frac{\Delta_i}{k_B T})}{\Delta_i} \frac{e^{\left(\frac{(-1^i) g_J \mu_B H_z}{2 k_B T}\right)}}{Z} \tag{4.2}$$

in which $\Delta_1 = \Delta_o/2 - g_j\mu_B H_z$ and $\Delta_2 = \Delta_o/2 + g_j\mu_B H_z$, and Z is the partition function: $Z = \exp(-\Delta_o/2k_BT)\cosh(3g_J\mu_B H_z/2k_BT) + \exp(\Delta_o/2k_BT)\cosh(g_J\mu_B H_z/2k_BT)$. These are the gaps between the states with quadrupolar matrix elements, which arise from the addition of the quasi-quartet CEF gap Δ_o and the gap induced by a magnetic field. K is approximated to be 0 here, as was determined in previous elastoresistivity experiments (Chapter 3). Significantly, following this equation we would expect the quadrupole-strain susceptibility to *decrease* in magnitude as the field is increased. This effect arises from the splitting and polarizing of the Γ_6 and Γ_7 CEF eigenstates as the field is increased.

In Chapter 3 we argued that the quadrupole-strain susceptibility is proportional to elastoresistivity in the same symmetry channel: $m_{B_{1g}} = g\chi_{B_{1g}}$. The Curie-Weiss T-dependence of $m_{B_{1g}}$, along with the arguments made in section 3.6.5, indicate that the proportionality term g is independent of temperature. Hence, if g is independent of field, as well as temperature, the analysis described above would imply that the elastoresistivity should *decrease* as a function of field due to the field-dependence of χ_Q. This is in sharp contrast to the observation (Figure 4.4) that $m_{B_{1g}}$ dramatically *increases* with increasing fields. Hence either g must either be strongly dependent on field, or the effective Hamiltonian in Eq. 4.1 must be missing crucial terms. We first consider this latter scenario,

explicitly including octupolar degrees of freedom.

Quadrupole-strain susceptibility with octupolar degrees of freedom

Here we discuss the allowed octupolar degrees of freedom of the quasi-quartet ground-state, and see the consequences of adding them into the mean-field Hamiltonian on the quadrupole-strain susceptibility.

Because of the multiple degrees of freedom of the ground state, the 4f multiplet can support many multipolar instabilities, not just limited to the magnetic and quadrupolar order parameters. The irreducible representations of allowed symmetry breaking orders for the quasi-quartet (which can be represented as $\Gamma_6 \oplus \Gamma_7$) are contained in the right hand side of this equation:

$$(\Gamma_6 \oplus \Gamma_7) \otimes (\Gamma_6 \oplus \Gamma_7) = 2A_{1g} \oplus 2A_{2g} \oplus 2B_{1g} \oplus 2B_{2g} \oplus 4E_g \tag{4.3}$$

If we only consider the approximation in which the ground state consists of Kramer's doublets $|\pm\frac{1}{2}\rangle$ and $|\pm\frac{3}{2}\rangle$, then the highest order multipolar moment allowed is l=3 or the octupolar moments. In fact, every multipole below order 3, with their 2l+1 mulitplicity, are included in the allowed (orthogonal) irreducible representations listed above. If the ground state did not consist of those pure m_j eigenstates, multipoles of higher order than octupole would also be allowed, but they would have to correspond to the listed irreducible representations, and hence would couple to the same products of magnetic fields with strains. We thus restrict our discussion to octupolar degrees of freedom.

In considering the magneto-elastoresistivity tensor measurement of $YbRu_2Ge_2$, in which both strain and magnetic field are relevant fields, it is crucial that the appropriate higher order multipoles are included in the $4f$ Hamiltonian. In particular, if B_{1g} strain $\varepsilon_{B_{1g}} = \frac{1}{2}(\varepsilon_{xx} - \varepsilon_{yy})$ and a c-axis oriented magnetic field H_z are applied, then the quasi-quartet allowed B_{2g}^- octupolar moment represented by the operator $O_3^2 = J_z(J_x^2 - J_y^2) + (J_x^2 - J_y^2)J_z$ must be considered, as it has a bilinear coupling with its two parameter conjugate field $H_z\varepsilon_{B_{1g}}$ (see section 1.3).

Consider the previous Hamiltonian from Eq. 4.1, but now add terms that arise from couplings to octupolar degrees of freedom. For simplicity, only the bilinear octupole-conjugate-field coupling and a mean field octupole-octupole coupling term are included, as other allowed couplings up to second order in order parameters will renormalize quantities similarly.

$$\hat{H}_{4f}^{tot} = \hat{H}_{4f}^{M,Q} - B_o O_3^2 H_z \varepsilon_{B_{1g}} - K_{oo}\langle O_3^2\rangle O_3^2 \tag{4.4}$$

First considering just the bilinear octupole-conjugate field term, the quadrupole-strain susceptibility

is now renormalized by magnetic field:

$$\chi_Q = \sum_{i=1}^{2} \frac{(B_2^2 Q^2 + (-1^i) Q B_o H_z) \sinh(\frac{\Delta_i}{k_B T})}{\Delta_i} \frac{e^{(\frac{-(1^i) g_J \mu_B H_z}{2 k_B T})}}{Z} \tag{4.5}$$

where Δ_i are the same field dependent gaps as in Eq. 4.2. The second term in the numerator of the sum is an additional term that arises from the inclusion of the bilinear coupling between the octupole O_3^2 and the product of magnetic field and B_{1g} strain. Note that if $\Delta_1 = \Delta_2$, that this term will cancel out with itself, and there will be no effect on the quadrupole-strain susceptibility. Only if the system has a finite magnetic moment will the quadrupole-strain susceptibility be renormalized by the octupolar coupling. In other words if the system simultaneously possesses a A_{2g}^- magnetic moment and a B_{2g}^- octupolar moment, then a quadrupole moment that is the product of these two moments, in this case belonging to the B_{1g}^+ representation ($A_{2g}^- \otimes B_{2g}^- = B_{1g}^+$) will be induced, and it will be induced quadratically with field (the magnetic moment and octupolar moments are induced linearly with magnetic fields at small fields), effectively renormalizing the quadrupole-strain susceptibility with field.

In the limit of vanishing magnetic field the second derivative of this quadrupole-strain susceptibility is given by:

$$\left.\frac{d^2 \chi_Q}{dH^2}\right|_{H=0} = Q B_o \tanh\left(\frac{\Delta_o}{2 k_B T}\right) \tag{4.6}$$

which implies the magnitude of the quadrupole-strain susceptibility will be *increased* as field is applied. Interaction terms like third term in Eq. 4.4, (i.e: $K_{ij}\langle O_i^2\rangle O_j^2$ where i and j can be 2 or 3), will renormalize Eq. 4.6 such that the "octupolar susceptibility" diverges at a finite temperature rather than like $\tanh(\Delta_o/T)$ ($\sim 1/T$ for small Δ_o). Significantly, the inclusion of both a bilinear octupole coupling and an interaction term in the Hamiltonian results in an increase of the magnitude of the quadrupole-strain susceptibility and also can account for the appearance of a monotonically renormalized Weiss temperature in the Curie-Weiss fits, both of which are seen in Figure 4.4. Furthermore the calculated magnetic field phase diagram remains consistent with the measured phase diagram in Figure 4.2.

4.5.2 Relating to quadrupole-strain susceptibility

As discussed in Chapter 3 and more specifically in section 3.6.5, for $4f$ systems in which $4f$ scattering is the dominant scattering mechanism, the elastoresistivity tensor element which relates strain of a certain symmetry channel to the induced resistivity change of that same symmetry channel is a direct probe of the corresponding quadrupole-strain susceptibility, for instance: $m_{B_{1g}} = g\chi_{B_{1g}}$, with the proportionality constant g being temperature independent. However this neglects magnetic field, which not only changes the fundamental symmetry considerations for this material, but also is allowed to function as a tuning parameter which can affect the transport coefficient g. Taking a

look at the symmetry considerations, for a finite applied magnetic field the original point group of the space group of the material (in the case of $YbRu_2Ge_2$, D_{4h}) will now been reduced (applying H_z will reduce D_{4h} to C_{4v}) , and so the irreducible representation of the resistivity measurement (B_{1g} for these measurements) reduces or is equvalent to other originally distinct symmetry channels (B_{1g} and B_{2g} both become B_1 in C_{4v}), hence the B_{2g}^- octupole O_3^2 will be measured in a originally B_{1g} measurement. Thus to be precise for these elastoresistivity measurements on $YbRu_2Ge_2$, the response is the linear combination of two objects:

$$\frac{1}{\rho_o}\frac{d\rho_{B_{1g}}}{d\varepsilon_{B_{1g}}}(H_z^2) = g_Q\frac{d\langle O_2^2\rangle}{d\varepsilon_{B_{1g}}}(H_z^2) + g_O H_z^2\frac{d\langle O_3^2\rangle}{d(H_z\varepsilon_{B_{1g}})} \tag{4.7}$$

where the first term on the right hand side is the familiar quadrupole-strain susceptibility, which is renormalized by magnetic field (from even powers of H_z from symmetry) as discussed previously, and the second term is effectively H_z^2 multiplied by the material's octupolar susceptibility. This second object can be imagined as an additional scattering channel comprised of the interaction between magnetic field and local octupoles which contributes to changes in resistivity in the B_{1g} symmetry channel. For $YbRu_2Ge_2$, in which quadrupole-octupole interactions are allowed in the presence of magnetic field, the second term with the octupolar susceptibility will be renormalized by quadrupolar interactions to be sensitive to the form of the quadrupole-strain susceptibility in field (just as the field dependent quadrupole-strain susceptibility was sensitive to the octupolar susceptibility as seen in Eq. 4.5 and 4.6), and will be hard to distinguish experimentally in elastoresistivity measurements.

The issue of fitting the field-dependence of the elastoresistivity is further complicated by practical strain-transmission issues. Specifically, as shown in Figure 4.4, even in zero applied field individual elastoresistivity traces cannot be described accurately by Curie-Weiss fits at temperatures above 30K due to potentially large contributions arising from strain heterogeneity and geometric terms, (also see the deviations from linearity in the traces in the inset graph of Figure 4.4). As a consequence we hesitate to fit to individual traces with the quadrupole-strain susceptibiliies obtained from Hamiltonians shown in Eqs. 4.2 and 4.4, especially considering the additional symmetry complications outlined at the beginning of this section. Broad trends are, however, much more compelling than finer details of such fits, and we note that the octupolar couplings described above provide a natural explanation for the field-dependence of the elastoresistivity shown in Figures 4.4 and 4.5. Moreover, the quadrupole-strain susceptibilities from the Hamiltonian in Eq. 4.4 have a similar temperature and field dependence as the data in Figure 4.4, and added parameters can be fixed that accurately describe the H^2 coefficient (dashed lines in the right hand panel of Figure 4.5).

4.5.3 Field-dependence of g

Considering now the potential dependence on the transport coefficient g on magnetic field, we see that that octupolar terms in the Hamiltonian for instance described in Eq. 4.4 only accurately

describe the measured elastoresistivity if g is not a function of H or T. A transport coefficient that diverges with respect to a tuning parameter as the system is tuned to a putative quantum critical point would not be entirely unexpected. For instance, some recent measurements on the pnictide superconductor system $Ba(Co_xFe_{(1-x)})_2As_2$ indicate the proportionality constant between elastoresistivity and the corresponding nematic susceptibility increases by an order of magnitude as x approaches the optimally doped region[58, 59]. However, for $YbRu_2Ge_2$, g would have to be also divergent as temperature decreased to explain the right panel of Figure 4.5, and the smooth and monotonic increase of the effective Weiss temperature of the elastoresistivity traces as field is increased (see the offset panel of Figure 4.4) would require a fine-tuning of this temperature dependence, which seems unlikely. Thermodynamic measurements, for instance measuring the elastocaloric effect in field, could in principle resolve this. While such a scenario cannot be ruled out without such measurements, we stress that regardless, the ground state of $YbRu_2Ge_2$ necessitates that local octupolar degrees of freedom be considered when experiments which combine strain and magnetic field are performed, which include the elastoresistivity measurements in this work.

4.5.4 Resistivity

The cusp of the low temperature resistivity increasing as a function of temperature near the proximity of the completely suppressed ferroquadrupolar transition at 21.3T seen in the right part of Figure 4.1, the increase of the quadratic coefficient as H_c is approached from the disordered phase, and the effective power law approaching $\rho = AT^2$, all are suggestive that quantum critical fluctuations may be playing a role in the resistivity in this part of the phase diagram. Without more definitive and exhaustive scaling and power law data we hesitate to draw any more conclusions than this.

4.6 Conclusion

These resistivity measurements establish the H-T phase diagram of $YbRu_2Ge_2$ (at least of the ferroquadrupolar phase), which through its approximate mapping to the transverse field Ising model suggests that there is a nematic quantum phase transition at 21.3T. The increase of the quadratic coefficent of the resistivity towards this field from the disordered phase of the low-temperature resistivity provide additional evidence this system exhibits quantum criticality. However more thorough characterization of this part of the phase diagram through transport and thermodynamic measurements needs to be performed to make more conclusive statements.

The elastoresistivity measurements provide evidence that octupolar moments and their couplings and interactions play a important role in the low temperature physics of $YbRu_2Ge_2$. These couplings renormalize the quadrupole-strain susceptibility such that it increases in magnitude and diverges towards higher temperatures as magnetic field is increased, opposite of what would be expected if only dipole and quadrupole moments were considered. However these measurements cannot rule out

the possibility that instead a transport coefficient which increases in field and diverges as temperature is decreased causes this behavior. We conclude with the fact that regardless of the source of the field renormalization of the elastoresistivity, octupoles must be considered for the ground state of this material if magnetic field is applied at low temperatures, and that magneto-elastoresistivity can be a sensitive probe of octupolar fluctuations and their related couplings.

More generally, we remark that magneto-elastoresistivity measurements can present evidence of local octupolar couplings and octupolar interactions, and in this case this measurement is one of the first to do so in a $4f$ intermetallic material. Due to the multiple experimental tuning parameters accessible in the magneto-elastoresistivity technique, it generally allows higher-order multipolar behavior to be explored, specifically through their couplings to powers of strain and magnetic field.

Chapter 5

Elastocaloric and transport properties of $TmAg_2$

Similar to $YbRu_2Ge_2$, which was featured in Chapters 3 and 4, $TmAg_2$ is an intermetallic compound for which the local $4f$ degrees of freedom undergo a ferroquadrupolar phase transition. However, unlike $YbRu_2Ge_2$, the crystal field ground state of the Tm^{3+} ion in $TmAg_2$ is a simple non-Kramer's doublet (i.e. can be split withought breaking time reversal symmetry). Considering for a moment only the restricted Hilbert space of the single-ion ground state, which is justified at low temperatures (see section 1.6.3), it maps precisely to the spin 1/2 Ising model.

As we've shown in section 1.6.3, a magnetic field applied along the c-axis H_z, and the B_{2g} shear strain ε_{xy}, map to transverse fields for the longitudinal ordering field, the B_{1g} quadrupole O_2^2, which aligns in this material at 5K in a ferroquadrupolar phase transition. As the mean-field transverse field Ising model is the paradigmatic model for obtaining a quantum critical point via the application of transverse fields, this motivates us to explore the phase diagram of $TmAg_2$, using both magnetic field and strain as tuning parameters. The material then permits investigation of the effects arising from interaction of the potentially quantum critical $4f$ quadrupolar degrees of freedom and the separate metallic degrees of freedom.

In this section we will present a novel strain-based technique, the elastocaloric effect, which induces strain in the sample and measures the corresponding temperature change that arises from electronic entropy shifts, and apply it to $TmAg_2$ simultaneously with magnetic fields along the c-axis to map out the H-T phase diagram. Furthermore, this technique probes strain derivatives of the transition temperature and quadrupole-strain susceptibilities, which we will show map into the paradigm of the transverse-field Ising model. We also investigate the resistivity and heat capacity of the material in the H-T plane.

5.1 Introduction

5.1.1 Background on $TmAg_2$

$TmAg_2$ is a $4f$ intermetallic material which undergoes a spontaneous ferroquadrupolar phase transition at 5K, proposed to be second order [3]. The localized $4f$ electrons have a single ion ground state of a non-Kramer's doublet [3], and as discussed in sections 1.5 and 1.6, this configuration can map precisely to a site in Ising models. This motivates studying this material to explore the effects of interaction of metallic degrees of freedom with an Ising model like lattice with local electronic degrees of freedom. In this section we introduce the Hamiltonian for this material which creates this energy spectrum, and then introduce the relevant tuning parameters that can potentially tune this system towards a quantum phase transition, and how these are applied in the measurements featured in this chapter.

The effective Hamiltonian describing the low-energy properties of 4f ions incorporated in crystalline solids is understood in great detail. The $4f$ electronic wavefunctions are spatially localized, and so form a lattice of local electronic sites. $4f - 4f$ coupling arises both from the coupling of the quadrupolar degrees of freedom to the lattice, and the generalization of the Ruderman–Kittel–Kasuya–Yosida (RKKY) interaction, mediated by the conduction electrons in metals [2, 10]. This provides an effective exchange interaction between the $4f$ sites, analogous to the exchange interaction writtten down in Ising models. Each site has strong spin-orbit coupling which yields an electronic multiplet that is described by a total angular momentum number J . Due to the local nature of the multiplet, the crystal electric field (CEF) from the surrounding ligands acts as a weak perturbation, splitting the degeneracy of the spherical harmonic basis states.

Significantly, the low-energy states of these $4f$ electronic multiplets can exhibit degeneracies, the multiplicity of which is determined by the point-group symmetry and charge distribution surrounding the $4f$ ion. For tetragonal materials with even angular momentum number J, Γ_5 doublets, (i.e. E_g symmetry, which transforms like xz, yz), can be the ground state of the $4f$ system, as is the case for $TmAg_2$. At low enough temperatures relative to the excited states this doublet becomes the dominant source of $4f$ physics, and perhaps even of the coupled itinerant and local electronic system. Materials with this ground state configuration are ideal candidates to compare to a spin 1/2 Ising model.

As shown in previous work (Ref. [31]), in this restricted Hilbert space for $TmAg_2$, B_{2g} strain and magnetic field H_z directed along the c-axis map precisely to transverse fields, and hence this system maps to a transverse field Ising model. This material stands in contrast with the paradigmatic case of $4f$ ferroquadrupolar order in the insulating compound $TmVO_4$, which has a phase transition at 2K, as $TmAg_2$ contains metallic degrees of freedom that interact with the local $4f$ Ising lattice. We might still expect to tune the ferroquadrupolar transition towards a nematic quantum critical point via the application of a transverse field, but this assumes the metallic degrees of freedom don't

couple strongly enough to the $4f$ sublattice to fundamentally change the low-temperature behavior of the total coupled system. The interactions between the metallic part of this material and the $4f$ sublattice are then of particular interest in the proximity of the potentially completely suppressed phase transition.

5.1.2 Strain in $TmAg_2$

$TmAg_2$ undergoes only one phase transition, a ferroquadrupolar phase transition occurring at 5K. The local $4f$ electronic multiplets, which for the Tm^{3+} ion harbor quadrupolar degrees of freedom, develop spontaneous electronic quadrupolar moments which collectively align at this phase transition. The macroscopic quadrupolar order parameter breaks the four-fold rotational symmetry of the lattice, and so the lattice distorts (i.e spontaneous strain) in a similar fashion due to its coupling to the order parameter. Herein lies a crucial point: because strain, which represents the internal degree of freedom of the lattice to distort, is a second-order tensor quantity (strain is defined as the symmetric spatial derivative of a displacement vector), it couples bilinearly to the quadrupoles of the same symmetry. This coupling guarantees that for a finite applied strain (induced by external stresses) of the appropriate symmetry there will be a non-zero induced quadrupolar moment, and vice versa. Thus techniques in which the material experiences strain are directly applying the conjugate field for ferroquadrupolar phase transitions, and so are of considerable interest for materials like $TmAg_2$. Specifically we use the AC elastocaloric effect technique, which measures temperature changes of samples induced by applied strain, and recently was developed and applied only in studying pnictide superconductors, and apply it to $TmAg_2$ in this text. As has been shown in Ref. [8], this technique under certain assumptions laid out in Section 2.3 measures the quantity:

$$\frac{dT}{d\varepsilon} = \frac{C_p^c}{C_p^c + C_p^{nc}} \frac{dT_Q}{d\varepsilon} \tag{5.1}$$

Where C_p^c is the component of the material's heat capacity that is dependent on strain, $\frac{dT_Q}{d\varepsilon}$ is the phase transition temperature's strain dependence, and C_p^{nc} is the background heat capacity arising mainly from phonons that isn't strongly strain-dependent. Because the phase transition for $TmAg_2$ causes a large heat capacity jump (mean-field step) relative to the background at 5K, it serves as ideal candidate material for this measurement not only to identify the phase transition sharply, but also to find strain derivatives of T_Q. This text will discuss how these derivatives evolve as a function of magnetic field approaching the putative nematic quantum critical point, and show that these quantities fit in the framework of the transverse-field Ising model with strain as an effective transverse field. Furthermore the elastocaloric effect has also recently been shown to be a sensitive probe for nematic susceptibilities [58], and this text will discuss the evolution of the nematic susceptibility in the magnetic field phase diagram as well.

5.1.3 Model Hamiltonian for $4f$ degrees of freedom

We first introduce a model $4f$ Hamiltonian for $TmAg_2$ neglecting metallic degrees of freedom (besides the inclusion of a interaction between $4f$ sites mediated via conduction electrons treated at a mean-field level), for which the CEF spectrum has a ground state non-Kramer's doublet which maps precisely to the spin 1/2 Ising model.

$TmAg_2$ is a rare-earth intermetallic material with tetragonal crystal structure at room temperature (space group I4/mmm), and belongs to the $MoSi_2$ structure type. The $4f$ electrons of the trivalent Tm ion form local electronic multiplets with a total angular momentum quantum number J=6. The 2J+1= 13 states are split by the surrounding crystalline electric field (CEF), and heat capacity and inelastic neutron scattering measurements provide evidence that the ground state is a Γ_5 (E_g, transforms as xz and yz, see section 1.3) doublet (composed of $m_J = |\pm 5\rangle$, $|\pm 3\rangle$, and $|\pm 1\rangle$ states [3]). The nearest excited state is an Γ_1 (composed of $|\pm 4\rangle$, $|0\rangle$ states) singlet at 14K [3]. Most notably, this is the only metallic $4f$ tetragonal material known to undergo only a continuous ferroquadrupolar phase transition, (coupled with a tetragonal-to-orthorhombic structural phase transition) this occurring at 5K with an O_2^2 (B_{1g} symmetry) order parameter. This phase transition is driven by local electronic degrees of freedom to break the rotational symmetry of the lattice, and hence is an example of an electronic nematic phase transition. No other phase transitions have been observed in this material above 1.5K.

The operators O_2^2, M_z and the B_{2g} Stevens operator P_{xy} will map onto the the standard Pauli matrices σ_i when applied to the restricted subspace of the ground state Γ_5 doublet (see sections 1.6.2 and 1.6.3). They obey the same canonical commutation relations, and so H_z and ε_{xy} (which couple to J_z and P_{xy} respectively) will serve as effective transverse fields to the spontaneous nematic B_{1g} order, and hence can tune the $4f$ sublattice to quantum criticality. We note that although this mapping is only an approximation to describing the $4f$ physics of the material, as the whole manifold of 13 CEF states should be considered, numerical simulation results featured in this work which include the full CEF Hamiltonian result in little difference at low temperatures to the expected results of just considering the ground state.

A model Hamiltonian can then be written down to describe the physics of the $4f$ sites in this material:

$$\begin{aligned} H_{4f} =& H_{CEF} - g_z(H) M_z H_z - B_2^2(\varepsilon_{xx} - \varepsilon_{yy}) O_2^2 - K_{B_{1g}} \langle O_2^2 \rangle O_2^2 \\ & - B_{xy} \varepsilon_{xy} P_{xy} - K_{B_{2g}} \langle P_{xy} \rangle P_{xy} \end{aligned} \tag{5.2}$$

The second term is the Zeeman effect from an applied magnetic field in the c-axis direction. It is multiplied by a field-dependent free parameter which accounts for demagnetization effects. The third term is the bilinear magnetoelastic coupling of the B_{1g} quadrupole operator O_2^2 ($J_x^2 - J_y^2$) to the corresponding lattice strain $\varepsilon_{B_{1g}} = \frac{1}{2}(\varepsilon_{xx} - \varepsilon_{yy})$, and the following term is a mean field quadrupole-quadrupole interaction term originating from the RKKY interaction mediated by the

conduction electrons. The same terms are allowed for the B_{2g} quadrupole $P_{xy} = \frac{1}{2}(J_y J_x + J_x J_y)$, which couples to $\varepsilon_{B_{2g}} = \varepsilon_{xy}$. The nonperturbative H_{CEF} describes the crystal electric field from the surrounding Ag atoms, and as previously stated produces a ground-state Γ_5 doublet with an excited singlet at $\Delta_1 = 14K$, with other excited states 50K and higher [3]. O_2^2, M_z, and P_{xy} map respectively to J_z, J_x, and J_y as Pauli pseudo-spin operators. Symmetry dictates that any of these magnetic or quadrupolar matrix elements between the ground state doublet and all excited singlets are zero. Thus this Hamiltonian (with zero applied strain) maps nearly exactly to a transverse field mean-field Ising Hamiltonian, the primary difference being the effect of thermally populating the excited states which provides an elevated background of the heat capacity above T_Q.

5.2 Experimental Methods

$TmAg_2$ single crystals were grown from a stoichiometric melt sealed in Ta crucibles, as detailed in section 2.1. These growths were annealed *in situ* at 80K below the melting point of $TmAg_2$ (1070K as measured from a differential scanning calorimeter) to increase crystal quality.

Resistivity measurements were performed in a 14T PPMS. Gold wires and silver paste (4929N) was used to contact the samples in the standard 4-point geometry. Samples were aligned with X-ray diffraction and then cut with a wire saw to obtain rectangular prism samples with (0 0 1) perpendicular to the main face of the sample. The crystals were polished to dimensions of roughly 2mm x 0.4mm x 0.06 mm to maximize the resistance signal. Many samples were measured, and a correlation was noted between the sharpness of the transition and the RRR of the sample indicating the crystal quality affected the phase transition. Resistivity data is shown here from a sample with a RRR of ~ 70.

Heat capacity measurements were performed in the same PPMS using a standard thermal relaxation technique. Apiezon N-grease was used to secure the sample to the sapphire platform. A correlation was also noted between the measured resistance metrics for sample quality and the sharpness of the phase transition signature in heat capacity, as well as the ratio of the magnitude of the critical feature to the non-critical background. Only the measurements of samples with the highest ratio of critical heat capacity to background are discussed in this chapter, and these samples were later used for the elastocaloric measurements.

For fitting the heat capacity of $TmAg_2$ in zero magnetic field as well as finite field, the previously mentioned Hamiltonian in Eq. 5.2 was self-consistently diagonalized to determine both the resulting energy spectrum as well as the order parameters M_z, O_2^2 and P_{xy}. All 13 CEF states for J=6 were considered. The strength of the mean field coupling as well as the field dependent coefficient $g_z(H)$ were treated as free parameters. "Built-in" B_{1g} strains were also treated as free parameters to simulate the disorder present in the lattice due to vacancies, which primarily manifests in broadening of the mean-field step of the heat capacity.

Elastocaloric measurements were performed as detailed in Section 2.3, and the experimental setup is depicted in Figure 2.3. A commerical Razorbill CS-100 strain cell was used to apply strain to the samples, and the samples were polished to be a similar size to the crystals used in resistivity measurements. The samples were secured between two sets of mounting plates using Stycast 2850FT Epoxy, and the mounting plates were screwed into the strain cell, as depicted in Figure 2.3. An AC voltage of 20V rms at 72 Hz was applied to the outer PZT stacks of the strain cell, which corresponded to applying an AC displacement of the sample of amplitude roughly 0.01% of its length. DC voltages were applied to both the outer set of PZTs and the inner PZT to reach a strain range of roughly 0.3% at low temperatures.

The temperature fluctuations in the sample induced by the AC strain were measured using a RuO_2 resistor/thermometer which was heat piped to the sample via a 50μm diameter gold wire, as shown in Figure 2.3. The gold wire was silver pasted to the sample as well as the back of the thermometer, to provide high thermal conductivity from the thermometer to the sample. The thermometer was polished to have dimensions of 150μm x 75μm x 20μm to reduce its heat capacity. The temperature signal was measured at the sum of this strain frequency and the thermometer excitation frequency, extracted using an SRS860 using the AC demodulation technique used in elastoresitivity measurements described in section 2.1.1 and in Ref [44]. To increase the signal to noise ratio the voltage from the thermometer was measured using a custom Wheatstone bridge in which the 3 other resistive components were identical resistors to the thermometer, and the bridge was thermally anchored to the cell, as detailed in section 2.3.

5.3 Results and Discussion

5.3.1 Heat Capacity

Here we describe the heat capacity measurements performed on $TmAg_2$, in terms of both the zero-field measurement which we show is consistent with a doublet sensitive to strain degrees of freedom, and also in terms of the magnetic field dependence of the signature of the phase transition, which we show is consistent with a mean-field spin 1/2 transverse field Ising phase boundary.

Heat capacity measurements were performed for several samples with different levels of disorder evident in the broadening of the phase transition. The least disordered is presented here. Data from 2 to 12K were collected in magnetic fields varying from 0T to 12T. Figure 5.1b displays the zero-field heat capacity, in which the ferroquadrupolar phase transition manifests in a mean-field step at 5K, consistent with a mean-field second-order phase transition involving a doublet. This signature is smeared however, and to attempt to explain this we simulated the heat capacity from a Hamiltonian which included "built-in" strains, as described in the caption. These values represent the potential macroscopic strains that can arise from securing the sample to a sapphire platform with a different thermal expansion, as well as from microscopic strains that can be induced via crystal

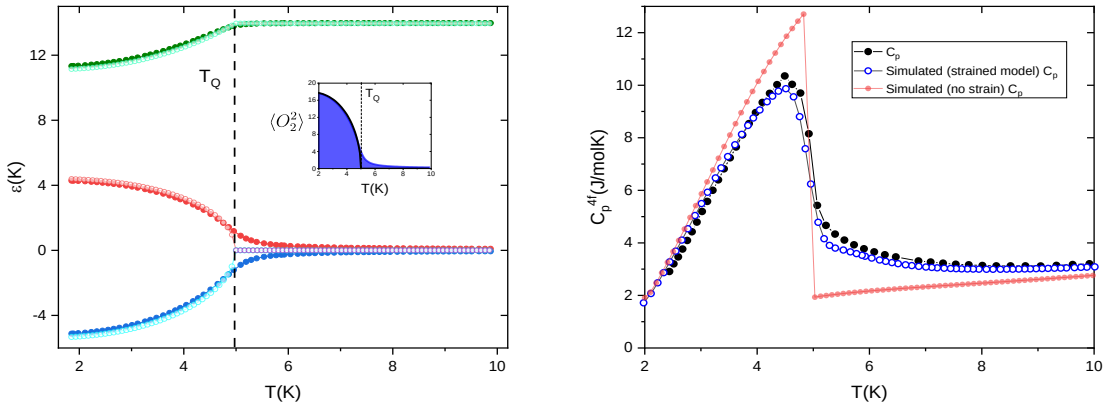

Figure 5.1: $4f$ **Heat capacity of $TmAg_2$ compared to simulations with "built-in" strains.** The left panel displays a schematic of the single-ion energy spectrum showing the lowest three CEF energy states of the 4f electronic multiplet that were simulated with a model Hamiltonian with previously determined parameters. Bold symbols show the energy eigenvalues from a simulation with an appropriate longitudinal strain of order 10^{-4} to simulate the broadening of the system's heat capacity (see main text). Open symbols show results of a simulation that doesn't incorporate an applied strain, such that the splitting of the Γ_5 ground-state doublet onsets at 5K. The inset displays the order parameter dependence on temperature for both unstrained (black line) and strained simulations. The right panel displays the measured zero-field heat capacity data for $TmAg_2$ (black dots), isolating the $4f$ electronic component of the heat capacity. This was done by subtracting the heat capacity of YAg_2, in which the Y^{3+} ion acts chemically identical to the Tm^{3+} ion but has an empty 4f shell. The blue symbols are simulated heat capacity results including three B_{1g} strains as a fit parameters. The phase transition temperatures in the simulations were determined by the mean-field interaction constants $B^2/C + K$, which were chosen so the system had a critical temperature $T_Q = 5K$. This simulated heat capacity is the linear combination: $0.634C_p(\varepsilon_1) + 0.23C_p(\varepsilon_2) + 0.136C_p(\varepsilon_3)$ where $\varepsilon_1 = 0.007\%$, $\varepsilon_2 = 0.1\%$, and $\varepsilon_3 = 0.7\%$. The results of a simulation featuring a Hamiltonian with no "built-in" strains, and consequently a sharp mean-field step, are shown in red.

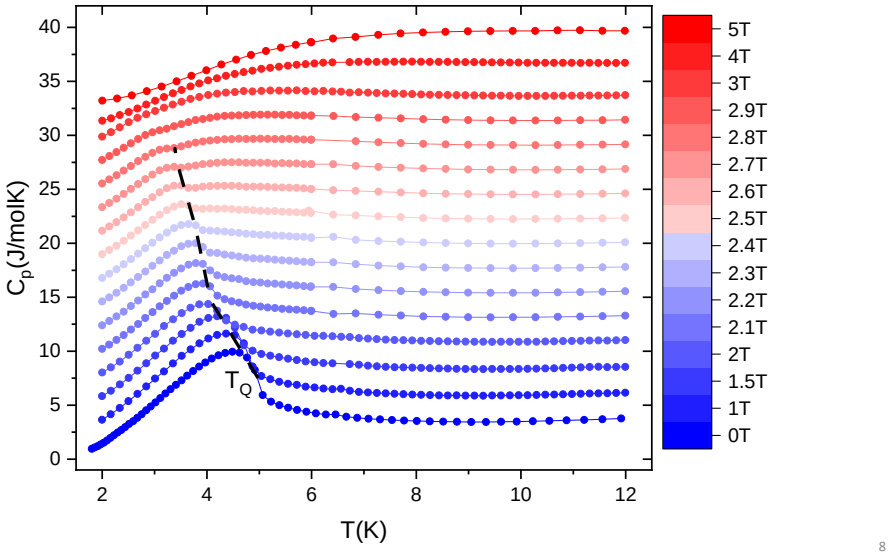

Figure 5.2: **Variation of the temperature dependence of the heat capacity with applied magnetic field.** Data are shown for fields ranging from 0-5T, with vertical offsets for clarity (no offsets for $H = 0T$). T_Q is marked by a black dotted line, showing its progressive suppression with increased magnetic field H_z.

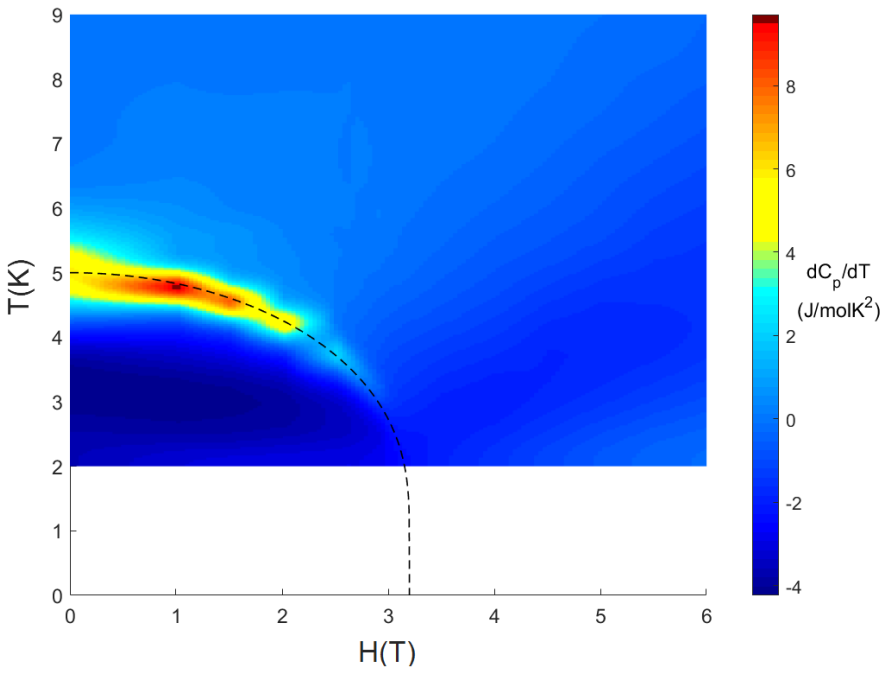

Figure 5.3: **Interpolated color map of the temperature derivative of the $4f$ heat capacity in the H-T plane.** The dotted line shows a mean-field transverse Ising fit of a phase boundary with $T_Q = 5K$ at zero field and $H_c = 3.1T$ at 0K.

imperfections/vacancies. These can be larger than 1% in theory, and so the values of the built-in strains that were chosen to accurately describe the data can be reasonably expected. The finer details of the strain values aside, this motivates thinking about the potentially significant effects of applying/inducing strain in this material. The simulated energy spectrum of the ground state and excited singlet are shown with and without these strain inputs in the left panel of Figure 5.1 as well.

The C_p data from 0T to 4T is shown in Figure 5.2, which shows a smooth suppression of T_Q with magnetic field, as seen by the dotted line serving as a guide to the eye. These traces (along with higher field traces) were interpolated in both field and temperature, and the numerical derivative was taken to create the color plot shown in Figure 5.3. The derivative marks the ferroquadrupolar phase transition quite well as a function of magnetic field down to around 3K, where the signature becomes too small in magnitude compared to the background to track accurately. The phase transition boundary is consistent with a mean-field spin 1/2 transverse field Ising phase boundary with $T_Q(0) = 5K$ and $H_c = 3.1T$. As the magnetic field was increased to progressively higher fields, a Schottkey feature became evident. This feature is consistent with an energy gap that evolved in magnetic field consistent with a doublet being separated by energy scales proportional to the magnetic field.

5.3.2 Elastocaloric Effect

In this section we explain how the elastocaloric experimental technique can sensitively probe ferroquadrupolar phase transitions as well as the strain derivatives of T_Q. We show and explain the results of this measurement with respect to $TmAg_2$ in Figure 5.3-5.6. We also demonstrate that the elastocaloric effect measures nematic/quadrupole-strain susceptibilities, and display the results of elastocaloric measurements which are sensitive to the B_{2g} quadrupole-strain susceptibility using offset strains and magnetic fields as tuning parameters, seen in Figure 5.7. We also discuss an experimental issue, namely contamination from the B_{1g} channel.

The AC elastocaloric technique, described in section 2.2 and Ref. [8], applies/induces an AC strain in the sample, and measures the corresponding temperature fluctuations. Briefly, in the proximity of a phase transition and given certain assumptions hold that are outlined in section 2.2, the amplitude of the temperature change will be proportional to the aspect of the critical heat capacity which is effectively shifted in temperature by applying a strain. It will also be proportional to the amount by which it is shifted (for small AC strains: $\frac{dT_Q}{d\varepsilon}$), and inversely proportional to the total heat capacity of the system.

Probing the ferroquadrupolar phase transition

As we will show in this section, the elastocaloric effect is a sensitive probe of the ferroquadrupolar phase transition in $TmAg_2$. Looking at Eq. 5.1, which is derived in Ref. [8], a phase transition which has strain dependent critical temperature $T_Q(\varepsilon)$ will result in a jump in the elastocaloric signature

Δ_{EC} given by:

$$\Delta_{EC} = \left(\frac{dT^-}{d\varepsilon}\right) - \left(\frac{dT^+}{d\varepsilon}\right) = \frac{dT_Q}{d\varepsilon}\left(\frac{C_p^{c-}}{C_p^{c-} + C_p^{nc}} - \frac{C_p^{c+}}{C_p^{c+} + C_p^{nc}}\right) \tag{5.3}$$

where $\frac{dT}{d\varepsilon}^{\pm}$ are the derivatives of the induced temperature change with respect to strain approaching the phase transition from the the disordered/ordered side. C_p^{c+} and C_p^{c-} are the heat capacities of the (strain dependent) critical degrees of freedom of the system right above and below the critical temperature, and C_p^{nc} is the background heat capacity that doesn't change through the phase transition (mainly the phonon contribution). For materials with prominent heat capacity features, like $TmAg_2$, seen in Figure 5.1, the elastocaloric effect should then manifest in a substantial change in $\frac{dT}{d\varepsilon}$ at the phase transition, proportional to $\frac{dT_Q}{d\varepsilon}$. The right-hand-side of Eq. 5.3 can be simplified assuming $C_p^{c+} = 0$ (as is the case for a mean-field step), resulting in:

$$\Delta_{EC} = \frac{dT_Q}{d\varepsilon}\frac{\Delta_{C_p}}{C_p^{tot}(T_Q)} \tag{5.4}$$

where Δ_{EC} represents the jump seen in the elastocaloric effect, $\Delta_{C_p} = C_p^- - C_p^+$, and C_p^{tot} is the total heat capacity approaching T_Q from the ordered state.

We applied this technique with a sample oriented such that the stress was applied along (1 1 0). This orientation induces B_{2g} strain and A_{1g} strain in the sample. Thus, when we consider the strain derivative in Eq. 5.4 that is extracted by the elastocaloric effect, the derivative with respect to both symmetry strains must be taken into account. By symmetry, the change in the phase transition temperature given a perturbative AC strain is applied in the presence of a finite DC strain is:

$$dT_Q(\varepsilon^{\mathbf{app}}) = B\frac{dT_Q}{d\varepsilon_{A_{1g}}}\varepsilon_{A1g}^{AC} + 2CD\varepsilon_{B_{2g}}^{DC}\frac{dT_Q}{d((\varepsilon_{B_{2g}})^2)}\varepsilon_{B_{2g}}^{AC} \tag{5.5}$$

where $\varepsilon^{\mathbf{app}}$ is the strain tensor quantity induced in the sample by the experimental setup, which has DC and AC strain components in both A_{1g} and B_{2g} symmetries: $A\varepsilon_{A_{1g}}^{DC} + B\varepsilon_{A_{1g}}^{AC}$, and $C\varepsilon_{B_{2g}}^{DC} + D\varepsilon_{B_{2g}}^{AC}$. A, B, C, and D are determined by the elastic constants of the material (see section 2.3) and proportional to the amplitude and amount of applied stress. As discussed in section 2.3, for stress applied along (1 1 0), the ratio between A and C, and B and D, is only weakly temperature dependent, as none of the relevant elastic constants for this symmetry channel soften (recall that $TmAg_2$ orders in the B_{1g} symmetry channel). Thus, we can assume that if we measure an elastocaloric signal at a fixed DC strain and subtract an equivalent measurement at zero applied strain, the result will be directly proportional to the second derivative of T_Q with respect to the potential transverse field $\varepsilon_{B_{2g}}$.

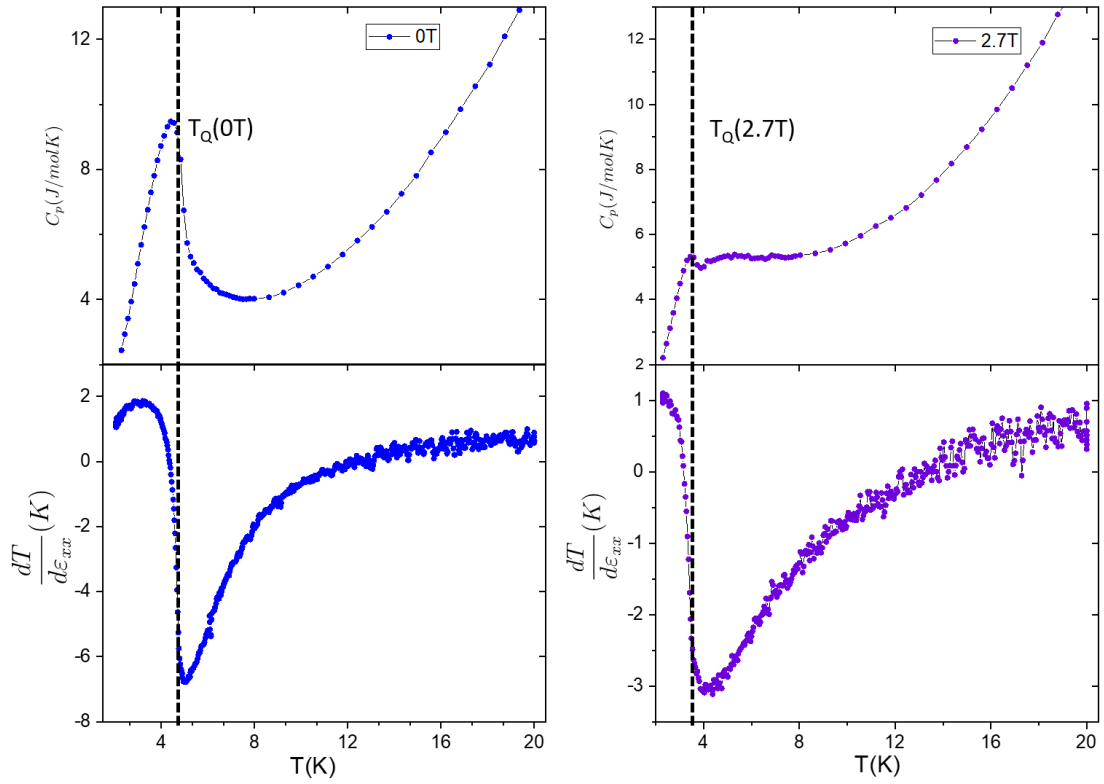

Figure 5.4: **Elastocaloric and heat capacity measurements of $TmAg_2$ at 0T (left panels) and 2.7T (right panels).** The top two graphs depict the heat capacity of $TmAg_2$ including the phonon contribution at 0T and 2.7T. The graphs below depict the elastocaloric effect via applying an AC stress along (1 1 0) for identical magnetic fields applied along the c-axis. The units of these graphs represent the temperature change in Kelvin of the thermometer attached to the sample per 100% strain applied to the sample. The actual peak-to-peak strain used for the measurements was closer to 0.01%. The phase transition, which occurs at temperatures denoted by the vertical black dashed lines, is marked by a discontinuity in the elastocaloric effect for both fields as described in the main text.

Magnetic field phase diagram and strain derivatives of T_Q

The top panels of Figure 5.4 shows the total heat capacity (including phonon background) for $TmAg_2$, 0T on the left and 2.7T on the right. Notice that the heat capacity signature of the phase transition at 2.7T is barely discernible above the background Schottkey anomaly, which is expected as the entropy has been shifted towards higher temperatures with the magnetic field induced gap in the doublet. Nonetheless as shown in the bottom two panels, the corresponding elastocaloric measurements feature relatively large signatures at the phase transition for both fields. This arises because the strain derivative described in Eq. 5.5 increases as a function of field, partially compensating for the field-induced loss of entropy of the critical degrees of freedom.

Figure 5.5 shows elastocaloric traces for fields from 0T (in blue) to 4T (in red). It is evident that the phase transition, marked by the jump (discontinuity), is smoothly suppressed as the magnetic field is increased, and the signature changes into a Schottkey-like bump for fields above the critical field, determined by this measurement to be $H_c = 3.32T \pm 0.1T$. The phase boundary is shown in the inset graph in Figure 5.5, and it aligns with the previous phase diagram inferred from heat capacity measurements (Figure 5.4). Note that the signature of the phase transition remains large right up to near the critical field, allowing a more precise determination of the phase boundary than possible with heat capacity. Only the probe's base temperature of 2.3K prevented observation of the phase transition to yet lower temperatures in the immediate proximity of the critical field H_c.

Figure 5.6 depicts the B_{2g} component of $\frac{dT_Q}{d\varepsilon}$ as a function of magnetic field, inferred through the observed jumps in elastocaloric and heat capacity measurements at identical fields, then found by rearranging Eq. 5.4. Each data point is obtained from a measurement which was done at the same finite strain $\varepsilon^{DC}_{B_{2g}}$, and by subtracting the zero-strain elastocaloric measurement at that field (zero-strain measurements were approximated/found via the method described in the next subsection), a quantity proportional to $\varepsilon^{DC}_{B_{2g}}$ multiplied by the quadratic coefficient of T_Q with respect to ε_{xy} was isolated (see right most term of Eq. 5.5). These are the (black) symbols plotted in Figure 5.6. The errors depicted arise from the errors in estimating the heat capacity ratio as well as the magnitude of the elastocaloric jump. The red line is a fit following the expected form for the derivative of T_Q with respect to a transverse field (B_{2g} strain) in a spin 1/2 mean-field Ising model as a function of an orthogonal transverse field, in this case magnetic field (see section 1.6.3).

Probing the nematic susceptibility in field

As shown via free energy arguments made in section 2.3, the elastocaloric effect is also a sensitive probe of fluctuations which couple to the induced strain that the sample is experiencing due to externally applied stresses. In particular, as explained in section 2.3, for a nematic/quadrupole-strain susceptibility of the material, the elastocaloric effect in the disordered phase will measure a signal (denoted $\left(\frac{dT}{d\varepsilon}\right)_{sus}$) proportional to the strain multiplied by the temperature derivative of a

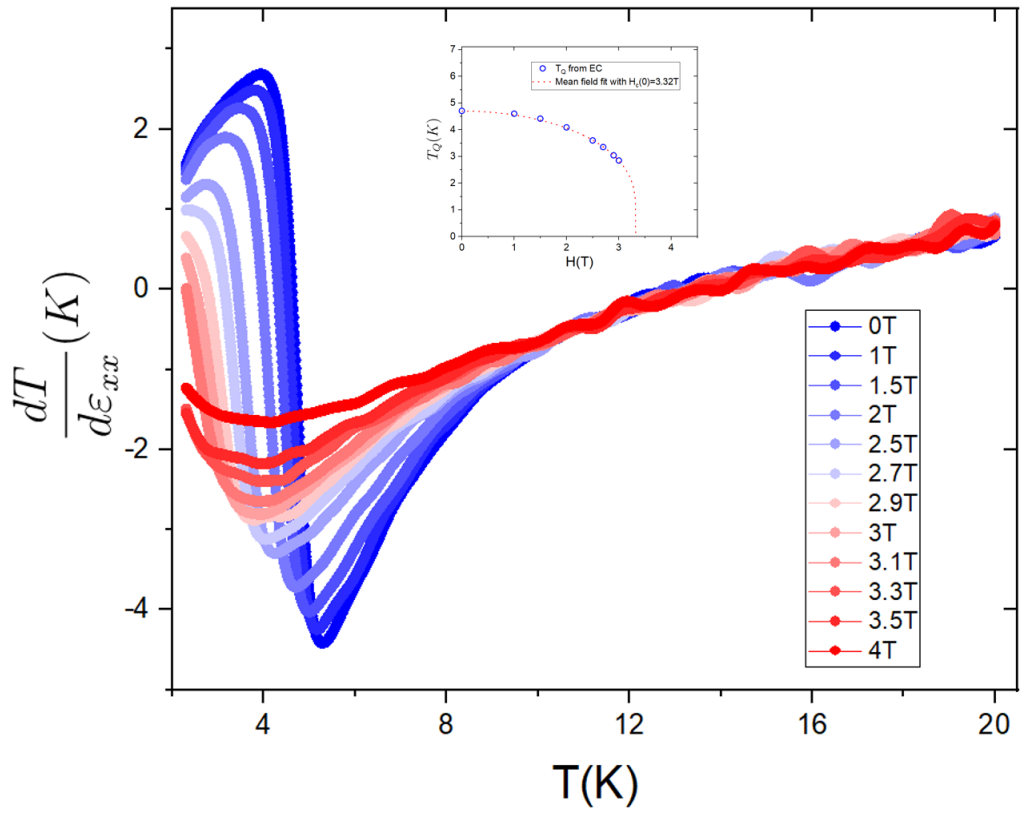

Figure 5.5: **Temperature dependence of the elastocaloric effect for different magnetic fields.** Elastocaloric data, measured while applying an AC stress along (1 1 0) while sweeping temperature from 20K to 2.3K, is plotted for magnetic fields applied along the c-axis from 0T (blue) to fields above the critical field of $3.32T \pm 0.1T$ (red). The ferroquadrupolar phase transition manifests in jumps in the elastocaloric traces, and the H-T phase boundary obtained by these signatures is plotted in the inset graph. The red dashed line in the inset is a mean-field transverse field Ising boundary with $T_Q(0T) = 4.8K$ and $H_c(0K) = 3.32T$. To the lowest temperatures measured in this study, the phase boundary follows mean-field expectations.

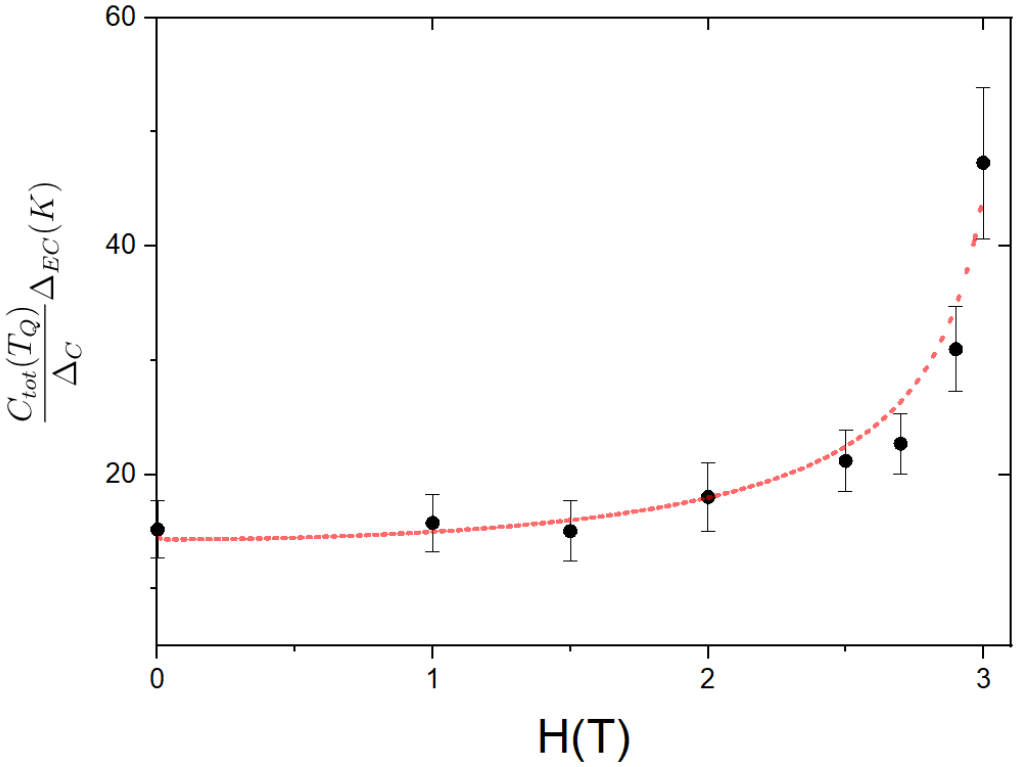

Figure 5.6: **Strain derivative of T_Q with respect to ε_{xy} as a function of magnetic field.** The black symbols are obtained by taking the ratio of the magnitude of the elastocaloric jump (Δ_{EC}) at the phase transition over the magnitude of the corresponding jump of the heat capacity, and multiplying by C_p^{tot}. These jumps are measured at finite strain, and the zero-strain jump is subtracted to obtain just the part proportional to the second derivative of T_Q with respect to $\varepsilon_{B_{2g}}$, as described in the text. The error bars represent the errors from extracting the magnitudes of the jumps in the elastocaloric effect and the heat capacity. These errors were estimated by using many linear fits of the quantities below and above the phase transition temperature, and extracting the range of the differences between the fits extrapolated to the phase transition temperature. The data points representing the strain derivatives shown are positive because the offset strain applied was compressive ($\sim -0.25\%$), and it multiplied the second derivative $\frac{d^2T_Q}{d\varepsilon^2_{B_{2g}}}$, which is negative since B_{2g} strain functions as a transverse field. The red dashed line is a fit from Eq. 1.49, which comes from solving the transverse-field Ising model for the derivative of the phase transition temperature as a function of the orthogonal transverse field. The measured values are consistent with this mean-field model.

nematic susceptibility (of the symmetry channel of the induced strain):

$$\left(\frac{dT}{d\varepsilon}\right)_{sus} = -\frac{T}{C_p}\lambda\varepsilon\frac{d\chi_N}{dT} \tag{5.6}$$

where λ is the bilinear coupling constant between the induced strain and the corresponding quadrupole, and χ_N is the nematic/quadrupole-strain susceptibility in the same symmetry channel as the applied strain.

In the case of the elastocaloric measurements on $TmAg_2$ that appear in this work, the relevant nematic/quadrupole-strain susceptibility that is measured is actually the B_{2g} susceptibility. The degrees of freedom of the ground state non-Kramer's doublet in $TmAg_2$ allow the analogous B_{2g} terms to be included in the $4f$ Hamiltonian just as the B_{1g} order parameter terms which were already included (see last two terms in Eq. 5.2), and so, as discussed in section 1.5, a Curie-Weiss form can be expected for both the B_{1g} and B_{2g} quadrupole-strain susceptibility.

The left panel of Figure 5.7 displays the temperature dependence of $\varepsilon^{DC}\frac{d\chi_{B_{2g}}}{dT}$ in magnetic fields from 0T to 4T. These traces were extracted from elastocaloric measurements performed at a fixed strain ε^{DC}. The dotted lines represent fits from the expected expression for a mean-field susceptibility for an Ising model with a transverse field being applied that is proportional to the applied magnetic field. In the particular case for the B_{2g} quadrupole-strain susceptibility of this material, this is governed by the expression (see section 1.6.2):

$$\varepsilon^{DC}_{B_{2g}}\frac{d\chi_{B_{2g}}}{dT} = \frac{C_p}{T}\left(\frac{dT}{d\varepsilon}\right)_{sus} = B^2_{xy}\varepsilon^{DC}_{B_{2g}}\frac{d}{dT}\left(\frac{\tanh\left(\frac{\Delta_H}{T}\right)}{T - T^*_{B_{2g}}\tanh\left(\frac{\Delta_H}{T}\right)}\right) \tag{5.7}$$

where B_{xy} is the bilinear magnetoelastic coupling between P_{xy} and ε_{xy}, Δ_H is the gap induced in the doublet by the magnetic field, and $T^*_{B_{2g}}$ is the effective Weiss temperature which arises from the mean-field interactions between local B_{2g} quadrupoles. The dotted lines are provided from this expression keeping $T^*_{B_{2g}} = 2.6K$ fixed, as well as fixing Δ_H to be proportional to field such that $\Delta_H = 1.6 * H_z(T)$, close to the expected 5/3.3 ratio expected given by the critical temperature being $T_Q(0) = 5K$ and the critical field measured to be $H_c = 3.3T$. However the multiplying constant, $C = B^2_{xy}\varepsilon^{DC}_{B_{2g}}$, increased in these fits with field, almost doubling from the 0T value at 4T. Similarly for fits which C was held constant, $T^*_{B_{2g}}$ nearly doubled from its value at 0T to its value at 4T to accurately map to the data. This is indicative that more degrees of freedom are potentially necessary to explain this data qualitatively, or perhaps that the energy scales of the mean-field interaction in the B_{2g} channel increase as field is increased. Nonetheless at a quantitative level, the elastocaloric effect in the disordered phase of $TmAg_2$ is clearly explained via the quadrupole-strain susceptibility obtained from a transverse-field Ising Hamiltonian, with interactions between B_{2g} quadrupoles mediated by conduction electrons at a similar energy scale as was inferred for the B_{1g} mean-field interaction. The B_{1g} interaction was proposed to be $T^*_{B_{1g}} \sim 3K$ [3] from previous

elastic softening and magnetic susceptibility measurements.

Strain dependence of the susceptibility term

The right panel of Figure 5.7 illustrates the DC strain dependence of the right hand side of Eq. 5.6 for elastocaloric data at 0T. The black data set in the main figure is the trace for which the strain induced in the sample is closest to zero-strain, based on Eq. 5.6. As compressive strain is applied, the elastocaloric amplitude becomes larger and negative, varying linearly with strain at all temperatures. The signal switches sign as tensile strain is applied, indicating Eq 5.6 accurately models the response of the elastocaloric effect in the disordered phase. The green trace which corresponds to $\varepsilon_{app}^{DC} = -0.25\%$, (where this is defined as the displacement of the sample along (1 1 0) divided by the original length of the sample) actually was measured with 0V applied to the PZTs of the strain cell, indicating that this is approximately the thermal mismatch strain between $TmAg_2$ and the Ti body of the cell. This thermal offset strain ε^{DC} was the value that all of the previously discussed data was collected at.

The inset graph of the right panel of Figure 5.7 shows the DC strain dependence of T_Q at 0T as measured by the temperature at which the jump occurred. It implies a small positive linear dependence of T_Q on the applied strain (0.3K/ % strain), indicating that the available strain range was too small to see noticeable quadratic effects from B_{2g} strain, and that this change in T_Q arises instead from A_{1g} strain.

Potential contamination from B_{1g} strains

Because the elastocaloric effect does not measure a symmetry-decomposed quantity, contamination from different strain symmetry channels cannot be controlled as accurately, as, for example, in the elastoresistivity technique. For instance if the sample were to be misoriented in the ab plane such that the applied stress was not completely applied along (1 1 0), a B_{1g} strain component would be induced, and a corresponding temperature fluctuation would arise from the derivative of the B_{1g} quadrupole-strain susceptibility term (potentially a much larger inherent effect than in the B_{2g} channel). We remark simply that we cannot rule this out as being the main cause of the susceptibility-like terms seen in the disordered phase in the present measurements. Future experiments that deliberately induce B_{1g} symmetry strains will enable a more conclusive interpretation of the origin of the observed behavior. We note for now, however, that all conclusions based off the strain, temperature, and field dependence of the measured effect remain valid.

5.3.3 Resistivity

Having established that magnetic fields can induce a quantum phase transition in $TmAg_2$, we proceed now to explore the electrical resistivity across the H-T phase diagram. Resistivity measurements

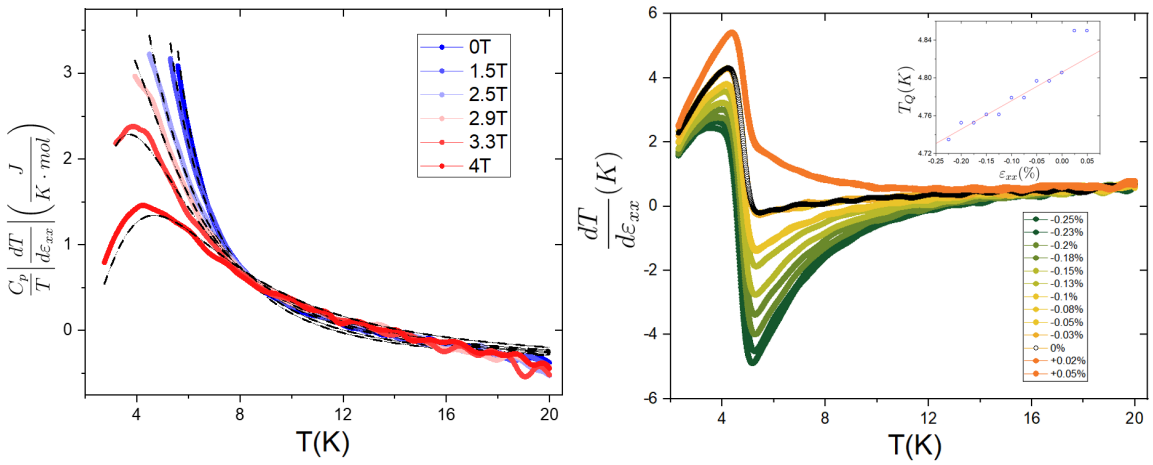

Figure 5.7: **The B_{2g} quadrupole-strain susceptibility as probed by the elastocaloric effect.** The left panel displays elastocaloric data, normalized to display the strain multiplied by the temperature derivative of the nematic susceptibility, measured at a fixed DC strain with different magnetic fields. The dotted lines are the expected fit for the susceptibility in an Ising model with a transverse field applied, although the proportionality constant is allowed to vary and almost doubles from its value at 0T to its value at 4T. The effective Weiss temperature for this susceptibility is found to be $T^*_{B_{2g}} = 2.6K$, although if the proportionality constant is fixed then this quantity will vary in the fits from 2 to 3K as field is increased. The right panel displays the temperature dependence of the elastocaloric effect as different DC strains are induced in the sample. The black dataset represents the data which is set to a strain closest to zero-strain, yellow-green traces represent compressive strain conditions, and the orange data is collected in tensile strain. The effect is linear with strain at all temperatures for this strain range, as expected from Eq. 5.6. Notice that the magnitude of the jump at 5K varies significantly with offset strain, this is expected as well from Eq. 5.5. The inset graph displays T_Q extracted from the jumps as a function of DC strain, which exhibits a linear dependence of 0.3K/% of applied strain.

were performed in temperature ranges from 1.8K to 15K, and magnetic fields from 0T to 8T. Figure 5.8 displays resistivity vs. temperature data in select representative magnetic fields from 0T (blue, bottom) to 8T (red top), vertically offset for clarity. The zero-field resistivity data marks the phase transition with a kink at 5K, and the signature of the phase transition is seen more clearly in $\frac{d\rho}{dT}$, resembling the signature in the heat capacity, as anticipated from standard Fisher-Langer arguments [60], but smeared more, perhaps indicative of elastoresistivity contributions from built in strains (see Chapter 3 for elastoresistivity discussion). The quasi-linear behavior of the resistivity above 5K is attributed to electron-phonon and potentially also inelastic $4f$ scattering. As the magnetic field is increased the signature of the phase transition in the resistivity becomes smaller, similar to the heat capacity, and the temperature dependence below T_Q flattens out. This is consistent with loss of quadrupole-disorder scattering from the appearance of the order parameter $\langle O_2^2 \rangle$, which, analogous to the discussion in Ref. [60] concerning magnetic order parameters, should manifest as $a_o(1 - b\langle O_2^2 \rangle^2)$, and the presence of a residual resistivity due to elastic scattering from impurities.

For magnetic fields above the critical field, the resistivity exhibits metallic behavior, but more notably the temperature dependence can be described by an integral of a Schottkey term, with a gap proportional to the magnetic field. This is precisely the behavior one would expect for the internal energy of the system considering the low temperature $4f$ degrees of freedom, and is suggestive that a relation between $\frac{d\rho}{dT}$ and C_p exists beyond just in the immediate proximity of the phase transition.

The left panel in Figure 5.9 displays a color map in the H-T plane of the heat capacity, and the right panel displays a color map of $\frac{d\rho}{dT}$, both obtained by by linear interpolation in between closely-spaced data sets. By inspection these diagrams are quite similar, not only in the proximity of the phase transition (shown by a dotted line serving as a guide to the eye), but also in the region of phase space with higher magnetic field and higher temperatures, in which both quantities exhibit a similar Schottkey-like feature. Near to the phase transition a Fisher-Langer type relation could potentially be expected to be relevant as the critical degrees of freedom dominate the transport, but such an argument clearly does not apply in the rest of the phase diagram where this quasi-proportionality is nevertheless still seen. We speculate that for inelastic scattering from $4f$ electrons, the associated field-dependent gaps in the CEF energy spectrum appear in the interaction matrix elements between the conduction and $4f$ electron scattering processes. These same energy gaps of course appear in the heat capacity due to Schottkey terms, and in both cases will have a field dependence similar to that which is observed.

Of course the regime of principal interest is for fields and temperatures close to the putative field tuned quantum critical point near $H_c \sim 3.1T$. Inspection of the resistivity data shown in Figure 5.8 reveals a finite slope of the resistivity down to the lowest temperatures measured close to this field (pink data). However measurements to conisderably lower temperatures will be required to determine whether this behavior is in anyway anomalous or otherwise indicative of quantum criticality. Unfortunately, these measurements were not possible during the timescale of this work,

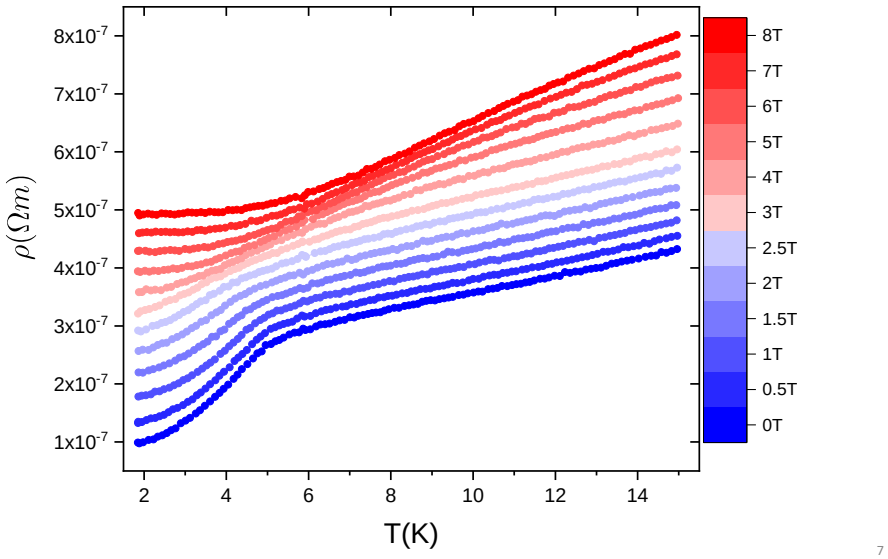

Figure 5.8: **Evolution of the temperature dependence of the resistivity of $TmAg_2$ as a function of magnetic field.** Resistivity data are shown for representative fields from 0T-8T, although much finer field spaced data were collected and then used to construct the interpolated color plot shown in Figure 5.9. As described in the main text, the signature of the phase transition in the resistivity is smeared and reduced in temperature as magnetic field increases. The temperature dependence of the resistivity flattens out progressively below the transition as the field gets close to the critical field. Above the critical field the temperature dependence of the resistivity is seemingly described by the integral of Schottkey terms (see main text and Figure 5.9).

and are clearly indicated for the future. We remark, however, that our findings (Figure 5.9) of clear signatures of energy gaps in the CEF spectrum that are tuned by field appearing in the resistivity will necessitate caution in the interpretation of such data, especially if power-law fits are attempted to higher temperatures.

5.4 Conclusion

We have established through elastocaloric and heat capacity measurements that the H-T phase diagram of $TmAg_2$ is consistent with a transverse-field Ising model, with magnetic field along the c-axis acting as a transverse field to the B_{1g} quadrupolar order parameter. Analysis of the strain derivatives of T_Q as obtained from the elastocaloric effect and heat capacity also show that B_{2g} strain is consistent with mapping onto the other orthogonal transverse field. This motivated the study of the thermodynamic susceptibilies and transport in the proximity of the completely suppressed

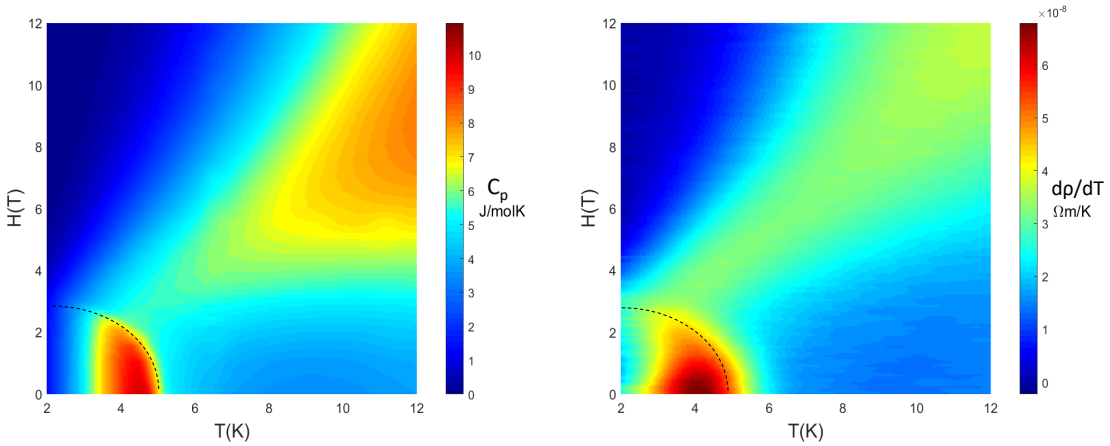

Figure 5.9: **Interpolated color-scale plots of both C_p (left panel) and $\frac{d\rho}{dT}$ (right panel) in the H-T plane.** Both the shape of the phase transition and the signature of a Schottkey-like anomaly appear very prominently and similarly in both quantities.

ferroquadrupolar phase transition. No obvious signatures of quantum criticality were seen in either the B_{2g} quadrupole-strain susceptibility or the resistivity there, at least over the temperature range considered. Rather, the quadrupole-strain susceptibility followed the expected form for a susceptibility in an Ising model with magnetic field acting as an orthogonal transverse field over the entire field and temperature range studied (although the potential field dependence of B_{xy}/K_{xy} perhaps motivates further experiments). The resistivity, or specifically $\frac{d\rho}{dT}$, followed a quasi-proportionality with the heat capacity, suggesting thermodynamic quantities dominated the scattering over any potential quantum critical scattering in temperatures down to 1.8K. Further lower-temperature measurements are clearly motivated, performed using even higher quality crystals, to resolve whether any consequences of quantum criticality are evident in transport or thermodynamic properties. This far, for the temperature range considered, no such signatures were evident.

Despite the apparent absence of obvious signatures of quantum criticality affecting the electronic transport, we nevertheless want to emphasize the novelty of both the application of the elastocaloric effect on a $4f$ intermetallic material, as well as investigating $TmAg_2$ in the context of nematic quantum criticality. The AC elastocaloric effect has recently been developed and applied to investigate an iron-based superconductor. We have shown with this work that it is also a sensitive probe of low-temperature ferroquadrupolar phase transitions, and uniquely suited to study materials with

couplings to anti-symmetric strains. For $TmAg_2$ it has shown that both magnetic field and B_{2g} strains can serve as tuning parameters to obtain quantum phase transitions. A strain-tuned quantum phase transition in $TmAg_2$ would be the first known case of a QCP tuned by *anti-symmetric* strain, and motivates more strain-based measurements and developing different experimental setups which allow larger strains.

Chapter 6

Conclusion

In this thesis we have discussed and probed thermodynamic and transport properties of two $4f$ intermetallic systems, $YbRu_2Ge_2$ and $TmAg_2$. Both of these materials have been proposed to undergo ferroquadrupolar phase transitions in the B_{1g} symmetry channel at 10.2K and 5K respectively. The B_{1g} elastoresistivity and low-temperature X-ray measurements of $YbRu_2Ge_2$ featured in Chapter 3, and the strain-tuning of the phase transition of $TmAg_2$ featured in Chapter 5, establishes that this is the case for both of these materials. We investigated both theoretically and experimentally in detail how both of these ferroquadrupolar phase transitions can be/were suppressed towards a quantum phase transition at 0K through the application of a magnetic field applied along the c-axis at $\sim 21.3T$ and $\sim 3.1T$ for $YbRu_2Ge_2$ and $TmAg_2$ respectively. The quadrupole-strain susceptibilities were investigated throughout their respective H-T phase diagrams (with two different complimentary probes), revealing higher-order octupolar couplings in $YbRu_2Ge_2$, and a transverse-field mean field Ising susceptibility for the quadrupole-strain susceptibility of $TmAg_2$. Resistivity measurements indicated potential signatures of quantum criticality in the proximity of the field-suppressed ferroquadrupolar phase transition for $YbRu_2Ge_2$, and an quasi-proportionality of the temperature derivative of the resistivity to the heat capacity in $TmAg_2$.

Although this thesis has generally emphasized the similarities of these materials, these measurements help clarify some of the differences between them. The elastoresisitivty and resistivity measurements suggest the $4f$ quadrupoles couple more strongly to the conduction electrons in $YbRu_2Ge_2$ at low temperatures than in $TmAg_2$. This is to be expected, as the weak Kondo effect seen in $YbRu_2Ge_2$ at higher temperatures indicates substantial interactions between the conduction electrons and the $4f$ sites. Also the quasi-quartet ground state of the $4f$ electrons in $YbRu_2Ge_2$ truly does manifest in higher order multipolar couplings that profoundly affect the magnetic field phase diagram of this material, unlike the case for the more simple non-Kramer's doublet of the $4f$ electrons in $TmAg_2$.

More generally this work has investigated $4f$ intermetallic materials in an original and exciting

context. $4f$ intermetallic materials, although studied in detail in the 70's and 80's mainly for the properties of their magnetic phase diagrams, also provide a much less recognized avenue to investigate topics pertaining to modern condensed matter physics problems, particularly understanding quantum criticality in metals. This was demonstrated in this work, both theoretically by mapping the low-temperature $4f$ Hamiltonians of $TmAg_2$ and $YbRu_2Ge_2$ to the paradigmatic model that undergoes a quantum phase transition, the mean-field transverse Ising model, and also experimentally investigated by using magnetic field to completely suppress the ferroquadrupolar phase transitions to 0K. These Hamiltonians were shown to accurately describe thermal properties of these materials, at least over the temperature ranges investigated, setting the stage for further measurements to yet lower temperatures in the proximity of putative nematic QCPs. Any such future measurements, coupled with the measurements featured in this work, will be able to be attribute any deviations to quantum critical degrees of freedom with confidence.

This work has also developed and applied two different experimental approaches to measuring nematic susceptibilities. Both the AC elastocaloric effect and AC elastoresistivity technique are recently developed novel strain based measurements. Previously they had been almost exclusively applied to the iron-based superconductors, and it was unclear if experiments designed to measure these quantities would observe significant signals in materials where the symmetry breaking arises from local rather than itinerant electronic degrees of freedom. The measurements in this thesis conclusively showed that these techniques are sensitive to local quadrupolar degrees of freedom of these materials, in effect marrying the terms quadrupole-strain and nematic, and showed the power of strain-based techniques in probing local multipolar degrees of freedom in general.

Although not discussed in this work, measurements of $Tm_{1-x}Y_xAg_2$ (preliminary) and $Yb(Ru_{1-x}Rh_x)_2Ge_2$ [61] indicate that the ferroquadrupolar phase transitions are suppressed to 0K for relatively small substitutions. Thus, chemical substitution is likely to be another different effective tuning parameter for tuning towards nematic quantum criticality, motivating the use of the techniques and analysis performed on the parent compounds in this thesis to investigate these chemically substituted samples as well. The precise mechanism by which the ferroquadrupolar order is suppressed in these doped material systems has yet to be definitively established. However, local strains arising from the substitution sites can act as random fields on the $4f$ sites, potentially invoking other statistical mechanics models in describing the thermodynamic and transport properties of these chemically substituted materials.

Bibliography

[1] Bohmer AE et al. (2014) Nematic susceptibility of hole-doped and electron-doped $BaFe_2As_2$ iron-based superconductors from shear modulus measurements **Phys. Rev. Lett. 112 047001**

[2] Morin P, Schmitt D (1990) Quadrupolar interactions and magneto-elastic effects in rare earth intermetallic compounds **Handbook of Ferromagnetic Materials, Vol. 5 1990, 1-132**

[3] Morin P, Rouchy J (1993) Quadrupolar ordering in tetragonal $TmAg_2$ **Phys Rev B 48, 256**

[4] Jeevan HS, Geibel C, Hossain Z (2006) Quasiquartet crystal-electric-field ground state with possible quadrupolar ordering in the tetragonal compound $YbRu_2Ge_2$ **Phys Rev B 73 020407(R)**

[5] Dresselhaus M. and Dresselhaus G. Group Theory: Application to the Physics of Condensed Matter **Springer Berlin Hidenberg 2010**

[6] Koster G.F. et al. The Properties of the Thirty-Two Point Groups **The MIT Press; First Edition edition (December 15, 1963)**

[7] Karahasanovic U. and Schmalian J. Elastic coupling and spin-driven nematicity in iron-based superconductors **Phys. Rev. B 93, 064520 (2016)**

[8] Ikeda M et al. AC elastocaloric effect as a probe for thermodynamic signatures of continuous phase transitions **Review of Scientific Instruments 90, 083902 (2019)**

[9] Strecka J. and Jascur M. A brief account of the Ising and Ising-like models mean-field, effective field and exact results **arXiv:1511:.03031v2**

[10] Tadao Kasuya A Theory of Metallic Ferro- and Antiferromagnetism on Zener's Model **Progress of Theoretical Physics, Volume 16, Issue 1, July 1956, Pages 45–57**

[11] Rosenberg E. et al (2019) Divergence of the quadrupole-strain susceptibility of the electronic nematic system $YbRu_2Ge_2$ **Proc Natl Acad Sci USA 116 (15) 7232-7237**

[12] Fradkin E, Kivelson SA, Lawler MJ, Eisenstein JP, and Mackenzie AP (2010) Nematic Fermi Fluids in Condensed Matter Physics **Annu. Rev. Condens. Matter. Phys. 1, 153-178**

[13] Fisher IR, Degiorgi L, and Shen ZX (2011) In-plane electronic anisotropy of underdoped "122" Fe-arsenides revealed by measurements of detwinned single crystals **Rep. Prog. Phys 74, 124506** and references therein.

[14] Fernandes RM, and Schmalian J (2012) Manifestations of nematic degrees of freedom in the magnetic, elastic, and superconducting properties of the iron pnictides **Supercond. Sci. Technol. 25, 084005** and references there-in.

[15] Chu JH, Kuo HH, Analytis JG, Fisher IR (2012) Divergent Nematic Susceptibility in an Iron Arsenide Superconductor **Science Vol. 337 Issue 6095 pp 710-712**

[16] Fernandes RM, Chubukov AV, and Schmalian J (2014) Nematic order in iron superconductors-who is in the driver's seat? **Nat. Phys Vol. 10 pp 97-104**

[17] Bohmer AE, and Meingast C (2016) Electronic nematic susceptibility of iron-based superconductors **C. R. Physique 17, 90**, And references there-in.

[18] Ando Y, Segawa K, Komiya S, and Lavrov AN (2002) Electrical resistivity anisotropy from self-organized one dimensionality in high-temperature superconductors **Physical Review Letters 88, 137005**

[19] Daou R et al. (2010) Broken rotational symmetry in the pseudogap phase of a high-T-c superconductor **Nature 463, 519-522**

[20] O. Cyr-Choiniere et al. (2015) ,Two types of nematicity in the phase diagram of the cuprate superconductor $YBa_2Cu_3O_y$ **Phys. Rev. B. 92, 224502**

[21] Chang J et al. (2016) Nernst effect in the cuprate superconductor $YBa_2Cu_3O_y$: Broken rotational and translational symmetries **Nature Communications 7, 11494**

[22] Achkar AJ et al. (2016) Nematicity in stripe-ordered cuprates probed via resonant x-ray scattering, **Science 351, 576-578**

[23] Sato Y et al. (2017) Thermodynamic evidence for a nematic phase transition at the onset of the pseudogap in $YBa_2Cu_3O_y$, **Nature Phys. 13, 1074**

[24] Wu J, Bollinger AT, He X, and Bozovic I (2017) Spontaneous breaking of rotational symmetry in copper oxide superconductors, **Nature 547, 7664**

[25] Ramshaw BJ et al. (2017) Broken rotational symmetry on the Fermi surface of a high-T-c superconductor **npj Quantum Materials 2, 8**

[26] Murayama H et al. (2018) Diagonal Nematicity in the Pseudogap Phase of $HgBa_2CuO_{4+d}$ **arXiv:1805.00276**

[27] Lederer S, Schattner Y, Berg E, and Kivelson SA (2015) Enhancement of superconductivity near a nematic quantum critical point **Phys. Rev. Lett. 114, 097001**

[28] Lederer S, Schattner Y, Berg E, and Kivelson SA (2017) Superconductivity and non-Fermi liquid behavior near a nematic quantum critical point **PNAS 114, 4905**

[29] Vojta (2009) Lattice symmetry breaking in cuprate superconductors: stripes, nematics, and superconductivity **Adv. in Phys. Vol. 58 pp 699-820**

[30] Lawler MJ et al. (2010) Intra-unit-cell electronic nematicity of the high-Tc copper-oxide pseudogap states **Nature Vol. 466 pp 347-351**

[31] Maharaj A, Rosenberg E, Hristov A, Berg E, Fernandes RM, Fisher IF, Kivelson SA (2017) Transverse fields to tune an Ising-nematic quantum phase transition **Proc Natl Acad Sci USA 1712533114**

[32] Kosaka M et al. (1998) Quadrupolar ordering and magnetic properties of tetragonal $TmAu_2$ **Phys Rev B 48, 58, 6339**

[33] Morin P, Kazei Z, Lejay P (1999) Quadrupolar couplings and magnetic phase diagrams in tetragonal $TmAu_2$ **J Phys Condens Matter 11, 1305-1319.**

[34] Takimoto T, Thalmeier P (2008) Theory of induced quadrupolar order in tetragonal $YbRu_2Ge_2$ **Phys Rev B 77, 045105**

[35] Jeevan HS, Adroja DT, Hillier AD Hossain Z, Ritter C, Geibel C (2011) Muon spin relaxation and neutron diffraction investigations of quadrupolar and magnetically ordered states of $YbRu_2Ge_2$ **Phys Rev B 84, 184405**

[36] Gehring GA and Gehring KA (1975) Co-operative Jahn-Teller effects **Reports on Progress in Physics Vol. 38**

[37] Kuo HH, Chu JH, Palmstrom JC, Kivelson SA, Fisher IR (2016) Ubiquitous signatures of nematic quantum criticality in optimally doped Fe-based superconductors **Science Vol. 352 Issue 6288 pp 958-962**

[38] Sablik M and Levy PM (1978) Anisotropy from quadrupole scattering in magnetically ordered rare-earth compounds **Journal of Applied Physics 49, 2171**

[39] Friederich A and Fert A (1974) Electron Scattering by the Electronic Quadrupole Moment of Rare-Earth Impurities **Phys. Rev. Lett. 33 1214**

[40] Shapiro MC, Hristov AT, Palmstrom JC, Chu JH, Fisher IF (2016) Measurement of the B_{1g} and B_{2g} components of the elastoresistivity tensor for tetragonal materials via transverse resistivity configurations **Rev Sci Inst Vol 87, Issue 6**

[41] Kuo HH, Shapiro MC, Riggs SC, and Fisher IR (2013) Measurement of the elastoresistivity coefficients of the underdoped iron arsenide $Ba(Fe_{0.975}Co_{0.025})_2As_2$ **Phys. Rev. B 88, 085113** [9 pages]

[42] Shapiro MC, Hlobil P, Hristov AT,. Maharaj AV, and Fisher IR (2015) Symmetry constraints on the elastoresistivity tensor **Phys. Rev. B 92, 235147**

[43] Palmstrom JC et al. (2017) Critical divergence of the symmetric (A_{1g}) nonlinear elastoresistance near the nematic transition in an iron-based superconductor **Phys Rev B 96.205133**

[44] Hristov AT, Palmstrom JC, Straquadine J, Merz T, Hwang H, Fisher IR (2018) Measurement of Elastoresistivity at Finite Frequency by Amplitude Demodulation **arXiv:1803.01909**

[45] Riggs SC et al. (2015) Evidence for a nematic component to the hidden-order parameter in URu_2Si_2 from differential elastoresistance measurements **Nature Communications volume 6, Article number: 6425**

[46] Jeevan HS (2010) Crystal Growth and Investigation of $CeCu_2Si_2$ and $YbRu_2Ge_2$: Competition/Co-existence of Superconducting, Dipolar and Quadrupolar order **core.ac.uk**

[47] Bouvier et al. (1996) Anomalous low-temperature magnetic behaviour in $DyRu_2Si_2$ and $DyRu_2Ge_2$ **EPL Vol. 33 Num. 8 pp 37002**

[48] Fernandes RM et al. (2010) Effects of Nematic Fluctuations on the Elastic Properties of Iron Arsenide Superconductors **Phys. Rev. Lett. 105, 157003**

[49] Gallais Y et al. (2013) Observation of Incipient Charge Nematicity in $Ba(Fe_{1-x}Co_x)_2As_2$ **Phys. Rev. Lett. 111, 267001**

[50] Yang YX et al. (2013) Raman scattering as a probe of charge nematic fluctuations in iron based superconductors **JPS Conf. Proc. 3, 015001**

[51] Thorsmolle VK et al. (2016) Critical quadrupole fluctuations and collective modes in iron pnictide superconductors **Phys. Rev. B 93, 054515**

[52] Wu SF et al. (2017) Superconductivity and electronic fluctuations in $Ba_{1-x}K_xFe_2As_2$ studied by Raman scattering **Phys. Rev. B 95, 085125**

[53] Kissikov T et al. (2016) NMR study of nematic spin fluctuations in a detwinned single crystal of underdoped $Ba(Fe_{1-x}Co_x)_2As_2$ **Phys. Rev. B 94, 165123**

[54] Kissikov T et al. (2017) Local nematic susceptibility in stressed BaFe2As2 from NMR electric field gradient measurements **Phys. Rev. B 96, 241108**

[55] Blomberg EC et al. (2012) Effect of tensile stress on the in-plane resistivity anisotropy in $BaFe_2As_2$ **Phys. Rev. B 85, 144509**

[56] Rosenberg E, Chu JH, Ruff J, Fisher IR (2018) Supplemental Material

[57] JG Analytis, HH Kuo, RD McDonald, M Wartenbe, NE Hussey, IR Fisher Transport near a quantum critical point in $BaFe_2(As_{1-x}P_x)_2$ **Nature Physics 10 (3), 194-197**

[58] Ikeda M et al. Elastocaloric Effect in $Ba(Fe_{1-x}Co_x)_2As_2$ Unpublished

[59] Malinowski P, Jiang Q, Sanchez J.J. et al. Suppression of superconductivity by anisotropic strain near a nematic quantum critical point. **Nat. Phys. (2020). https://doi-org.stanford.idm.oclc.org/10.1038/s41567-020-0983-9**

[60] Michael E. Fisher and J. S. Langer. Resistive Anomalies at Magnetic Critical Points **Phys. Rev. Lett. 20, 665 (25 March 1968)**

[61] H. Pfau, E. W. Rosenberg, P. Massat, B. Moritz, M. Hashimoto, D. Lu, I. R. Fisher, and Z.-X. Shen Electronic structure of the quadrupolar ordered heavy-fermion compound $YbRu_2Ge_2$ measured by angle-resolved photoemission **Phys. Rev. B 99, 075159 (2019)**